



5-2016

# Symbiotic plasmonic nanomaterials: Synthesis and properties

Abhinav Malasi

*University of Tennessee - Knoxville*, [amalasi@vols.utk.edu](mailto:amalasi@vols.utk.edu)

---

## Recommended Citation

Malasi, Abhinav, "Symbiotic plasmonic nanomaterials: Synthesis and properties." PhD diss., University of Tennessee, 2016.  
[https://trace.tennessee.edu/utk\\_graddiss/3722](https://trace.tennessee.edu/utk_graddiss/3722)

This Dissertation is brought to you for free and open access by the Graduate School at Trace: Tennessee Research and Creative Exchange. It has been accepted for inclusion in Doctoral Dissertations by an authorized administrator of Trace: Tennessee Research and Creative Exchange. For more information, please contact [trace@utk.edu](mailto:trace@utk.edu).

To the Graduate Council:

I am submitting herewith a dissertation written by Abhinav Malasi entitled "Symbiotic plasmonic nanomaterials: Synthesis and properties." I have examined the final electronic copy of this dissertation for form and content and recommend that it be accepted in partial fulfillment of the requirements for the degree of Doctor of Philosophy, with a major in Chemical Engineering.

Ramki Kalyanaraman, Major Professor

We have read this dissertation and recommend its acceptance:

Gerd Duscher, Dibyendu Mukherjee, Michael Hu, Alexander B. Papandrew, Siris O. Laursen

Accepted for the Council:

Dixie L. Thompson

Vice Provost and Dean of the Graduate School

(Original signatures are on file with official student records.)

---

# Symbiotic plasmonic nanomaterials: Synthesis and properties

A Dissertation Presented for the

Doctor of Philosophy

Degree

The University of Tennessee, Knoxville

Abhinav Malasi

May 2016

*Dedicated to my lovely parents, Shashi Malasi and N M Malasi and my life, Anshul.*

# Acknowledgments

I want to offer my sincere gratitude to the lovely people who supported me throughout my life and encouraged me to follow my dreams.

A special thanks goes to my advisors Dr. Ramki Kalyanaraman and Dr. Gerd Duscher for their support and guidance without which this thesis would have not been completed. I am very thankful to Ramki for giving me the opportunity to work under his guidance. Ramki has been an excellent mentor and for the last five and a half years working with him were filled with fun and challenges. I greatly appreciate his dedication to the group and admire the freedom he gives for conducting research. I am also thankful to him for the lengthy, timely and insightful discussions which helped in improving the understanding of my research work.

I would like to thank my committee members Dr. Michael Hu, Dr. Alexander Papandrew, Dr. Siris Laursen and Dr. Dibyendu Mukherjee for their valuable suggestions. I would like to thank my collaborator Dr. Hernando Garcia who has been a good mentor and I am really very thankful for his valuable inputs and discussions related to my work on plasmonics.

I would like to thank Dr. Veena Gopal Krishnan for teaching the chemical bath deposition technique. I am thankful to all the faculty who taught me courses.

I would also like acknowledge the valuable and insightful discussions with Dr. Alexander Papandrew, Dr. Maulik Patel and Dr. Rupam Mukherjee. I would also like to thank Dr. Michael Hu and his group in ORNL for teaching me the synthesis of CdSe quantum dots. Dale Hensley from CNMS, ORNL for helping out with SEM training. I would also like to thank John Dunlap and Greg Jones for helping out with the sample preparation and characterization of nanomaterials.

I appreciate the help and support received and the patience shown by Rita Gray and Jennifer Wolfenbarger from the CBE administrative office, Stephen Steiner from technical services and Doug Fielden from the mechanical systems group. Special thanks to Doug for fixing the e-beam, without his expertise my PhD would not have been completed. I would also like to thank Frank Holiway and Randy Stooksbury from the facilities.

I am thankful to my past and present labmates with whom I had the pleasure of working alongside. I am glad to have spend the time of my PhD with some of the interesting people whom I can never forget. I am thankful to Dr. Ritesh Sachan, Dr. Nozomi Shirato, Dr. Sagar Yadavalli, Vanessa Ramos, Emily Symonds, Humaira Taz, Jingxuan Ge, Annette Farah, Venkatanarayana Sandireddy, Mikayla Ehram, Connor Carr, Michelle Lames and Robert Sellmer for the wonderful time spent together in the confinements of DO 317 and SERF 403. Ritesh and Nozomi were my roommates and I cannot forget the memorable moments I had

with you guys.

Special thanks to Ritesh for being a supportive friend in my troubled times and a good critic. Ritesh was a good mentor and taught me most of the things of the lab. I am also glad to have learned driving from Ritesh which proved to be beneficial for my trips to Kent.

I would love to thank my friends Reza, Misagh, Michelle, Moughe, Amir, Fatimeh, Hadi, Hiraku, Sheng, Hanieh, Shuchita, Priyanki, Prashasti, Graham, Nima, Guru, Jordan, Shaofang, Yueying, Carlos, Mengkun, Ondrej and Sameer, whom I met in Knoxville and they will forever be in my heart.

I cherished the moments enjoyed with two amazing people Dr. Nick Diorio and Dr. Jakub Kolacz whom I met in Kent during my visits there.

I would love to thank my undergraduate wing mates with whom I have a special bond for life. Their constant humorous messages kept my spirits up and running.

Very special thanks to my elder brother Abhishek Malasi, who has always been my inspiration and role model and to whom I have always looked up to for each and everything. Love, support and belief in me of my parents, Mrs Shashi Malasi and Mr. N. M. Malasi, without which I would not be here. I am grateful to my family members, Yash, Siri, Srishti, Kshitiz and Hien, here in states who made my time here interesting and meaningful. I am also thankful to the love and affection bestowed upon me by my mother-in-law Veena Sharma, father-in-law R. R. Sharma, Momisha Khanduri, Parul Sharma, Diksha Sharma and Rithik Sharma. I am grateful for the love and support of the family members from my paternal and maternal sides.

Last but not the least, I am thankful to my loving wife Anshul Sharma for being the sunshine of my life. She always stood by me during my good and bad times. Always supported me and showed confidence in all my decisions. For me she is truly an amazing person, a good and loving wife and a better friend.

# Abstract

Metal particles of the dimensions of the order of 1 to 100's of nanometers show unique properties that are not clearly evident in their bulk state. These nanoparticles are highly reactive and sensitive to the changes in the vicinity of the particle surface and hence find applications in the field of sensing of chemical and biological agents, catalysis, energy harvesting, data storage and many more. By synthesizing bimetallic nanoparticles, a single nanoparticle can show multifunctional characteristics. The focus of this thesis is to detail the synthesis and understand the properties of bimetallic nanomaterial systems that show interesting optical, chemical, and magnetic behaviors, some of which fall into the category of a symbiotic behavior. Symbiosis is the mutual sharing of resources between two individual organisms. The potential design considerations in the synthesis of such symbiotic nanomaterials include their position in the electrochemical series, thermodynamic immiscibility, and vastly contrasting properties, such as plasmonic (Ag) and ferromagnetic (Co). In addition to these aspects, nanostructure size, shape, and composition can also play an important role in the ensuing optical, magnetic and chemical behaviors. For this work, two different synthesis routes were utilized to make nanostructures of various shapes, size, composition and spacing. The second part of the thesis focused on to understand the relationship between the role of intrinsic and extrinsic factors on the optical and chemical properties of these bimetallic nanostructures. From measurements of the plasmonic resonance energy and bandwidth, we developed a quantitative picture of the dependence of oxidation stability, plasmon quality factor and the radiative quantum efficiency on size and energy. These results showed that the bimetal nanoparticles could have comparable or better quality factor and quantum efficiency than pure Ag.

We also discovered a new class of thin film amorphous transparent semiconducting material. The semiconductor was made from a ternary oxide comprising of the metals Fe, Tb, and Dy. The combination of high visible light transparency, high conductivity and extraordinarily high mobility makes this material a potential candidate for use in thin film transistor and transparent conductor applications, and is a possible replacement for In-based materials.

# Table of Contents

<b>1</b>	<b>Introduction</b>	<b>1</b>
1.1	Introduction . . . . .	1
1.1.1	Bimetallic nanoparticles . . . . .	1
1.1.2	Symbiosis in bimetals . . . . .	3
1.2	Current knowledge and challenges . . . . .	5
1.2.1	Synthesis of better new plasmonic nanomaterials . . . . .	6
1.2.2	Metal oxidation investigation by LSPR characterization . . . . .	8
1.2.3	Far field quality factor and quantum efficiency of plasmonic nanoparticles . . . . .	9
1.2.4	Improved effective medium model incorporating multipolar contributions . . . . .	15
1.2.5	Discovery of iron-based amorphous material with high transparency and Hall mobility	16
1.3	Outline of thesis . . . . .	17
<b>2</b>	<b>Methods and techniques</b>	<b>18</b>
2.1	Experimental techniques involved in synthesis and characterization . . . . .	18
2.1.1	Selection of materials . . . . .	18
2.1.2	Synthesis techniques . . . . .	18
2.1.2.1	<i>Substrate preparation</i> . . . . .	18
2.1.2.2	<i>NSL mask formation</i> . . . . .	19
2.1.2.3	<i>Thin film deposition</i> . . . . .	19
2.1.2.4	<i>Laser irradiation for dewetting</i> . . . . .	20
2.1.3	Characterization techniques . . . . .	22
2.1.3.1	<i>Surface/morphology characterization</i> . . . . .	22
2.1.3.2	<i>Elemental identification</i> . . . . .	23
2.1.3.3	<i>Physical properties</i> . . . . .	23
2.2	Theory and modeling techniques . . . . .	27
2.2.1	<i>Oxide quantification:</i> . . . . .	27
2.2.2	<i>NSL simulation:</i> . . . . .	28
2.2.3	<i>Bridging Mie, Fresnel and Effective medium approximation theories:</i> . . . . .	28
2.3	Acknowledgment . . . . .	28



<b>3</b>	<b>Two-dimensionally ordered plasmonic and magnetic nanostructures on transferable electron transparent substrates</b>	<b>29</b>
3.1	Summary . . . . .	29
3.2	Method . . . . .	29
3.3	Characterization . . . . .	32
3.4	Results and discussion . . . . .	32
3.5	Acknowledgment . . . . .	38
<b>4</b>	<b>Localized surface plasmon sensing based investigation of nanoscale metal oxidation kinetics</b>	<b>39</b>
4.1	Summary . . . . .	39
4.2	Experimental details . . . . .	39
4.3	Results and discussion . . . . .	40
4.4	Acknowledgment . . . . .	45
<b>5</b>	<b>Plasmonic quality factor and quantum efficiency of hemispherical Ag and bimetal AgCo nanoparticles</b>	<b>47</b>
5.1	Summary . . . . .	47
5.2	Results . . . . .	47
5.2.1	Optical spectroscopy of Ag nanoparticles . . . . .	47
5.2.2	Pure Ag nanostructures in different environments . . . . .	48
5.2.3	Bimetallic Ag nanostructures . . . . .	51
5.3	Discussion . . . . .	53
5.3.1	Quality factor of hemispherical nanoparticles . . . . .	53
5.3.2	Model for plasmon bandwidth . . . . .	54
5.3.3	Calculation of the non-radiative and radiative dephasing rates . . . . .	57
5.3.4	Ag vs AgCo: Radiative and non-radiative contributions . . . . .	60
5.3.5	Quantum efficiency of plasmonic scattering from Ag and AgCo . . . . .	62
5.4	Conclusion . . . . .	63
5.5	Acknowledgment . . . . .	63
<b>6</b>	<b>From Mie to Fresnel through effective medium approximation with multipole contributions</b>	<b>65</b>
6.1	Summary . . . . .	65
6.2	Theory . . . . .	65
6.3	Results . . . . .	71
6.4	Limitations of the Model . . . . .	73
6.5	Acknowledgement . . . . .	75
<b>7</b>	<b>Novel Iron-based ternary amorphous oxide semiconductor with very high transparency, electronic conductivity, and mobility</b>	<b>76</b>
7.1	Summary . . . . .	76
7.2	Results . . . . .	76

7.3	Discussion and conclusion . . . . .	83
7.4	Methods and Techniques . . . . .	84
7.4.1	Material synthesis and processing . . . . .	84
7.4.2	Surface characterization . . . . .	84
7.4.3	Material characterization . . . . .	85
7.4.4	Optical properties . . . . .	85
7.4.5	Magnetic properties . . . . .	86
7.4.6	Electrical properties . . . . .	86
7.5	Acknowledgments . . . . .	87
7.6	Author Contributions Statement . . . . .	87
7.7	Supplemental Information . . . . .	88
7.7.1	Film roughness . . . . .	88
7.7.2	GIXRD measurements of films . . . . .	88
7.7.3	Tauc plot measurement . . . . .	88
7.7.4	Magnetic measurements by SMOKE . . . . .	88
7.7.5	Hall Effect Measurement . . . . .	89
7.7.6	XPS Measurements . . . . .	90
7.7.7	SEM Measurement . . . . .	90
7.7.8	TEM and EELS measurements . . . . .	90
<b>8</b>	<b>Conclusion and Future work</b>	<b>92</b>
8.1	Conclusion . . . . .	92
8.2	Future work . . . . .	94
8.2.1	Bimetal related work . . . . .	94
8.2.2	Terfenol-D related work . . . . .	97
	<b>Bibliography</b>	<b>99</b>
	<b>Vita</b>	<b>116</b>

# List of Tables

2.1	<i>Details of material and morphology studied in the thesis.</i>	22
4.1	<i>Comparison for 50% bandwidth decay for different Co-Ag samples.</i>	43

# List of Figures

1.1	<i>(a) The absorption spectra of Au nanoparticles in core-shell structures as a function of increasing Ag shell thickness. (b) The dependence of Faraday rotation and electric field enhancement on the Co content in Co-Ag core-shell NPs. . . . .</i>	2
1.2	<i>(a) Transmission electron microscopy image of Pt nanorods with Au NPs on its tip. (b) Comparison of H<sub>2</sub> gas generation as a function of time for three different types of Pt-Au nanostructures. . . . .</i>	3
1.3	<i>Evidence for symbiotic behavior in bimetal nanoparticles (a) The optical plasmonic bandwidth decay of Ag occurs much faster than for Ag-Co (top panel). This was attributed to decreased oxidation of Ag surface due to galvanic coupling with Co (bottom panel). (b) Transmission electron microscopy high angle annular dark field (HAADF) image of Ag-Co NP (top panel). Bottom panel shows plasmon mapping using low loss electron energy loss spectroscopy (EELS) of the region inside the white dashed rectangle (marked on top panel). The plasmon map indicated the presence of localized surface plasmons, i.e. ferroplasmons, on the Co side and the generation of a hot spot at the Ag-Co-vacuum interface. . . . .</i>	4
1.4	<i>Schematic showing the pairs of symbiotic properties studied using plasmonics. . . . .</i>	5
1.5	<i>AFM micrograph showing the nanoparticle generated from NSL. The location marked as 1 and 2 point to some common defects in the NSL pattern. . . . .</i>	7
1.6	<i>The plasmon decay of metal nanoparticle can be interpreted by a two-level excitation model. . . . .</i>	9
1.7	<i>Plasmon quality factor of the elements in the periodic table. . . . .</i>	11
1.8	<i>Different loss mechanisms responsible for the broadening of the plasmon bandwidth. . . . .</i>	12
1.9	<i>The real (lines with symbols) and imaginary (dashed curves) components of the energy-dependent dielectric functions for Ag and Co. . . . .</i>	13
1.10	<i>(a) Comparison of the bandwidth and the dephasing time of Au nanospheres with nanorods as a function of plasmon resonance energy. (b) Comparison of the quality factor of Au nanospheres with nanorods as a function of plasmon resonance energy. . . . .</i>	14
1.11	<i>Schematic summarizing the theme of bridging Mie with Fresnel theories using EMA. . . . .</i>	16
2.1	<i>The equilibrium phase diagrams for (a) Ag-Co and (b) Ag-Fe systems. . . . .</i>	19
2.2	<i>(a) NSL setup built to make PS monolayer templates at the air-water interface. (b) Large monolayer coverage area of PS mask formed at the air-water interface. . . . .</i>	20
2.3	<i>SEM image for the (a) hemispherically shaped Ag NPs and (b) bimetallic Co-Ag NP. . . . .</i>	21

2.4	<i>Shows the parameter space for the Ag-Co bimetal system.</i>	21
2.5	<i>SEM image of the nanotriangles fabricated using NSL technique. (a) Shows the image of as-synthesized Ag nanotriangles. (b) Shows the image of laser treated Ag nanotriangles. An individual triangle break into 3-6 semispherical NPs.</i>	22
2.6	<i>Deuterium light source spectra.</i>	24
2.7	<i>(a) The raw transmission data. (b) Absorption spectra converted from raw transmission data using Eq. 2.1. (c) Normalized absorption spectra fitted with two Lorentzian peaks.</i>	24
2.8	<i>Tauc plot to find the optical band gap of semiconductor materials.</i>	25
2.9	<i>SMOKE setup for measurements to be done in longitudinal orientation.</i>	26
3.1	<i>The schematic shows the three major steps for the TEM sample preparation. (a) Step 1 of the synthesis, which is focused on NSL template formation. It shows the formation of NSL template on plasma treated carbon film on mica substrates. (b) Step 2 is fabrication of nanostructures, which is achieved by depositing metal films and then etching out the template. Further heat treatment, such as with laser pulses, can be done to the metal nanostructures to change their shape. (c) Step 3 is the float off of the carbon substrate with NSL structures on the water surface which is then captured on the TEM grid by draining the water.</i>	30
3.2	<i>(a) SEM images of Ag nanotriangles formed by NSL on quartz substrate. Inset shows the FFT of the contrast in (a) providing clear evidence for the hexagonal symmetry. (b) Magnified image of the repeating Ag nanotriangle hexagonal pattern. (c) SEM image of Ag nanoparticles formed by irradiation of Ag nanotriangles on quartz using pulsed laser heating. (d) Magnified image of the irradiated Ag nanotriangles. (e) TEM HAADF image of the Ag nanotriangles formed by NSL + FO. The underlying lacey carbon film of the TEM substrate is also evident. Inset shows the FFT (taken from the the red square) showing evidence for the hexagonal symmetry of the spatial arrangement. (f) Magnified TEM image of the Ag nanotriangle repeating unit. (g) TEM HAADF image of the Ag nanoparticles transformed from nanotriangles following irradiation by laser pulses formed by NSL + FO. Inset FFT shows the hexagonal symmetry. (h) The magnified image of the irradiated Ag nanotriangle patterns. The scale bar on the individual hexagonal ring images is 500 nm.</i>	33
3.3	<i>Low loss EELS mapping of a Ag nanotriangle on C substrate. (a) HAADF image of Ag nanotriangle. (b-d) Map of different plasmon modes excited by the e-beam. (b) corresponds to an energy of 1.35 eV, (c) is for 2.5 eV and (d) is 3.2 eV.</i>	34

3.4	(a) Far-field optical absorption spectrum of Ag nanotriangles for various thickness of the triangular nanostructures. Also shown is the absorption spectrum for the Ag nanoparticles formed by pulsed laser heating (dashed blue line). (b) SEM morphology of Co nanotriangles from NSL on quartz, with inset showing the FFT hexagonal pattern. (c) Comprison of the far field optical absorption spectrum from Co, Ag and Co-Ag nanotriangles deposited at $10^\circ$ , respectively. (d) Magnetic hysteresis measured by SMOKE technique in longitudinal geometry comparing a Co film (solid black line), NSL Co nanotriangles (dotted red line) and NSL Co-Ag triangles (dashed green line).The Co triangles were deposited at $10^\circ$ and Co-Ag was deposited at $10^\circ$ and $-10^\circ$ , respectively. . . . .	35
3.5	(a) The co-ordinate system for the modeling of ARNSL. $x$ - $y$ is the plane of the substrate with $z$ -axis acting as the normal to the plane. $\vec{p}$ is the vector denoting the direction of the metal flux and makes an angle $\theta$ with the $z$ -axis. $\phi$ is the orientation of the HCP with respect to the co-ordinate system. Some of the simulated patterns are shown in: (b) Simulated pattern for a single metal deposition with $\theta = 0^\circ$ and $\phi = 0^\circ$ . (c) Simulated pattern of bi-metals deposited at $\theta = \pm 10^\circ$ , $\phi = 0^\circ$ . (d) Simulated pattern for $\theta = \pm 10^\circ$ , $\phi = 90^\circ$ . (e) Experimental SEM image of Ag (bright triangles) and Co (dark triangles) deposited for the conditions in (c). (f) SEM image of repeating hexagonal pattern shown in (e). (g) Experimental SEM image of Ag (bright triangles) and Co (dark triangles) deposited for the conditions in (d). (h) SEM image of the repeating unit shown in (g). A hexagon is marked in the SEM images for reference and to show the repeating units of NSL. The length of the scale bars in (f) and (h) are of 500 nm each. . . . .	37
3.6	(a) The HAADF image of Co-Ag nanotriangles formed by deposition at $10^\circ$ and $-10^\circ$ , respectively. (b) A magnified HAADF image of one pair of Co-Ag nanotriangles, encircled in (a). (c) Core loss EELS map yielding the thickness of Ag in the structure shown in (b). Core loss EELS map yielding the thickness of Co for the structure shown in (b). . . . .	38
3.7	Elemental mapping of Ag and Co using EDS in the TEM. (a) HAADF image of Co (dark) and Ag (bright) triangles. (b) EDS map of Co across the HAADF image shown in (a). (c) EDS map of Ag across the HAADF image shown in (a). The scale bar is of 500 nm length. . . . .	38
4.1	SEM images of Co-Ag NP arrays with the particle size distribution shown in the inset. (a) NP made from the Ag(5 nm)/Co(1 nm) case yielding particles of 16.7% Co with an average particle diameter of 91 nm and (b) NP made from the Co(2 nm)/Ag(5 nm) case yielding particles of 28.5% Co with an average particle diameter of 100 nm. . . . .	40
4.2	Broadband optical absorption spectra recorded as a function of aging time for the two Co-Ag arrays. (a) Measured spectra for the 16.7% Co array and (b) spectra for the 28.5% case. The strong peak (such as the one at 520 nm for the 0 day 16.7% sample) is the LSPR peak. This peak decays with increasing aging time for both samples. (c) Comparison of the normalized optical absorption spectrums of freshly prepared Ag with 16.7 and 28.5% Co samples. . . . .	41

4.3	(a) The change in the normalized BW of the LSPR peak of the bimetal nanoparticles is plotted. The solid triangles corresponds to the experimental values for the 16.7% Co while the open squares correspond to the 28.5% case. An initial slow decrease is followed by a rapid decrease at a later time for both Co cases. The dashed lines correspond to fits based on the known oxidation behaviors of Co and Ag metals. The inset shows the slow decay portion of the Co-Ag particles for the 16.7% case (solid triangles) and the 28.5% case (open squares). The dashed line is an inverse-log curve as a guide to the eye. (b) The LSPR bandwidth decay of pure Ag nanoparticles (solid circle) overlaid with the rapid decay portions of the Co-Ag nanoparticles from (a). The dashed exponential decay line serves as a guide to the eye. . . . .	42
4.4	(a) The experimental transmission spectrum (solid line) shown is for the 16.7% Co sample taken after day 12. This experimental spectrum was fitted using the MFA by varying the CoO fraction to get the best fit shown by the dashed line. (b) The theoretically calculated 1-dimensional oxide thickness (of CoO) plotted as function of days. An initial period of rapid growth is followed by a slower linear trend. The life time of the Co part of Co-Ag was estimated from the linear regime of oxide growth. The inset shows the CoO volume fraction growth over prolonged time extracted by fitting the experimental transmission spectrums using MFA. The dashed and dotted lines in the inset are guide for the eyes. (c) The plot for theoretically calculated Co lifetime using MFA (solid circles line) and experimental values from Fig. 4.3(a) (symbols). The dashed line is a linear fit to the data. . . . .	44
5.1	(a) SEM image of pure Ag NP array of size $36 \pm 11$ nm with the particle size distribution histogram is in the inset. (b) The normalized absorption spectrum of different sized hemispherical NPs plotted as a function of energy. (c) The plasmon resonance energy and the bandwidth are plotted as a function of Ag NP size. The black hollow circles and the solid red squares denotes plasmon resonance energy and the bandwidth, respectively. The black dotted and the dashed red lines are the best fits for the experimental data. . . . .	49
5.2	Compares the Lorentz, Gaussian and Voigt fits to the experimental optical spectrum. . . . .	49
5.3	(a) Compares the absorption spectrum of Ag NPs in air with that of the Ag NPs dipped in toluene and machine oil. (b) Compares the resonance energy of Ag NPs measured in air and different dielectrics as a function of Ag NP size. (c) Compares the bandwidth of Ag NPs measured in air and different dielectrics as a function of Ag NP size. . . . .	50
5.4	(a) Compares the absorption spectrum of Ag NPs embedded in Fe-Tb-Dy amorphous semiconductor oxide. (b) Compares the BW of Ag NPs embedded in Fe-Tb-Dy amorphous semiconductor oxide and CdS film as a function of resonance energy. . . . .	50
5.5	Shows the normalized absorption spectrums of Ag NPs embedded in (a) Co film and (b) Fe film. As the thickness of the metal film is increased, the plasmon energy decreases. (c) Compares the BW of Ag NPs embedded in Co and Fe metal film as a function of resonance energy. . . . .	51

5.6	<i>(a) Representative SEM image of Co-Ag NP system. The SEM corresponds to Ag (5 nm)/Co (2 nm) with the average NP size of <math>113 \pm 30</math> nm. The inset shows the size distribution histogram. (b,c) Corresponds to the normalized absorption spectrums of Co-Ag bimetallic system. The Ag film thickness is fixed at 5 nm and the Co thickness is varied from 1-5 nm. The absorption spectrums in (b) are for Co/Ag and in (c) for Ag/Co configuration. (d) Plots the plasmon energy as a function of NP size for the two Co-Ag systems. (e) Plots the plasmon energy as the function of the Co percentage in the NP system. . . . .</i>	52
5.7	<i>BW dependence of CoAg bimetal on (a) resonance energy, (b) volume of the bimetal nanoparticle and (c) Co amount (volume %). . . . .</i>	52
5.8	<i>Quality factor for Ag in various environments. (a) Dependence of <math>Q</math> on particle volume. (c) dependence of <math>Q</math> on resonance (LSPR) energy. . . . .</i>	53
5.9	<i>Quality factor for Ag versus AgCo in air. (a) Dependence of <math>Q</math> on the effective volume of Ag within the nanoparticle. (b) Dependence of <math>Q</math> on the total volume of nanoparticle. (c) dependence of <math>Q</math> on resonance (LSPR) energy. . . . .</i>	54
5.10	<i>(a) Imaginary component of the dielectric function <math>\epsilon''</math> of Ag (solid line) and Co (dashed line) as a function of energy. (b) The quality factor for AgCo bimetal spheres calculated using Mie theory with an effective medium approach to calculate the dielectric function. . . . .</i>	57
5.11	<i>(a) SEM image of the Ag nanotriangle array synthesized by NSL using a template of 200 nm PS beads with the height of the triangles equal to 25 nm. (b) Normalized absorption spectrums of Ag nanotriangles of height 25 nm formed by PS bead templates of 100, 200 and 500 nm. As the size of the PS bead is increased, the Ag plasmon shifts toward lower energy (red shifts). (c) Plots the plasmon resonance energy and (d) BW as a function of volume of the nanotriangles formed by different PS bead templates. . . . .</i>	58
5.12	<i>(a) Compares the BW of hemispherical Ag NPs with Ag nanotriangles plotted against the plasmon energy. As the plasmon resonance energy increases, the BW of nanotriangles increased while that of hemisphere decreased. (b) Plots the <math>K</math> values calculated at the different plasmon resonance energies. The dashed line represents the average <math>K</math> value for the data set plotted. . . . .</i>	59
5.13	<i>Radiative and non-radiative contributions to the total bandwidth of Ag NPs. (a) Energy dependence of the bandwidth contributions. (b) Volume dependence of the bandwidth contributions (note log scale on x-axis). . . . .</i>	59
5.14	<i>Radiative and non-radiative contributions to the total bandwidth of bimetallic NPs. (a) Energy dependence of bandwidth contributions for AgCo. (b) Volume dependence of the bandwidth contributions for AgCo (note log scale on x-axis). (c) Energy dependence of bandwidth contributions for CoAg. (d) Volume dependence of the bandwidth contributions for CoAg (note log scale on x-axis). . . . .</i>	61
5.15	<i>(a) Quantum Efficiency of Ag in different dielectric and lossy mediums. Quantum Efficiency of Ag and bimetal AgCo. (b) Energy dependence of <math>\eta</math>. (c) Variation of <math>\eta</math> with effective volume of Ag in the nanoparticle. (d) Variation of <math>\eta</math> with total volume of nanoparticle. . . .</i>	62



5.16	<i>Q and <math>\eta</math> versus resonance energy for (a) pure Ag nanoparticles and (b) CoAg nanoparticles. (c) Comparison of the ratio <math>Q/\eta</math> versus resonance energy for the various pure Ag and bimetallic AgCo nanoparticles.</i>	63
6.1	<i>Real part of the effective dielectric function for two different particle sizes, as predicted by K-K relation and by our theory result, Eq. 6.21.</i>	70
6.2	<i>OD for a) 10 nm and b) 100 nm radius Ag nanoparticles embedded in glass matrix. The plots were calculated using the Maxwell-Garnett (MG), Gans-Happel (GH), and approximate Mie theories, as well as by our new theory, Eq. 6.21.</i>	71
6.3	<i>Comparison of our theoretical prediction based on Eq. 6.21 (solid red curve) to the experimental measurement (dashed black curve) of OD of nanoparticles of Ag with average size of 40 nm embedded in a glass matrix. Results of the MG theory (green dashed curve, scaled by a factor of 0.5), GH (dark blue dashed curve), and Mie (light blue dashed curve) theories are also shown. Our new EMA theory result of Eq. 6.21 overlays the Mie theory result very well, while predicting both the dipole and quadrupole peaks.</i>	72
6.4	<i>a) The resonance wavelength of the dipole (open circles) and quadrupole (open squares) excitation of Ag nanoparticles embedded in glass as a function of the particle radius calculated using Eq. 6.21. b) Plot of the absorption curves generated for Ag nanoparticles of different radius embedded in glass matrix.</i>	73
7.1	<i>(a) Optical photograph of lettered blocks showing the large transparency of 25 nm thick films in as-prepared state (marked as AP), and following annealing in nitrogen (marked as N2) and oxygen (marked as O2) at 500°C for 2 hrs. (b) Optical energy (and wavelength) dependent transmission of as-prepared films with thickness between 9 to 37 nm (dashed curves) and following annealing of the 25 nm film solid curves). (c-d) SEM (c) and AFM (d) information from a 25 nm as-prepared film respectively. (d) Tauc plot comparing the direct optical absorption in 25 nm films (as prepared is dashed line while annealed are solid lines). The extrapolations from the strongly absorbing linear regimes are shown and were used to estimate the band gap. Inset shows the Tauc direct band gap values as a function of thickness of the as-prepared films and following annealing of the 25 nm film. A line corresponding to the average band gap value from measurements of various as-prepared films is also shown in the inset.</i>	78

7.2	<i>(a) Amorphous microstructure of the as-prepared films was evidenced by TEM imaging and selected area diffraction (inset). (b-c) EELS analysis of the as-prepared and O<sub>2</sub>annealed films only detected Fe, and O (Fig. c) and Tb and Dy (Fig. d). In Fig. (b) the EELS spectrum from a PLD nanoparticle is also shown by dotted curve. (d-g) XPS measurements showing the various detected components in the as-prepared vs O<sub>2</sub> annealed films. (d) Fe 2p signal (e) O 1s signal. (f) Tb 3d 5/2 signal, (g) Dy 3d 5/2 signal. In figures b-g, the as-prepared (AP) films are shown by dashed curves while the O<sub>2</sub> (O<sub>2</sub>) annealed films are shown by solid curves. The vertical dotted lines mark the position of the various absorption edges (EELS) and peaks (XPS) as indicated. The additional vertical lines in Fig. (d) correspond to the additional Fe<sub>3d</sub> absorption peaks found in the hematite and magnetite form or iron oxides.</i>	81
7.3	<i>Transport properties of the as-prepared (a-c) and annealed films (d-f). (a) Dependence of conductivity on thickness of as-prepared films. Inset shows that the conductivity <math>\sigma</math> increased exponentially with temperature for a 25 nm as-prepared film. (b) The mobility of the as-prepared films showed n-type conductivity and its magnitude was relatively unchanged with thickness yielding an average value of <math>32 \pm 4 \text{ cm}^2/\text{V}\cdot\text{s}</math>. (c) The electron carrier concentration in the as-prepared films decreased exponentially with increasing film thickness. This correlated with an increased surface roughness of the films (inset). (d) Conductivity change for 25 nm films following annealing in nitrogen (N<sub>2</sub>) or oxygen (O<sub>2</sub>) at 500°C for 2 hrs. (e) Mobility change with annealing. (f) Carrier concentration remained relatively unchanged following annealing. In figures d-f, the as-prepared films are indicated as AP while the O<sub>2</sub> and N<sub>2</sub> annealed films are marked as O<sub>2</sub> and N<sub>2</sub> respectively. The dashed lines in (a-c) correspond to best fits to the experimental data. The dashed lines in (d-f) correspond to guides to the eye.</i>	82
7.4	<i>Surface roughness profile of as-deposited films measured using AFM.</i>	88
7.5	<i>(a) Shows the XRD of the Terfenol-D target. Indexing of the various peaks showed that the target was consistent with the original Terfenol-D composition. (b) Comparison of GIXRD scans of as-prepared, nitrogen annealed, and oxygen annealed films of 25 nm thickness as well as the underlying substrate which was SiO<sub>2</sub>(400 nm)/Si. The only features evident from the films were the underlying substrate features, as indicated on the figure. This confirmed that the films were amorphous.</i>	89
7.6	<i>(a) Tauc plot of as-deposited films. (b) Kerr rotation measurements of as-prepared and annealed films. (c) Plot of Hall voltage as a function of applied magnetic field for a 74 nm thick as-prepared film studied for two different voltage configurations for an applied current of 100 <math>\mu\text{A}</math>.</i>	89
7.7	<i>XPS survey scans to determine elements present in the as-prepared and annealed films.</i>	90
7.8	<i>(a) SEM micrograph of the surface of an O<sub>2</sub> annealed film shows a smooth morphology and a decrease in the nanoparticles from the PLD process in comparison to the as-prepared films (shown in manuscript Fig. 1(c)). (b) TEM micrograph of O<sub>2</sub> annealed film.</i>	91

8.1	<i>Schematic showing the various steps to form 2D periodic nanostructure arrays on electron transparent substrate. . . . .</i>	92
8.2	<i>Schematic showing by synthesizing bimetals of CoAg, the lifetime of Ag increases. . . . .</i>	93
8.3	<i>Possible different morphologies of NPs synthesized using NSL. . . . .</i>	94
8.4	<i>(a) Compares the absorption spectrum of Co-Ag, Fe-Ag and Ni-Ag NPs of almost equal thicknesses. (b) Compares the optical bandwidth degradation of the bimetals in (a). . . . .</i>	95
8.5	<i>(a) Compares the absorption spectrum of Co-Ag NPs arrays for different Co percentage. (b) Compares the Kerr hysteresis loops for different Co compositions for longitudinal. . . . .</i>	96
8.6	<i>(a) Representative SEM image for Fe-Ag nanotriangles synthesized using 500 nm PS bead template. The thicknesses of Fe and Ag are 12 and 15 nm, respectively. The length of the scale bar is 200 nm. (b) Absorption spectra for three different thicknesses of Ag for fixed Fe thickness in Fe-Ag nanotriangles. (c) Kerr rotation comparison for the three different thicknesses of Ag with fixed Fe amount. . . . .</i>	96
8.7	<i>(a) Plots the bandwidth of Ag, Co-Ag and Fe-Ag nanotriangles as a function of plasmon resonance energy. (b) Plots the quality factor of Ag, Co-Ag and Fe-Ag nanotriangles as a function of plasmon resonance energy. . . . .</i>	96
8.8	<i>(a) Photograph of synthesized CdSe quantum dots. (b) Shows the absorbance and the photoluminescence of CdSe quantum dots. . . . .</i>	97

# Chapter 1

## Introduction

### 1.1 Introduction

The overall goal of this thesis is to synthesize and investigate the far field plasmonic properties of bimetallic nanoparticles that can show new and/or improved behavior through symbiotic relationships. The primary motivators for this work, which are detailed below, are the recent evidences for symbiotic behaviors, especially improved chemical stability and appearance of ferroplasmonic character in noble metal - ferromagnetic metal systems.

#### 1.1.1 Bimetallic nanoparticles

One of the most interesting properties demonstrated by metal nanoparticles is their strong and resonant response to electromagnetic (EM) fields. In general, when an electromagnetic field (light) shines on a metal nanoparticle, whose size is comparable to or smaller than the wavelength of light, it can induce collective coherent oscillations of the free (conduction) electrons of the metal. For nanoparticles, these oscillations occur at specific frequency known as the plasmon frequency or the localized surface plasmon resonance (LSPR) frequency [3]. Various characteristics of this resonant plasmon interaction, such as the location of the plasmon frequency and the intensity of the resonance, such as determined by the plasmon bandwidth, depend on the metal-type, i.e. its dielectric function, as well as shape and size. In addition, the character of the surrounding medium also plays a very important role in the overall response. For instance, interaction between metal nanoparticles in proximity to other materials (metals, semiconductors or dielectrics) can give rise to new phenomenon such as Fano resonance, plasmon hybridization, enhanced magneto-optical activity, improved catalytic activity, enhanced solar cell efficiency, and better sensing of chemical or biological agents [4, 5, 6, 7, 1, 8]. The tuning of the plasmonic properties as well as the interactions is of great interest and has been explored by changing the shape, size and the ambient environment properties [3]. Another possible way to further tune the response of the metal nanoparticles is by synthesizing bimetallic or multi-metallic nanoparticles. It has been seen that on combining two different metals, new phenomenon and/or improved properties are observed in the nanoscale. For example, in core-shell nanoparticles of Au-Ag, the plasmon resonance energy of the Au core could be decreased from 500 to 400 nm by increasing the Ag shell

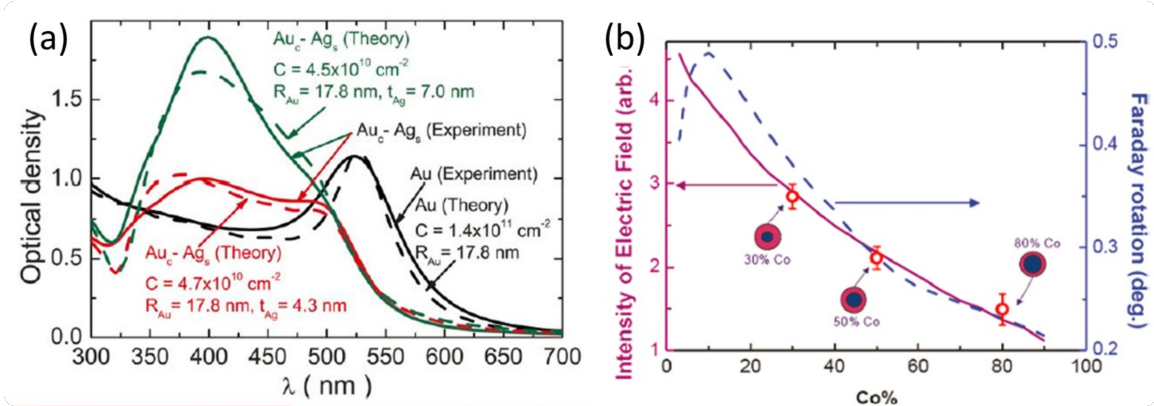


Figure 1.1: (a) The absorption spectra of Au nanoparticles in core-shell structures as a function of increasing Ag shell thickness. (b) The dependence of Faraday rotation and electric field enhancement on the Co content in Co-Ag core-shell NPs. (a) was taken from ref. [1] while (b) was taken from ref. [2].

thickness, as shown in Fig. 1.1(a) [1]. The other unique feature of the Au-Ag core-shell nanoparticle is that it supports Fano resonances below a certain Ag shell thickness. Fano resonance is a phenomenon seen at the nanoscale due to the interference of localized surface plasmon resonance (LSPR) and the continuum of interband transitions. In the nanoscale, other unique phenomenon such as hybridization or dipole-dipole coupling between homo dimers and hetero dimers can also be seen. By synthesizing bimetallic nanoparticles that combine metals with large intrinsic magneto-optical (MO) activity, such as ferromagnets, with metals with large intrinsic plasmonic resonances, such as the noble metals, the MO activity of the bimetallic nanoparticle can be significantly enhanced. For instance, core-shell nanoparticles of Co-Ag shows much higher Faraday rotation than pure Co, at the plasmon resonance frequency of the bimetallic nanoparticle. The Faraday effect is the change in polarization state of the transmitted light [9]. The enhanced Faraday rotation has been attributed to the local electric field enhancement due to the plasmonic resonance in the Co-Ag nanoparticle, as shown in Fig. 1.1(b) [2]. Plasmonic nanosandwiches consisting of Au/Co/Au system have also demonstrated enhanced MO activity at the LSPR of the nanosandwich [10]. The MO activity and the LSPR of the nanosandwich can be further tuned by controlling the thickness of the individual metal layers or the diameter of the nanosandwich [11, 10]. The demonstration of improved MO activity is amongst the first examples in which the material properties are significantly improved directly or indirectly due to plasmon excitations. Another class of materials where plasmonics benefit the properties is catalysis and, although the mechanism(s) is/are presently being debated, a growing number of examples show correlation between improved catalytic behavior and plasmonics. For instance, Pt nanorods with Au at the tips demonstrate much higher activities in visible and infrared light than shown by Pt nanorods covered with Au, as shown in Fig. 1.2(a) [12]. These Pt nanorods modified with Au at the tip were used for  $\text{H}_2$  generation and showed increased  $\text{H}_2$  production that was attributed to excited (hot) electrons transfer from plasmonic Au to the Pt [Fig. 1.2(b)] [12]. There are many other supporting evidences, such as Au-Cu nanoalloy particles on  $\text{TiO}_2$  surface demonstrating better photocatalytic activity for the reduction of carbon dioxide to methane by water [13].

These examples demonstrated that the bimetallic nanoparticles in which one of the components is a plasmonic metal, can enhance the overall properties of the other individual non-plasmonic metal constituent. In fact, for the

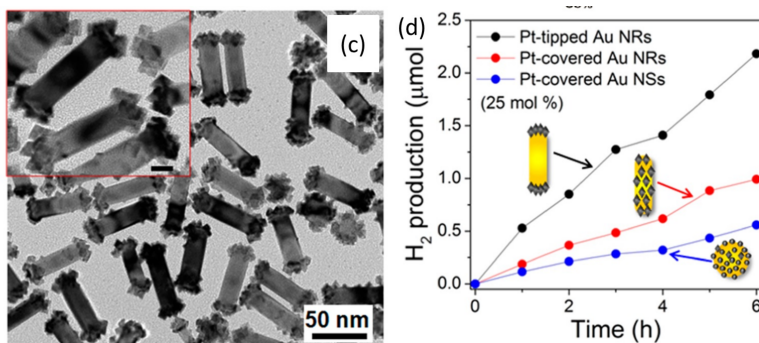


Figure 1.2: (a) Transmission electron microscopy image of Pt nanorods with Au NPs on its tip. (b) Comparison of H<sub>2</sub> gas generation as a function of time for three different types of Pt-Au nanostructures. Figures taken from ref. [12]

examples discussed above, the common factor for improvement in the properties can be stated to be the plasmonic character of one of the metal constituents.

### 1.1.2 Symbiosis in bimetals

While the last section provided examples of how the plasmonic materials can greatly improve the existing properties of other metals when in contact with them, another interesting question that arises is whether the properties of the plasmonic material itself can be enhanced or improved when in contact with other non-plasmonic materials. If so, then these types of bimetallic nanoparticles could be termed as **symbiotic plasmonic nanomaterials**.

It has been observed that the coexistence of plants with its natural environment leads to behaviors in which the ecosystem and its evolution cannot be separated [14]. That is, they have a symbiotic relation in which the evolution of plants gets affected by their ecosystem while, on the other hand, their evolution affects the ecosystem. This type of symbiotic relations can be seen in the animal kingdom also, where bees depend on flowers for nectar and in turn help in dispersing pollens. Learning from this type of behavior seen in nature, we hope to expand it to pairs of non-living systems. In this thesis, we will investigate pairs of plasmonic and magnetic materials which, when combined to form bimetallic nanostructures (NSs) show unique optical, magnetic and chemical properties that result from symbiosis. The idea of symbiotic metallic nanomaterials originated from recently published works on bimetallic Ag-Co nanoparticles. It was reported that bimetals of Ag-Co nanoparticles (NPs) showed better refractive index sensing and good environmental stability in comparison to the monometals [15, 16]. Others also found that Ag-Co bimetals can show better catalytic behavior [7]. Two different studies were done on the Ag-Co NP system. In one study, the Ag part of the Ag-Co nanoparticle showed resistance to oxidation in comparison to the Co part of the nanoparticle. The oxidation behavior was studied using UV-vis spectroscopy, in which the degradation of the bandwidth of the plasmon peak was studied over a certain period of time as shown in Fig. 1.3 (a), top panel. It was found that Co protected the Ag from oxidation because the Ag-Co NP was acting like a galvanic cell with Co behaving as a sacrificial anode [Fig. 1.3 (a), lower panel] [16]. In another study, low-loss electron energy loss spectroscopy (EELS) was done to map the plasmons on these Ag-Co NPs [Fig. 1.3 (b)]. It was seen

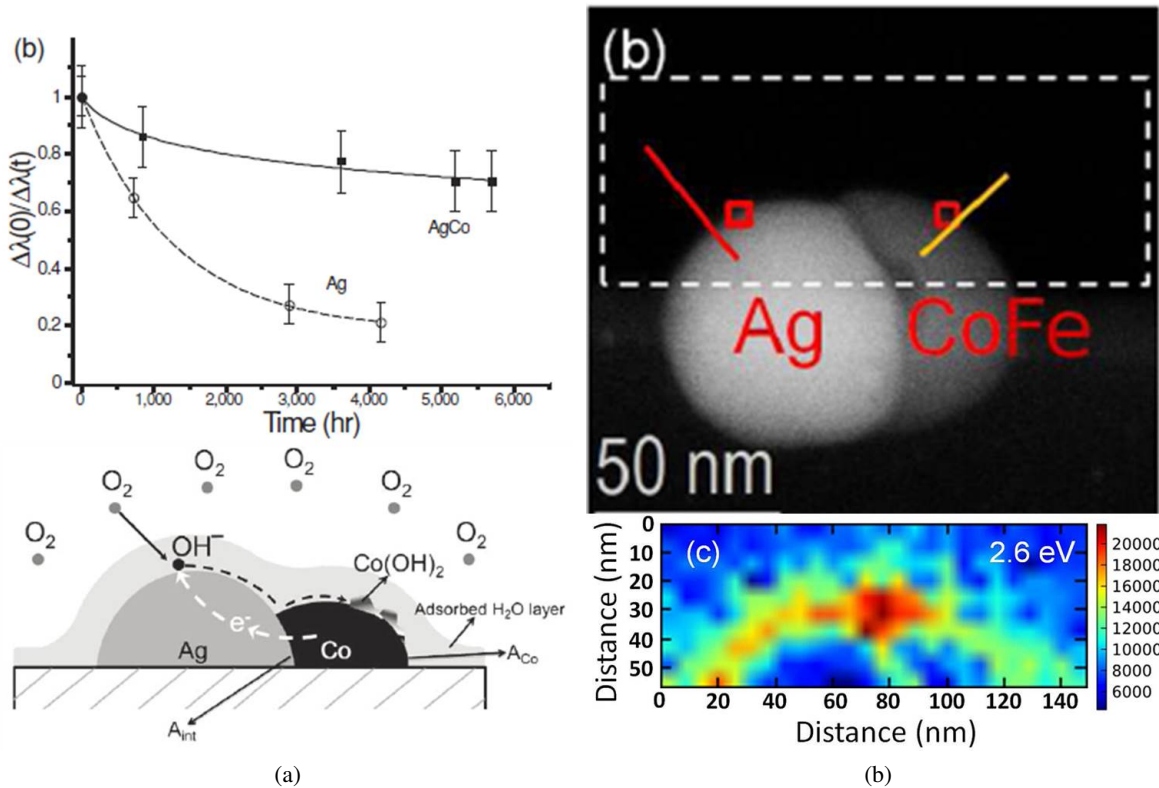


Figure 1.3: Evidence for symbiotic behavior in bimetal nanoparticles (a) The optical plasmonic bandwidth decay of Ag occurs much faster than for Ag-Co (top panel). This was attributed to decreased oxidation of Ag surface due to galvanic coupling with Co (bottom panel) [16]. (b) Transmission electron microscopy high angle annular dark field (HAADF) image of Ag-Co NP (top panel). Bottom panel shows plasmon mapping using low loss electron energy loss spectroscopy (EELS) of the region inside the white dashed rectangle (marked on top panel). The plasmon map indicated the presence of localized surface plasmons, i.e. ferroplasmons, on the Co side and the generation of a hot spot at the Ag-Co-vacuum interface [17]. Figures were taken from ref. [17].

that the pure Co NP did not show any plasmon peak in the visible spectrum but the Co part of the Ag-Co NP showed an intense localized surface plasmon on the Co side of the bimetal NP. This plasmon, which was comparable in intensity to the plasmon on the Ag side of the bimetal was termed as a Ferroplasmon [17]. Thus, it was seen that though Ag has a tendency to oxidize, it can be stabilized when in contact with Co. On the other hand, Co which has a damped plasmon in the UV range showed an intense localized surface plasmon called Ferroplasmon in contact with Ag. Thus, the Ag-Co bimetallic system showed symbiotic-like behavior. Based on these findings, bimetallic or multimetallic nanomaterial appear to be good systems to explore for their optical, magnetic and chemical properties and the schematic in Fig. 1.4 illustrates some possible pairs of symbiotic properties that can be influenced and/or investigated using plasmonics.

Motivated by these interesting symbiotic possibilities in plasmonic-ferromagnetic bimetal pairs, the goal of this thesis was to develop a greater understanding of the far field optical behavior of the Ag-Co bimetal pair. This pair of metals is quite unique for several reasons. One, these two metals are virtually immiscible at high (liquid phase) and low temperatures. Two, these metals have a large difference in their electrochemical

tendencies. Three, they have intrinsic strong plasmonic (Ag) and ferromagnetic (Co) properties. Before we provide the necessary background on various aspects pertinent to this thesis, we begin by summarizing the new body of work resulting from this thesis.

(1) We have extended the technique of nanosphere lithography to synthesize large areas of bimetallic Ag-Co nanoparticles, including on electron transparent substrates.

(2) We have developed useful new knowledge on the oxidation kinetics of the Ag-Co system in order to be able to predict the useful plasmonic lifetime of Ag as a function of the Co amount.

(3) We have developed a detailed picture of the dependence of the plasmonic quality factor as a function of energy and size for hemispherical shaped Ag and Ag-Co bimetallic nanoparticles.

(4) Other important results of this thesis include the discovery of a new amorphous transparent oxide material and a new effective medium model to describe the optical behavior of nanoparticles.

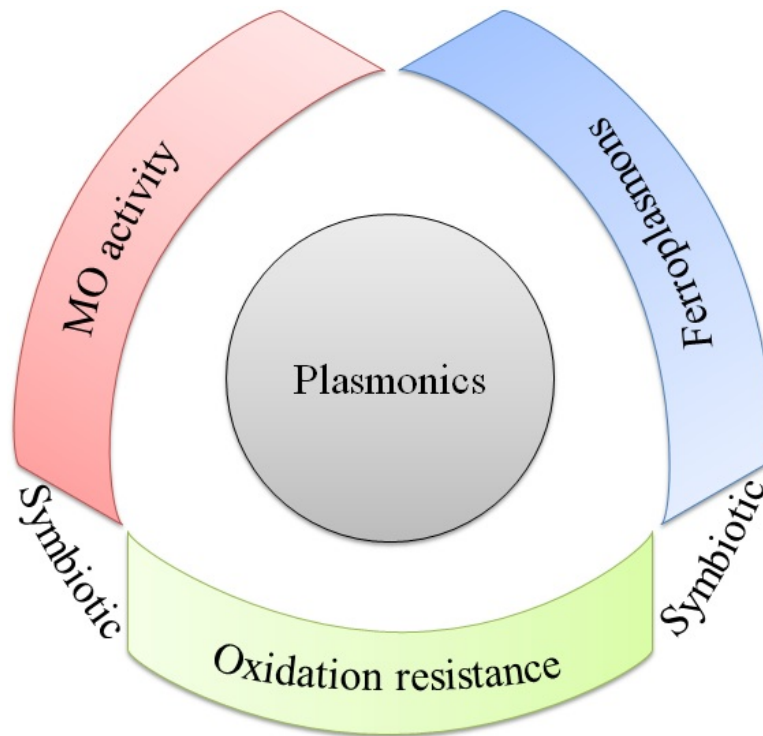


Figure 1.4: Schematic showing the pairs of symbiotic properties studied using plasmonics.

## 1.2 Current knowledge and challenges

In the next few sections we provide the relevant background in key topics of this thesis, such as synthesis, plasmonics, magneto-optical behavior, etc., and also identify the existing challenges that this thesis aims to address.



### 1.2.1 Synthesis of better new plasmonic nanomaterials

(Reproduced with permission from Abhinav Malasi, Jingxuan Ge, Connor Carr, Hernando Garcia, Gerd Duscher and Ramki Kalyanaraman, *Part. Part. Syst. Charact.*, **2015**, 32, 970-978. Copyright 2015 WILEY-VCH Verlag GmbH & Co. KGaA)

As mentioned earlier, the interaction of metallic and other conducting nanostructures with electromagnetic waves can result in important resonant interactions called surface or localized plasmons, which are being utilized in many different applications, including sensing, energy harvesting, data storage, catalysis and more [18, 19, 20, 21, 22]. Progress in the field of plasmonics is primarily being driven by a good understanding of these resonant optical behaviors. In recent years there has been growing interest in correlating the near-field resonant behavior with the far field optical properties as several differences, such as a red shift in resonant position from near to far field has become evident [23, 24, 25, 26, 27, 28, 29, 30, 31, 32, 33]. Near-field studies have also revealed unique phenomenon such as hotspots due to strong electric fields, plasmon coupling effects like hybridization, and Fano resonances [34, 6, 35]. These near-field effects have been instrumental in enabling behaviors such as surface enhanced Raman sensing (SERS), localized plasmon resonance sensing, and Kerr rotation [36, 37, 38]. However, one of the important challenges in this field to discover better new materials that go beyond the traditional plasmonic materials of gold and silver.

One way to accelerate the discovery of better new plasmonic materials is by developing techniques to rapidly characterize the near-field behavior as a function of nanostructure size, shape, spatial arrangement, composition and environmental variables. However, these features can often vary rapidly within the length scale of a few nanometers or smaller. For example, the dipolar coupling between two closely spaced nanoparticles is strongly governed by the size of the gap [39, 40]. Likewise, a small change in shape or composition can strongly influence the plasmonic signal [41]. Therefore, to keep pace with the explosion in the various nanomaterial synthesis techniques, we also need an accurate characterization of nanoscale plasmonic behavior by techniques that can probe and explore the nanomaterials at extremely high spatial as well as spectral energy resolution. Presently, the only known technique that can offer this ability is high resolution transmission electron microscopy (TEM). TEM has been central to the understanding of important properties of plasmonic materials, including the bulk plasmon energies, surface plasmon behaviors, magnetic circular dichroism, and ferropasmons [17, 42, 43, 44, 45]. However, TEM has traditionally been a very time consuming technique due to the constraint placed by requiring electron transparent materials for the analysis [46]. This constraint often limits the number of samples one can investigate, thus restricting the pace of discovery of new plasmonic properties and materials.

Lithographic techniques are well suited towards making large area 2D periodic ordered structures. The formation of these periodic structures involves the three basic steps, i.e. mask formation, material deposition, and mask etching. The technique which will be used in this dissertation to pattern large area 2D periodic ordered structures is called nanosphere lithography (NSL) [47, 48, 49]. This technique involves the self-assembly of a monolayer of spherical beads on rigid substrates or at the air-water interface, which then can be transferred onto a substrate [47, 50, 51, 52, 53, 54, 55, 56, 57]. The biggest challenge using this technique is the presence of large number defects, as shown in Fig. 1.5. The easiest way to control defect density is to control the evaporation rate of the fluid containing the beads [58, 59, 56, 60, 61]. As the fluid

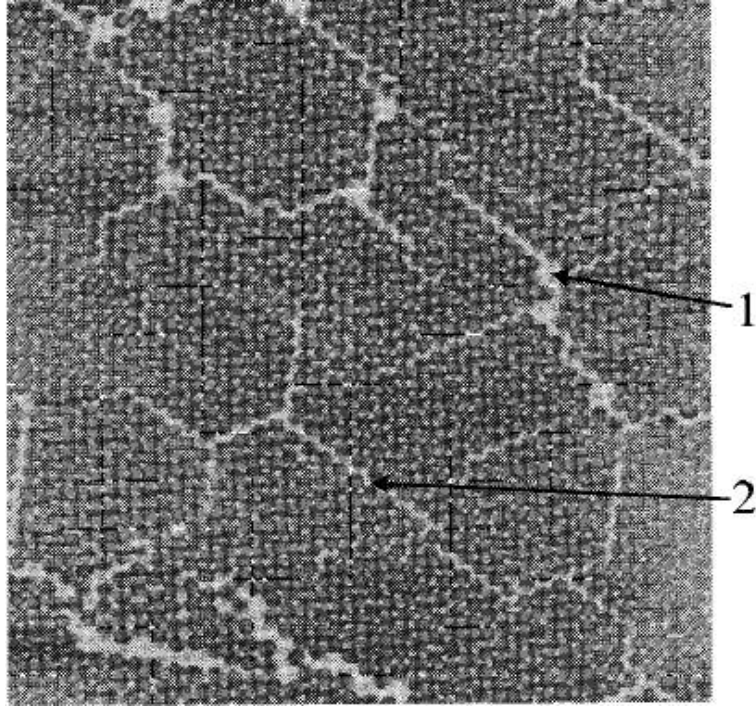


Figure 1.5: AFM micrograph showing the nanoparticle generated from NSL. The location marked as 1 and 2 point to some common defects in the NSL pattern. Figure from ref. [66].

evaporates, it forces the beads to move towards the crystallized bead areas due to the internal flow of the fluid. Other ways are to confine the solution and apply mechanical or physical force by gas flow to form ordered arrangement [62, 63, 64, 65]. Overall, NSL is a fast, effective and robust technique, which does not require clean room facilities and elaborate curing and etching steps for mask formation. Masks used for NSL are the self assembled monolayer of colloidal nanoparticles. The monolayer of these colloidal nanoparticles end up in a hexagonal closed pack arrangement. Once the monolayer template is ready, the metal is deposited through the gaps between the colloidal beads arrangement. Finally, the template is etched out and the hexagonally arranged metal triangular patterns can be seen on the substrate.

Here we propose a way to accelerate nanostructure characterization enabled by localized probing and measurement of plasmonic behavior through a simple and time-efficient experimental approach to produce electron transparent nanostructures. Nanosphere lithography (NSL) has emerged as a good candidate for patterning large areas and is significantly cheaper than traditional lithography techniques such as e-beam or photoresist lithography [47, 67, 48, 49]. Using this technique two-dimensional (2D) periodic patterns can be obtained over large cm scale areas [50, 68, 65]. NSL involves the self assembly of colloidal beads onto a substrate to yield a close-packed arrangement of spheres. This resulting system can then serve as a mask for the subsequent deposition of material using vapor deposition techniques [69]. This process leads to the synthesis of periodically-arranged triangular structures, which then can be converted to semi-spherical shaped particles by thermal annealing [47, 70]. A further modification of the NSL technique that expands its capabilities is by depositing the materials at an angle [48, 49, 71, 69]. The other variants of NSL, used to demonstrate the synthesis of nanostructures made from a combination of different materials,

i.e. multi-component nanostructures are shadow sphere lithography and hole-mask colloidal lithography [69, 72, 73, 74, 75]. However, thus far, NSL has not been applied directly to make electron transparent substrates that can rapidly yield high quality nanostructures for TEM analysis. *In this thesis we utilized NSL and ARNSL on various substrates, including ultrathin carbon substrates in combination with a water-based float-off (FO) process, to yield large area ordered nanostructures.*

## 1.2.2 Metal oxidation investigation by LSPR characterization

(Reproduced with permission from Abhinav Malasi, Ritesh Sachan, Vanessa Ramos, Hernando Garcia, Gerd Duscher and Ramki Kalyanaraman, *Nanotechnology*, **2015**, 26, 205701. Copyright 2015 IOP Publishing)

The role of interaction of light with noble metal dust embedded in glass can be dated back to 4th century, where the stained glass was just used for its aesthetic value. The glass used in architecture and crafts contained gold and silver dust which gave it some of the unique properties which could only be deciphered in the mid 19th century. The first work reported on metal-light interaction can be dated to 4th century, but its scientific understanding was given by Michael Faraday in 1856. In his work, he proposed that the beautiful coloration of the ruby glass was due to the fine silver and gold dust. Then in early 20th century, Gustavo Mie formulated a theory which showed the interaction of light with metal nanoparticles smaller than the wavelength of light [76]. Since then, the use of the theory given by Mie has been an integral part of the study of interaction of light with metal particles comparable to wavelength of light. The phenomenon of the coloration of the glass came to be called as plasmonics. The extinction cross-section defined by Mie for nanoparticles much smaller than the wavelength of light is given as [77]:

$$\sigma_{ext} = \frac{24\pi^2 \epsilon_m^{3/2} d^3}{\lambda} \frac{\epsilon''(\omega)}{[\epsilon'(\omega) + 2\epsilon_m]^2 + \epsilon''(\omega)^2} \quad (1.1)$$

where,  $\epsilon_m$  is the dielectric of the surrounding medium,  $\epsilon'$  and  $\epsilon''$  are the real and imaginary part of the complex dielectric function of the metal nanoparticle,  $d$  is the nanoparticle diameter and  $\lambda$  is the wavelength of light. The condition for the existence of the plasmon is when the extinction cross-section reaches the maximum. It can only be maximized when  $\epsilon'(\omega) + 2\epsilon_m = 0$ . So, by changing the external dielectric medium, the LSPR of the nanoparticle can be tuned. The size dependence of the nanoparticle can be incorporated with the size correction in the dielectric function of the metal nanoparticle. The size correction incorporates the various electron-electron, electron-phonon interactions. The modified complex dielectric function can be written as [78, 79]:

$$\epsilon(\omega, d) = \epsilon_{bulk}(\omega) + \omega_p^2 \left( \frac{1}{\omega^2 + \Gamma_\infty^2} - \frac{1}{\omega^2 + \Gamma(d)^2} \right) + i \frac{\omega_p^2}{\omega} \left( \frac{\Gamma(d)}{\omega^2 + \Gamma(d)^2} - \frac{\Gamma_\infty}{\omega^2 + \Gamma_\infty^2} \right) \quad (1.2)$$

and

$$\Gamma(d) = \Gamma_\infty + \frac{Av_F}{d} \quad (1.3)$$

where,  $\omega$  is the frequency,  $\omega_p$  is the plasmon frequency,  $\epsilon$  is the complex dielectric function,  $\Gamma_\infty$  is the bulk electron relaxation time,  $\Gamma(d)$  is the size corrected electron relaxation time,  $d$  is the diameter of the nanoparticle,  $v_F$  is the fermi velocity and  $A$  is the size correction factor, equal to 2 for spherically shaped nanoparticles [78].

Understanding the stability of nanoparticles in various environments is of fundamental interest due to the large number of applications in diverse fields such as plasmonics, catalysis, energy harvesting, data storage, optoelectronics and biotoxicity [80, 22, 20, 21, 81, 82, 83]. In the field of plasmonics, this study is particularly relevant because, out of the three known noble and plasmonic metals, Au, Ag and Cu, the latter two degrade rapidly in contact with air and special efforts have to be made to prevent this [84, 85, 86]. It is also well established that reducing a materials dimensions can often lead to changes in its physical and chemical behaviors. In this regards, while the bulk oxidation and corrosion behavior of metals has been well studied, similar data for metallic nanoparticles is lacking. In the last decade, several techniques have been employed to probe nanoscale oxidation, including x-ray scattering [87, 88], electron energy-loss spectroscopy [89], optical spectroscopy [90, 16, 91, 84], surface enhanced Raman sensing [87, 86, 92], and cyclic voltammetry [93].

Recently, it has been shown that the LSPR signal from Ag nanoparticles in contact with Cobalt (Co) metal decays slowly compared to pure Ag nanoparticles [16]. This was attributed to the preferential sacrificial behavior of Co metal. However, the lifetime of the Co-Ag bimetal was not determined. *Building on this previous work, in this thesis we investigated the kinetics of oxidation to ascertain the lifetime of Ag plasmons and dependence on the bimetal composition.* .

### 1.2.3 Far field quality factor and quantum efficiency of plasmonic nanoparticles

While the plasmon frequency is one of the central characteristics of an LSPR, the spatial bandwidth  $\Delta\lambda_{SPR}$  often determines the ultimate usefulness of a metal in plasmonic applications. In fact, this is one of the primary reasons why Ag is the most important plasmonic metal, as we discuss next. For a free electron gas the dielectric function in the Drude-Lorentz-Sommerfeld model can be expressed as [94]:

$$\epsilon_m(\omega) = 1 + \frac{\omega_p^2}{\omega^2 + i\gamma\omega} \quad (1.4)$$

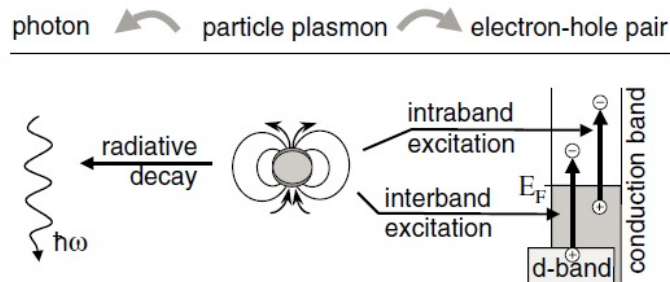


Figure 1.6: The plasmon decay of metal nanoparticle can be interpreted by a two-level excitation model. Figure taken from ref. [95].

The plasmon frequency,  $\omega_p = ne^2/\epsilon_0 m^*$ , is determined by the electron density  $n$ , the electron effective mass  $m^*$ , the damping constant  $\gamma$  and the permittivity of vacuum  $\epsilon_0$ . The damping constant  $\gamma$  determines the rate at which the plasmon dephases, i.e. the electrons in the collective oscillation lose coherence, and is responsible for the reduction in intensity and broadening of the plasmon peak. The contributing factors to the bandwidth may be divided into intrinsic and extrinsic parts. The intrinsic part is a material specific property that arises from various electron scattering processes. The total dephasing rate can be expressed via Mathiessen's rule as the sum of the reciprocal of all relaxation times  $\tau$  as,

$$\gamma = \sum \tau_i^{-1} = \frac{1}{\tau_{e-e}} + \frac{1}{\tau_{e-ph}} + \frac{1}{\tau_{e-d}} + \frac{1}{\tau_{e-m}} \dots \quad (1.5)$$

where e-e, e-ph, e-d, e-m correspond to the electron-electron, electron-phonon, electron-defect, and electron-magnon scattering processes. Inelastic scatterings result in intra- and inter-band transitions, which contribute to plasmon energy loss. An alternate view of the decay of plasmons is based on an analogy with molecular spectroscopy. As shown by Heilweil et al and Link and El-Sayed [96, 41], the interaction of incident EM waves with the free electrons can be interpreted as excitations in a two-level system and subsequent decay via radiative and non-radiative transitions, as depicted in Fig. 1.6. In this model, the total dephasing time  $T_2$  is expressed as

$$\frac{1}{T_2} = \frac{\Delta\omega_{LSPR}}{2\pi} = \frac{1}{2T_1} + \frac{1}{T_2^*} \quad (1.6)$$

where  $\Delta\omega_{LSPR}$  is the frequency bandwidth of the LSPR,  $c$  is the velocity of light,  $T_2^*$  is the dephasing time due to elastic scattering processes, and  $T_1$  is the energy (population) relaxation time via radiative and non-radiative processes.

The usefulness of the plasmonic nanomaterial can be quantitatively described partly by the location of LSPR (in visible wavelengths or not) but largely by the quality factor of the plasmons. The quality factor, is a measure of the sharpness of the plasmon resonance, and captures the enhancement of the local electric field due to excitation of the plasmons by the incident EM field [97]. One of the simplest ways to compare the quality of LSPR amongst different materials is to evaluate the behavior of spherical nanoparticles in air within the quasistatic approximation, i.e. when the incident EM wavelengths are much larger than the particle size. In this approximation, the plasmonic quality factor is obtained directly from the dielectric function of the metal as [97]:

$$Q_{LSPR} = \frac{-\epsilon'}{\epsilon''} \quad (1.7)$$

where,  $\epsilon'$  is the real part and  $\epsilon''$  is the imaginary part of the complex dielectric function of the metal. Based on this, one can design a plasmonic system in at least one of two ways. The first is to select the appropriate material, i.e. one with the largest quality. Using the equation, Blaber et al. calculated the plasmonic quality factor for all the elements and color coded the periodic table according to quality factor, as shown in Fig. 1.7. From this table an important limitation became apparent in that, there are very few metals, i.e. virtually only the noble metals (Ag, Au, Cu), which have strong plasmonic responses in air ambient and in the visible wavelengths. This limitation has led to extensive research on alternate new materials for plasmonic

Element		* Frequency is at the limit of the available data # Low frequency data not included														B	C	Max Qlsp Key
Frequency of Max QLSP	Maximum QLSP															Al	Si	4.00-5.99
Li	Be																	0.00-2.99
0.14*	0.20																	3.00-3.99
<b>28.82</b>	<b>3.58</b>																	4.00-5.99
Na	Mg															11.00		6.00-9.99
1.44	4.00															<b>13.58</b>		10+
<b>35.09</b>	<b>9.94</b>																	
K	Ca	Sc	Ti	V	Cr	Mn	Fe	Co	Ni	Cu	Zn	Ga	Ge	As	Se			
1.05	0.65*	0.3*	0.20	0.36	0.30	0.07*	0.10*	0.10*	0.15	1.75	3.60#	8.30						
<b>40.68</b>	<b>3.63</b>	<b>1.02</b>	<b>2.58</b>	<b>4.27</b>	<b>2.16</b>	<b>1.16</b>	<b>2.48</b>	<b>2.69</b>	<b>2.71</b>	<b>10.09</b>	<b>3.59</b>	<b>3.41</b>						
Rb	Sr	Y	Zr	Nb	Mo	Tc	Ru	Rh	Pd	Ag	Cd	In	Sn	Sb	Te			
0.81	0.36*	1.48*	3.00	0.55	0.38		0.10*	0.30	0.10*	1.14	0.65#	5.10	2.25	3.50				
<b>21.90</b>	<b>2.85</b>	<b>1.41</b>	<b>1.16</b>	<b>3.39</b>	<b>5.38</b>		<b>2.03</b>	<b>2.10</b>	<b>6.52</b>	<b>97.43</b>	<b>3.63</b>	<b>4.60</b>	<b>3.50</b>	<b>1.33</b>				
Cs	Ba	Lan	Hf	Ta	W	Re	Os	Ir	Pt	Au	Hg	Tl	Pb	Bi	Po			
0.51*	1.91		0.52*	0.58	0.30	0.10*	0.10*	0.40	0.35	1.40	4.20	3.20	5.95	3.50				
<b>11.20</b>	<b>0.91</b>		<b>0.79</b>	<b>5.25</b>	<b>4.96</b>	<b>4.99</b>	<b>6.12</b>	<b>2.55</b>	<b>1.96</b>	<b>33.99</b>	<b>2.20</b>	<b>2.71</b>	<b>3.07</b>	<b>1.15</b>				

Figure 1.7: Plasmon quality factor of the elements in the periodic table. Figure from ref. [97].

applications, as discussed in recent reviews by West et al., Blaber et al. and Naik et al. [97, 80, 98]. Specifically, they have discussed different combinations of binary alloys of noble metals, transition metals and noble-transition metals [97, 80]. In addition, they have also discussed the intermetallics of alkali metal binary systems, noble metal binary systems, alkali-noble metal combinations, binary intermetallics of Group 13 and ternary intermetallics [97, 80]. However, one of the common problems faced with pursuing either alloys or intermetallics is that the imaginary part of the complex dielectric function becomes greater than that of the individual metal constituents, resulting in a much larger value of the loss or  $\epsilon''$ , decreasing the quality factor. Recently, some other possible materials showing plasmon quality comparable to Au have become important, such as nitrides of titanium and zirconium [98].

A second approach to tuning and/or improving the plasmonic quality factor is to modify the shape, size, and surrounding environment of the material. To understand how these factors influence the quality factor, it is illustrative to first define the more practical measure of the plasmonic quality based on readily measurable quantities, which are the LSPR wavelength ( $\lambda$ ) and bandwidth ( $\Delta\lambda$ ), i.e.  $Q = \frac{\lambda}{\Delta\lambda}$  or in terms of the energetic parameters,  $Q = \frac{E_{res}}{\Gamma}$ , where  $E_{res}$  is the energy position of the plasmonic resonance and  $\Gamma$  is the energy bandwidth of the resonance. Based on this latter form, the weakening of plasmonic resonance can be attributed directly to the various loss mechanisms that contribute to the dephasing of the coherent plasmonic oscillations. As mentioned previously, and shown in Fig. 1.6, the plasmonic excitation in the two-level model (Eq. 1.6) can decay due to a combination of elastic dephasing of the oscillations, i.e. scattering events in which the electrons do not lose energy, and inelastic contributions coming from transitions of electrons to states inside (intraband) or outside (interband) its energy band and by radiation of photons. The challenges in optimizing a nanostructure to show the best quality factor comes because of a complicated interplay between the size and shape of the particle and the energy of the resonance. To understand this, it is illustrative to first understand the contributions from the various dephasing pathways, as summarized in Fig. 1.8.

1. Elastic scattering of electrons contributing to  $T^*$  can occur through a variety of processes such as

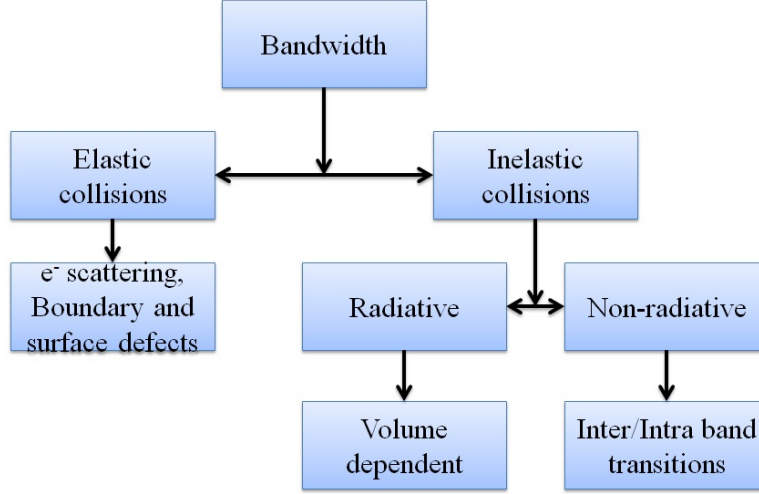


Figure 1.8: *Different loss mechanisms responsible for the broadening of the plasmon bandwidth.*

scattering by other electrons (intrinsic to the metal) and defects such as boundaries and surfaces. An important length scale is the characteristic electron scattering length or the electronic mean free path ( $l_e$ ). If the density of defects and/or the particle size become comparable to or smaller than  $l_e$  then the elastic scattering rates will increase over the metals intrinsic value increasing the dephasing rate, i.e. lower quality resonance. For strongly plasmonic metals like Ag and Au, the  $l_e$  is typically  $\sim 40$  nm, suggesting that plasmonic signals from particles with size  $< 40$  nm will show significant broadening due to additional elastic scattering from the surface of the nanoparticle [99].

2. The inelastic contribution from the non-radiative process is primarily governed by the location of the resonance energy in the context of the imaginary component of the dielectric function. In the quasi-static approximation, i.e. when the EM wavelength is comparable to or larger than the particle diameter  $D$ , the oscillations can be envisioned as a coherent collective oscillation of the electrons and the frequency-dependent polarization  $\alpha(\omega)$  of a spherical metal nanoparticle can be written as [3]:

$$\alpha(\omega) = \frac{\pi}{2} D^3 \frac{\epsilon_m(\omega) - \epsilon_h(\omega)}{\epsilon'_m(\omega) + i\epsilon''_m(\omega) + 2\epsilon_h(\omega)} \quad (1.8)$$

where  $\epsilon_h(\omega)$  and  $\epsilon_m(\omega)$  are host and metal dielectrics, respectively. Since the metal can have a negative value of the dielectric function, Mie or Frohlich resonance condition for the appearance of the plasmons is achieved when  $\epsilon'_m(\omega) = -2\epsilon_h(\omega)$ , for a non-absorbing dielectric host, like glass [100, 101]. Under this condition, the singularity of the polarization function is prevented by the non-zero term coming from the imaginary component of the metal dielectric function, i.e.  $\epsilon''_m(\omega)$  and from this it can be seen that the larger the value of the imaginary component, broader will be the damping, i.e. low quality plasmons. The behavior of the dielectric function for Ag and Co metals are shown as a function of energy in Fig. 1.9. From this it is evident that Ag has a rapid decrease in the loss (i.e. imaginary component) at  $\sim 320$  nm. corresponding to its interband transition. Ag nanoparticles for which the resonance energy is  $> 310$  nm could be expected to show much smaller interband loss as

compared to particles whose resonant energy is  $<310$  nm.

3. For particle sizes well beyond the mean free path, inelastic loss due to radiation of photons become a strong contributor to the overall dephasing and under simple approximations this contribution is observed to be linearly increasing with the volume of the particle [95].

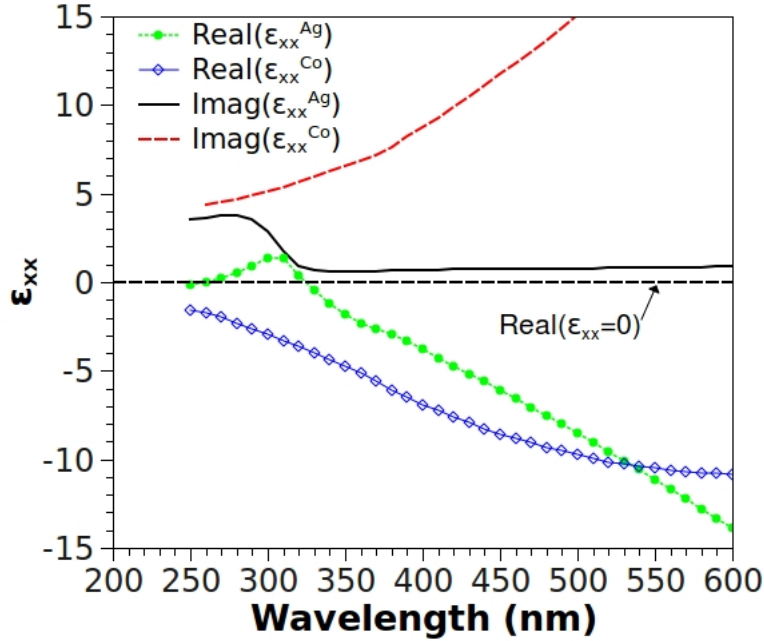


Figure 1.9: *The real (lines with symbols) and imaginary (dashed curves) components of the energy-dependent dielectric functions for Ag and Co. Data was taken from ref. [102]*

Based on the relative magnitudes of the elastic and energy relaxation times, one can characterize the behavior of different nanoparticles. Among the extrinsic factors, particle size, shapes, and interfaces (grain boundary, chemical effects, etc.), play important roles. For example, since radiation damping is more important for larger particles, whereas scattering from the surface atoms is dominant in smaller particles, [103] hence intermediate size could yield the best quality factor. Secondly, bandwidths become narrower with increasing aspect ratio (rod shaped) of the nanoparticles because of smaller sample volume and the energy shift of the resonance [95]. Third, interface scattering is larger in polycrystals compared to single crystals because of grain boundary scattering. When embedded or in contact with another material, a different chemical interface also contributes to additional scattering [104], especially for the smaller particle sizes. In arrays of nanoparticles, dipolar and higher order interactions modify both plasmon frequency and linewidth [105, 106].

Due to the complicated interplay of size, shape, and dielectric, exhaustive investigations related to controlling the quality factor of the localized plasmons are not widely available in literature. One of the first works to use size and shape to improve the quality factor and the quantum scattering efficiency, which is defined as  $\eta = \frac{1/T_{IR}}{1/T_{iR}+1/T_{iNR}}$ , was performed by Sonnichsen et al. in which Au nanorods were used to shift



the resonance energy far from the lossy interband transitions without a significant increase of the particle volume over that of nanospheres [95]. Their result is shown in Fig. 1.10 and it established that size and shape were critical for enhancing the quantum efficiency.

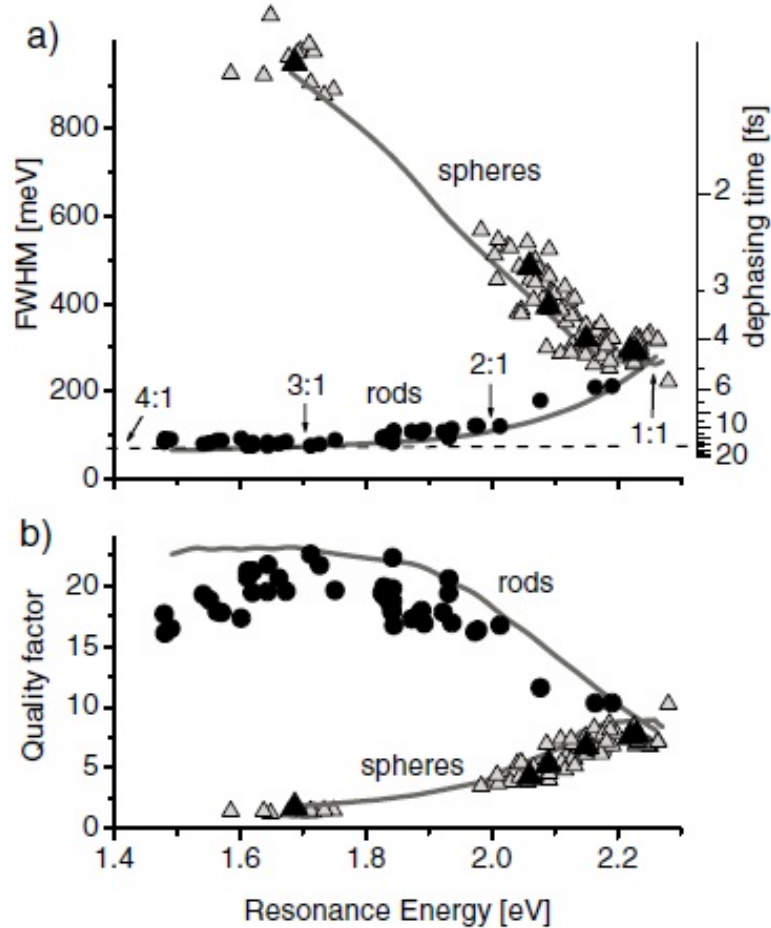


Figure 1.10: (a) Comparison of the bandwidth and the dephasing time of Au nanospheres with nanorods as a function of plasmon resonance energy. (b) Comparison of the quality factor of Au nanospheres with nanorods as a function of plasmon resonance energy. Figures taken from ref. [95].

However, such studies have not been performed for bimetallic systems. More importantly, a detailed investigation of the plasmonic quality factor and quantum efficiency in complex shapes such as hemispheres and triangles is lacking. *In the present work, we performed a detailed size and environment dependent experimental study of plasmonic quality of Ag hemispheres.* We also compared pure Ag to bimetallic Ag-Co of hemispherical geometry and established that, under certain conditions, the AgCo bimetal system can yield higher quality factor as well as better quantum efficiencies than pure Ag.

## 1.2.4 Improved effective medium model incorporating multipolar contributions

(Reproduced with permission from Abhinav Malasi, Ramki Kalyanaraman and Hernando Garcia, *J. Optics*, **2014**, 16, 065001. Copyright 2015 IOP Publishing)

Materials with heterogeneity in structure and composition and which show useful optical properties are all around us. From the perspective of advanced technologies, heterogeneous materials made from nanoscale components that scatter light resonantly, such as by plasmonic effects, are finding use in many different fields, including for ultrasensitive biological and chemical sensing by plasmonics [107, 108, 109], for tailored light scattering to improve solar cell efficiency [20, 110], and for coupling of plasmonics with magnetic Kerr effect for various applications [111, 112, 113, 114]. The design of such materials and the predictions or evaluation of their optical performance, such as by knowledge of the dielectric function, and scattering and absorption cross-sections, can be achieved either through a complete solution of Maxwell's equations or by approximate solutions via effective medium approximations (EMA). The benefit of the former is a highly accurate quantitative picture of the electromagnetic fields but at the expense of less physical insight and large computational expense [115]. In contrast, EMA models can provide a fast and easy route to obtaining the central physical behaviors of complicated heterostructure systems as shown by several studies [116, 117, 118, 119, 120, 121, 122, 123].

The fundamental models used to calculate plasmonic properties of scattering objects, such as metal inclusions, are those given by Rayleigh [124] and Mie [76]. The Rayleigh solution predicts the optical behavior correctly for inclusions much smaller than the incident wavelength [124], where the field inside the inclusion is uniform. The optical response from a metal inclusion of arbitrary size in an otherwise homogeneous and transparent media was solved by Mie [76]. The Mie solution uses the variation of field inside the inclusions which are large or comparable to the wavelength of incident light, thus predicting more accurately the plasmonic behavior for large inclusions. Recently, Lukyanchuk et. al.[125] showed that the Rayleigh approach deviates for materials having low dissipation rate, and in this case, the light scattered by a small spherical particle can be explained by Mie theory. The exact solution to the Maxwell equations are approximated in accordance with the size parameter being much less than the incident wavelength. This model predicts the multipole resonances appropriately, a feature that becomes increasingly important as the particle size increases [126, 127, 3]. However, these models only give accurate information on the behavior of scattering and absorption dependence on wavelength of incident light for a *single* particle system.

Many approaches to incorporate scattering and absorption to describe heterogeneous systems by an effective dielectric function ( $\epsilon_{eff}$ ) have been done in the past. For example, Foldy [128] proposed that the incident and scattering wave combined to form a wave that travels uniformly in the composite without scattering and having a different group velocity from that of incident wave. This wave experiences reflection and refraction as well as showing coherent scattering. In the analysis he provided an expression for the group velocity and the wave vector, but not a formal definition of  $\epsilon_{eff}$ . In the work by Lewin [129], an expression for the dielectric function of a composite was found using Fresnel formulas for the reflection and transmission coefficients and using the first term of the coefficient for the scattering wave from the Mie formalism. Further he showed that the permittivity of the system has volumetric dependence but not the particle size dependence. Lax [130] on the other hand used tools from scattering theory to define a propagation constant in

accordance with the optical theorem, but no expression was derived. An approach similar to the one that we are proposing in this work, was taken by Doyle [131]. Doyle calculated the polarizability of a small metal particle using the scattering coefficients from Mie theory and combined the Clausius-Mossotti equation to obtain an effective dielectric constant and in this way succeeded in introducing size-dependence in an effective dielectric function. Dungey & Bohren [132] refined the calculation by incorporating the coupled dipole approximation with the polarizability expression calculated by Doyle [131]. This new method gave results that were comparable with the experimental extinction data. It is worth mentioning here that in Dungey & Bohren's approach only extinction and scattering coefficients were calculated and there is no definition of a effective dielectric function of the system. The current status is that existing theories either ignore one or more important parameters, such as size dependence and influence of the higher order multipoles, or do not explicitly discuss the effective dielectric function of the system, and in the event they do incorporate all effects, remain computationally expensive.

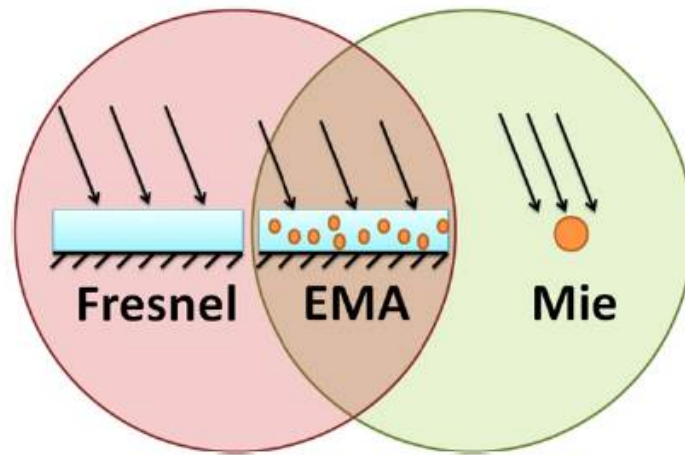


Figure 1.11: *Schematic summarizing the theme of bridging Mie with Fresnel theories using EMA. Figure taken from ref. [133].*

*In this thesis we developed an EMA approach to predict the optical behavior of heterogeneous materials in which inclusions, such as nanoparticles can have size-dependent optical responses. In other words, we attempted to bridge the Fresnel technique with the Mie solution, which includes size-dependent behaviors, via an EMA approach, as depicted in Fig. 1.11.*

### **1.2.5 Discovery of iron-based amorphous material with high transparency and Hall mobility**

(Reproduced with permission from Abhinav Malasi, Humaira Taz, Annette Farah, Maulik Patel, Benjamin Lawrie, Raphael Pooser, Arthur Baddorf, Gerd Duscher and Ramki Kalyanaraman, *Scientific Reports*, **2015**, accepted. Copyright 2015 Nature Publishing Group)

Materials which combine large optical transparency with electronic conductivity are of great scientific interest, partly due to a dearth of such materials, and largely due to their potential for applications. For

example, solar cells and smart windows rely upon having a transparent front conductor, while thin film transistors made from transparent semiconductors are central to flat panel display, flexible optoelectronics devices, and organic light emitting devices [134, 135, 136]. In 2004 a new era in the design and application of these materials was ushered in when the Japanese team of Nomura et al showed the room temperature fabrication of a high-performing thin film transistor made from Indium-based amorphous oxide semiconductor material [137]. This report has led to widespread interest in amorphous conducting and semiconducting oxide materials because it demonstrated the capability of combining high optical transparency with high electronic conductivity and hall mobility ( $>10 \text{ cm}^2/\text{V-s}$ ), which greatly exceeded the value for amorphous Si ( $<1 \text{ cm}^2/\text{V-s}$ ) [135]. The amorphous microstructure makes such material extremely attractive because they can be synthesized at room temperature thus reducing processing cost and complexity, can eliminate non-uniformity arising from defects such as grain boundaries seen in polycrystalline materials, and can show better tolerance to mechanical stress as compared to polycrystalline or crystalline materials [138]. Presently, all known high mobility ( $>10 \text{ cm}^2/\text{V-s}$ ) amorphous oxide materials, such as In-Ga-Zn oxide (a-IGZO) and Zn-In-Sn oxide, are made by combining two or more oxides which have extremely high mobility arising from their metal cations having an oxidation state configuration given by  $(n-1)d^{10}ns^0$ , i.e. oxides with an s-conduction band. As postulated by Hosono et al and verified by others, the large spatial extent and orientation independence of the spherically symmetric  $ns$  orbitals can result in extremely high mobility and conductivity behavior [139, 140, 141, 142, 143].

*In this thesis we discovered the first evidence of a ternary amorphous oxide semiconductor that goes beyond this existing paradigm of requiring metal cations with  $(n-1)d^{10}ns^0$  to show good conduction.*

### 1.3 Outline of thesis

The bulleted list summarizing the remainder of the thesis content is provided here.

- In Chapter 2 we discuss the various experimental and computational methods and techniques used throughout this thesis
- In Chapter 3 we detail the NSL synthesis of bimetal nanostructures
- In Chapter 4 we describe the studies of metal oxidation kinetics using plasmonics
- In Chapter 5 we describe the studies of plasmonic quality factor in nanoparticles
- In Chapter 6 we discuss the new effective medium model developed
- In Chapter 7 we describe the discovery of a new amorphous oxide material
- In Chapter 8 we summarize the thesis and identify potential future problems to address

# Chapter 2

## Methods and techniques

The various experimental and modeling techniques used to synthesize the various nanomaterials, and to characterize the morphology and optical behavior are detailed in this chapter.

### 2.1 Experimental techniques involved in synthesis and characterization

#### 2.1.1 Selection of materials

Since this thesis was focussed primarily on bimetal systems, Ag metal along with ferromagnetic metals were used. Ag has intrinsic plasmonic properties but is susceptible to degradation in ambient environment [97, 144, 41, 145, 146, 86, 92]. The ferromagnetic materials like Co and Fe have strong magnetic properties but no strong plasmonic properties in the visible energy [147]. The combination of Ag with metals like Co and Fe is also unusual in the sense that these combinations are highly thermodynamically immiscible systems which simplifies the synthesis of bimetallic structures of various morphologies through thermal routes [148, 149, 150, 151]. The thermodynamic phase diagram for these bimetals are shown in Fig. 2.1.

The second material that was investigated in this thesis was Terfenol-D, which is a ternary alloy of  $(Tb_{0.3}Dy_{0.7})Fe_{1.92}$  and is a highly magnetostrictive material. We investigated the optical, magnetic and electronic transport properties of this material, which resulted in the discovery of amorphous transparent semiconductor.

#### 2.1.2 Synthesis techniques

##### 2.1.2.1 Substrate preparation

Substrates of quartz and thermally grown 400 nm of  $SiO_2$  on Si substrates were cut into pieces of 1x1  $cm^2$  area and were then cleaned by sequentially sonicating them in acetone, isopropanol and deionized water (DI). Then cleaned substrates were then dried and stored in sample boxes for future use. The carbon substrates were prepared by cleaving the fresh surface of mica (V-2 grade) using a scotch tape and then sputter coating a thin layer of carbon in the range of 10-30 nm using a SPI inc. carbon coater.

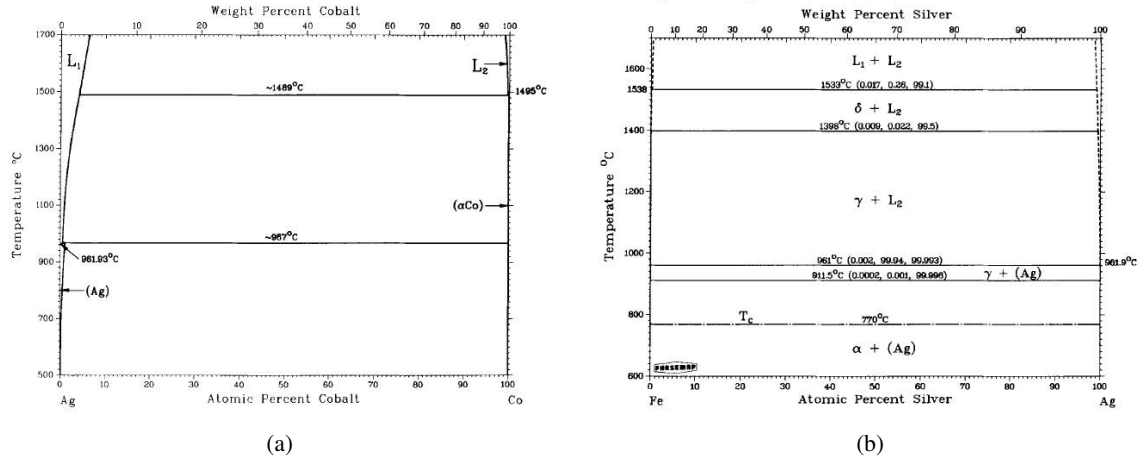


Figure 2.1: The equilibrium phase diagrams for (a) Ag-Co [150] and (b) Ag-Fe systems [149].

### 2.1.2.2 NSL mask formation

The PS masks were fabricated in two different ways. The first method involved spin coating of PS beads solution and the other one involved making monolayer of PS beads at air-water interface. For making a monolayer with the help of spin coating, PS beads solution of 500 nm size were mixed with equal volume of Triton-X and methanol mixture (1:400 v/v). After this, the solution was spincoated on different substrates using a programmable spincoater from Laurell Technologies Corporation model number WS-400BZ-8TFM/LITE. The spincoating was done in three different stages. The coating was started at 400 rpm for 10 sec to spread the PS beads uniformly on the substrate and then was ramped up to 800 rpm for 2 minutes to remove the excess material, and finally ramped up to 1400 rpm for 10 sec to remove the bead accumulation occurring at the edges [152]. After the spincoating, the sample was left to dry under controlled environment (temperature maintained at  $22 \pm 1$  with relative humidity at  $40 \pm 5\%$ ).

The other technique involves the formation of PS monolayer at air-water interface [50, 65]. Sodium dodecyl sulfate (SDS) was dissolved in water to make a solution of 0.3 M concentration. After which equal volumes of PS beads solution (sizes 100 or 200 nm) were mixed with ethanol. The SDS solution was filled in a glass trough and the PS beads solution was poured onto a glass slide inclined at  $\sim 45^\circ$  angle and partially immersed in the trough. A syringe was used to pour the PS solution on the glass slide. Using this technique, large patches of PS monolayer of size in cm range were formed at the air-water interface. The PS monolayers were transferred onto the substrate by scooping the PS monolayer and then were left for drying at an inclination angle of  $2^\circ - 4^\circ$  in a controlled environment. Using this technique, continuous monolayer patches of cm square area can be achieved. Fig. 2.2 (a) shows the apparatus used for the PS template formation. Fig. 2.2 (b) shows the large monolayer floating at the air-water interface.

### 2.1.2.3 Thin film deposition

Metal films were deposited using electron beam evaporator or pulsed laser deposition (PLD). The base pressure of the vacuum chamber for deposition of metal film was about  $1 - 5 \times 10^{-8}$  Torr. The Ag and Fe

metals were deposited using a Mantis QUAD-EV-HP e-beam source while Co was deposited using Tectra e-beam source. The substrates used for deposition composed of glass, quartz, 400 nm SiO<sub>2</sub> on Si substrates, thin carbon film on mica and on NSL substrates. The film thicknesses and surface roughness of the as deposited metal films were measured by Nanonics Multiview 1000 atomic force microscope (AFM) working in contact mode. The metals used for the different studies undertaken in this dissertation are Ag, Co, Fe and Terfenol-D. All the metals except Terfenol-D were deposited using electron beam evaporator. The film thicknesses deposited were in the range of 1 to 75 nm.

#### 2.1.2.4 *Laser irradiation for dewetting*

The thin metal films were irradiated using 9 ns pulsed Nd:YAG laser (Spectra physics model Lab-150-50) operating at 266 nm with a repetition rate of 50 Hz. The laser beam has a Gaussian profile. The laser irradiation was done in ambient air and at normal incidence to the substrate plane. The laser energy density was chosen in a way to heat the metal film at its melt threshold. By controlling the laser energy density, number of laser pulses and film thickness, a variety of nanostructures can be formed. The final outcome of the laser irradiation of thin metal films is the hemispherically shaped monodispersed NPs following various intermediate stages. Fig. 2.3 shows the final NPs achieved by dewetting of a monolayer and a bilayer.

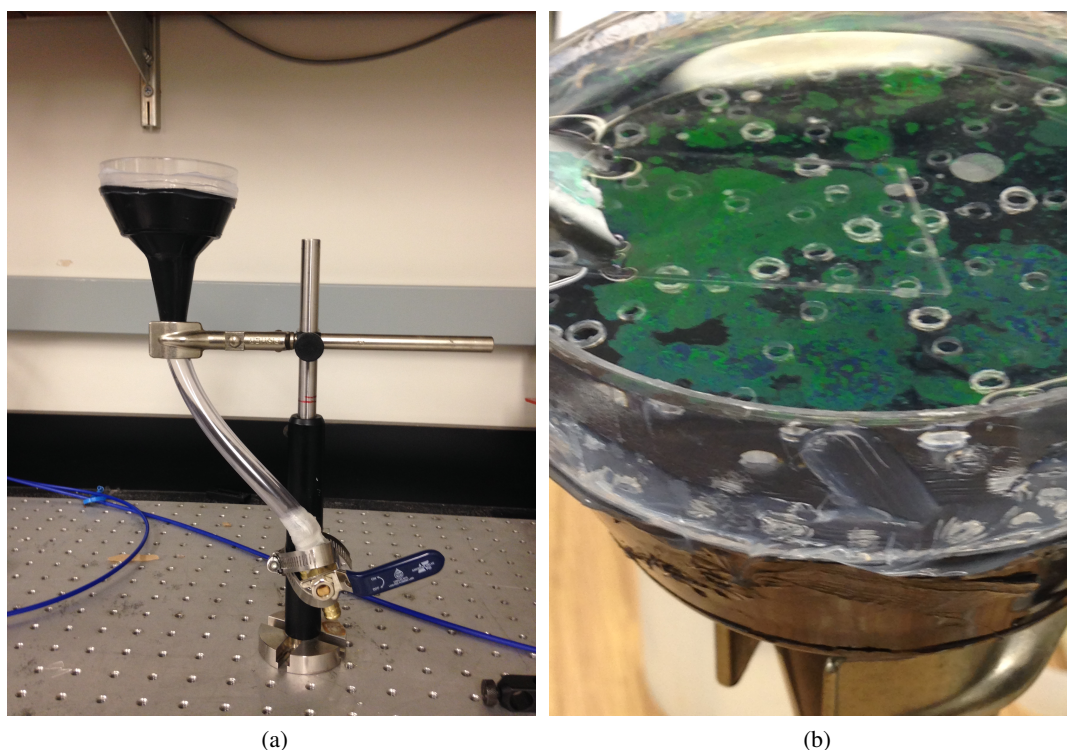


Figure 2.2: (a) NSL setup built to make PS monolayer templates at the air-water interface. (b) Large monolayer coverage area of PS mask formed at the air-water interface.

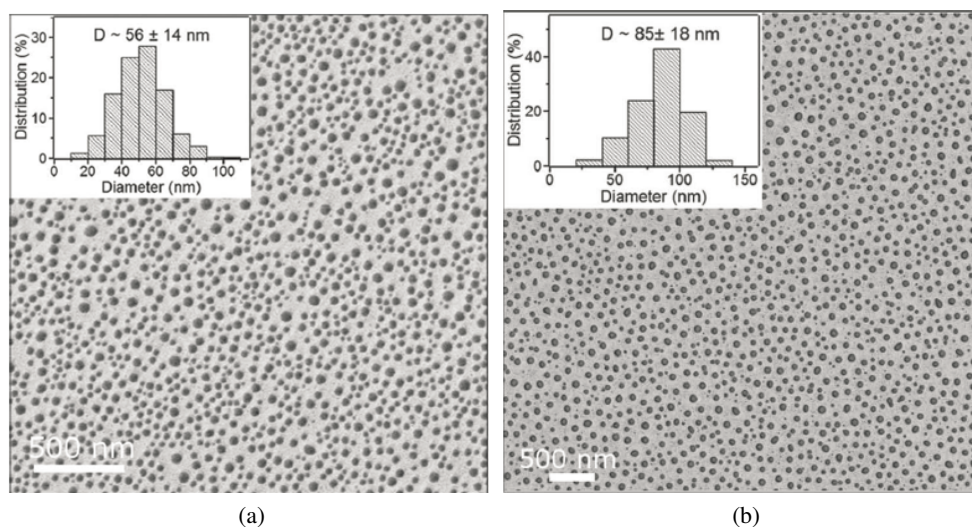


Figure 2.3: SEM image for the (a) hemispherically shaped Ag NPs and (b) bimetallic Co-Ag NP [16].

Bimetallics of Co-Ag and Fe-Ag were synthesized and studied for their oxidation degradation. By changing the film thickness of individual metal films, the amount of the metals in a single nanoparticle could be tuned and thus the interface area between the metals could be changed [15, 16, 17, 153]. These as-synthesized bimetallics were then studied for oxidation stability in ambient environment. The size and morphology of the Co-Ag bimetallic NPs were controlled by the individual metal film thicknesses and the order in which the films were deposited [154, 15, 16, 17, 153]. Fig. 2.4 shows that by controlling the individual metal film thickness and the order in which the metal films are deposited a large parameter space can be achieved [15].

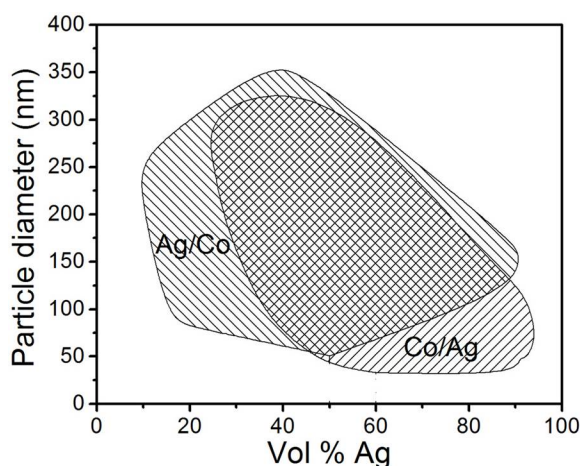


Figure 2.4: Shows the parameter space for the Ag-Co bimetal system [15].

The etched out NSL templates with triangular nanostructures were laser treated to change the nanostructure morphology. Fig. 2.5 shows the SEM images of Ag nanotriangle shape transformation to the semispherical nanoparticles after laser treatment.



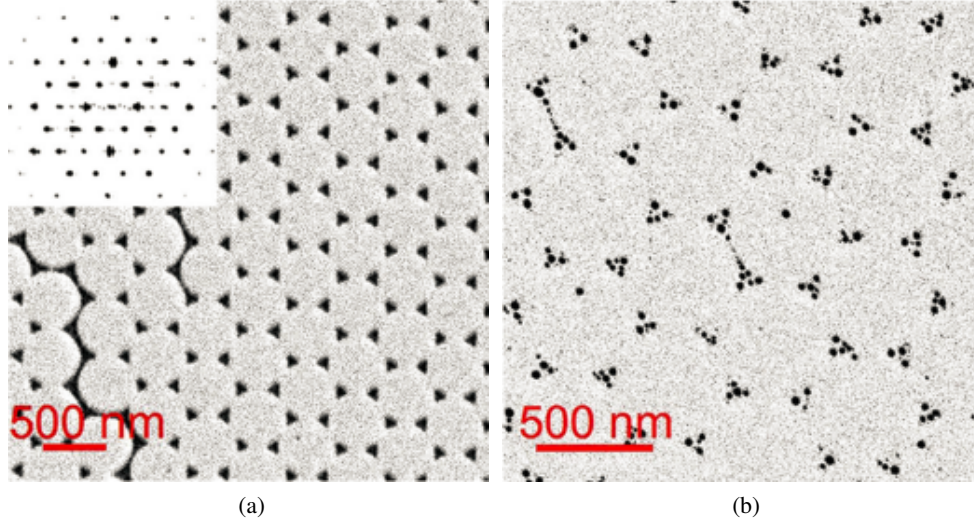


Figure 2.5: SEM image of the nanotriangles fabricated using NSL technique. (a) Shows the image of as-synthesized Ag nanotriangles. (b) Shows the image of laser treated Ag nanotriangles. An individual triangle break into 3-6 semispherical NPs. Images taken from Ref. [155].

Table 2.1 summarizes the materials details studied in various chapters.

Table 2.1: Details of material and morphology studied in the thesis.

Chapter No.	Materials	Film thickness	Morphology
3	Ag, Co	10 - 50 nm	Nanotriangles, semispherical NPs
4	Ag, Co	1 - 5 nm	Hemispherical NPs
5	Ag, Co	1 - 50 nm	Nanotriangles, Hemispherical NPs
7	Terfenol-D [ $(Tb_{0.3}Dy_{0.7})Fe_{1.92}$ ]	5 - 75 nm	Film

### 2.1.3 Characterization techniques

#### 2.1.3.1 Surface/morphology characterization

- Scanning electron microscopy (SEM):** After the nanostructure formation, they were characterized for their morphology using SEM. Zeiss Merlin SEM was used to image the morphology of the various mono-metallic and bi-metallic nanostructures being operated in the voltage range of 1.7 to 5 kV and using an inlens or secondary electron detector. The size of the nanoparticles and its size distribution was calculated using image processing software ImageJ.
- Atomic force microscopy (AFM):** Roughness measurements of the as-deposited films were made by atomic force microscopy (AFM). Areas of  $4 \times 4 \mu m^2$  were scanned for the various films and root mean square (rms) roughness was calculated by averaging over multiple (up to 256 number) line profiles at different areas. The film roughness measurements were done using Nanonics Multiview 1000 AFM, which was operated in line-by-line tapping mode at a resolution of 256-by-256 and a rate of 8 ms per point. The cantilever tip had a radius of curvature measuring less than 40 nm.

### 2.1.3.2 *Elemental identification*

- **Transmission electron microscopy:** The elemental mapping was done using Zeiss Libra 200. The elemental mapping of bimetallic nanostructures was done using either core-loss electron-energy loss spectroscopy or energy dispersive spectrometry (EDS). The TEM is equipped with Bruker XFlash 5030 to do the EDS mapping. High resolution TEM images and diffraction patterns were taken in a Zeiss Libra 200MC at an acceleration voltage of 200kV, while the Z-contrast images and EELS spectra were taken with an aberration corrected (Nion, Inc.) dedicated STEM VG 501 UX operated at 100kV. This instrument is equipped with a cold field emission electron source and a Gatan Enfina EELS spectrometer.
- **X-ray powder diffraction (XRD):** As-deposited and annealed thin films were characterized using grazing incidence X-ray diffraction (GIXRD). These measurements were performed using a Panalytical X'Pert3 MRD X-ray diffractometer equipped with Cu K $\alpha$  source (1.54059 Å) radiation and a Xe-proportional detector. The GIXRD patterns were recorded in a  $2\theta$  scanning mode using a parallel beam mirror on the incident beam side and a parallel plate collimator of 0.27 divergence on the diffracted beam side. A combination of beam mask and divergence slits was selected to illuminate the sample surface without illuminating the sample holder. In order to avoid diffraction from the sample holder the samples were mounted on a 2-inch single crystal silicon wafer oriented slightly off axis. The GIXRD patterns were collected in the  $2\theta$  range between 10-90° with a step size of 0.02° and step time of 7 sec/step.
- **X-ray photoelectron spectroscopy (XPS):** XPS measurements were carried out at room temperature by using a SPECS Focus 500 monochromated Al K $\alpha$  X-ray source operated at 380 W and a SPECS PHOIBOS-150 hemispherical electron analyzer at normal emission and 40 eV pass energy. Relative atomic concentrations were taken from comparison of Dy3d, Tb3d<sub>5/2</sub>, O1s, and Fe2p<sub>3/2</sub> core levels, analyzed and corrected for sensitivity and transmission factors in CasaXPS software.

### 2.1.3.3 *Physical properties*

- **Optical properties:** The optical characterization was done using HR2000+ES spectrometer which can record the reflection or transmission spectrums. For the present work, all the measurements were done in the transmission mode. Optical fibers of internal diameter of 600  $\mu\text{m}$  were used to shine the light on the samples. The optical data was acquired using the data acquisition card and was displayed using Ocean's optics software called the Spectra suite. The spectral coverage of this optical instrument is from UV to near infrared (200-1100 nm). It uses a light source consisting of deuterium source. Deuterium light source has characteristic peaks at 656 and 486 nm called  $D_\alpha$  and  $D_\beta$  peaks, respectively. It also has a characteristic band between 560-640 nm in its emission spectra called Fulcher- $\alpha$  band as shown in Fig. 2.6. To get good signal, it was made sure to avoid saturation of the reference spectrum at the characteristic peaks of the light source. However, due to the limitation of the instrument,  $D_\alpha$  peak saturation was unavoidable. The acquisition of the data was done at an

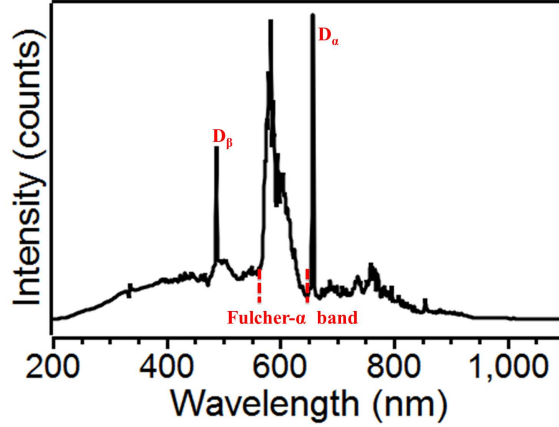


Figure 2.6: Deuterium light source spectra.

integration time of 1 ms for an average to scans ratio of 100 to get good signal to noise ratio. The final processed optical data is made saturation free by removing the  $D_\alpha$  peak.

For further analysis of the raw transmission data, absorption spectrums were generated by using Beer-Lambert's law using the formula:

$$Abs = \ln \left( \frac{100}{T\%} \right) \quad (2.1)$$

where,  $Abs$  is the absorption and  $T$  is the transmission. The obtained absorption spectrums were then normalized with respect to the highest intensity peak. Fig. 2.7 shows the transition of optical spectrums from raw i.e. the transmission data to the final state i.e. normalized absorption spectrums. From this normalized absorption spectrum, the full width half maxima was calculated which is known as the bandwidth (BW) of the plasmon peak. The BW's of the plasmon peaks were calculated by fitting multiple Lorentzian peaks in the experimental normalized absorption spectrums as shown in Fig. 2.7 (c). The localized surface plasmon resonance peak (LSPR) is the peak corresponding to the maximum intensity.

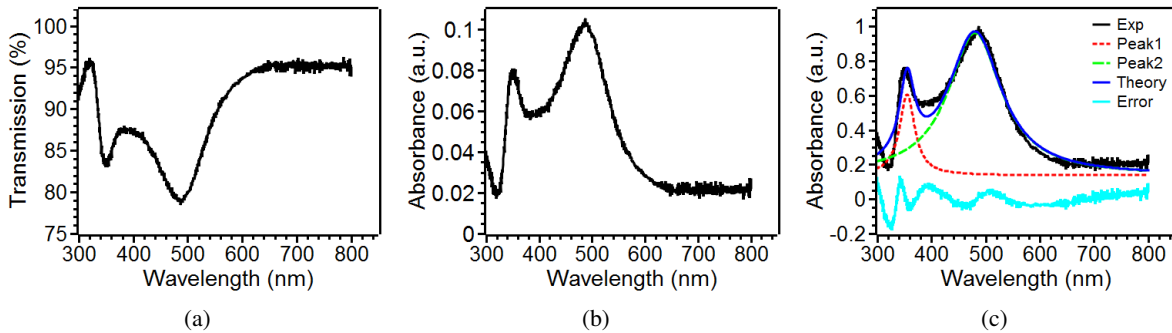


Figure 2.7: (a) The raw transmission data. (b) Absorption spectra converted from raw transmission data using Eq. 2.1. (c) Normalized absorption spectra fitted with two Lorentzian peaks.

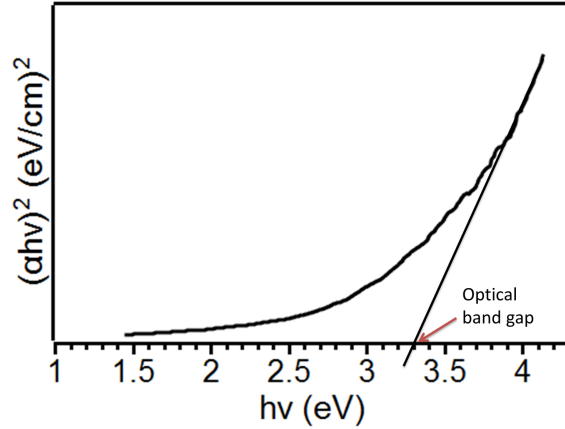


Figure 2.8: Tauc plot to find the optical band gap of semiconductor materials.

Tauc plots were generated for the amorphous semiconductor films made of the oxides of Fe-Tb-Dy ternary system. From the Tauc plots, the optical direct band gap was calculated by drawing the tangent at the onset of absorption increase due to interband transition. To obtain the Tauc plot, the absorption co-efficient ( $\alpha$ ) was calculated as:

$$\alpha = \frac{Abs}{t} \quad (2.2)$$

where,  $t$  is the film thickness in  $cm$ . After that,  $(\alpha hv)^2$  as a function of  $hv$  was plotted. This plot is known as Tauc plot. A typical example of calculating band gap from Tauc plot is shown in Fig. 2.8.

The optical studies were done by preparing different sets of Ag, Co-Ag and Fe-Ag samples on quartz substrate. The samples were characterized for their optical properties to study the role of particle size, shape and anodic material on the degradation of Ag bimetallic nanoparticles as a function of days. These spectrums were then used to generate absorption dependent wavelength plots. From these plots, various information was extracted, such as, plasmon peak position, the plasmon bandwidth and the plasmon quality factor. The peak position and bandwidth was plotted as a function of time to study the oxidation degradation behavior of the bimetallic nanoparticle. Semiconductor oxide films of Fe-Tb-Dy ternary alloy were deposited on quartz substrate for studying their optical behavior and for the calculation of the direct optical band gap.

- **Magnetic properties:** The magnetic properties of the as deposited and annealed films were studied using surface magneto-optical Kerr effect (SMOKE) technique. The SMOKE measurements were done in the longitudinal orientation using a s-polarized laser beam of 633 nm wavelength making  $12.6^\circ$  angle of incidence with the normal to the substrate plane. The schematic for the SMOKE measurement setup for the longitudinal geometry is shown in Fig. 2.9. The Terfenol-D thin film was also studied for its magnetic properties using SMOKE setup.

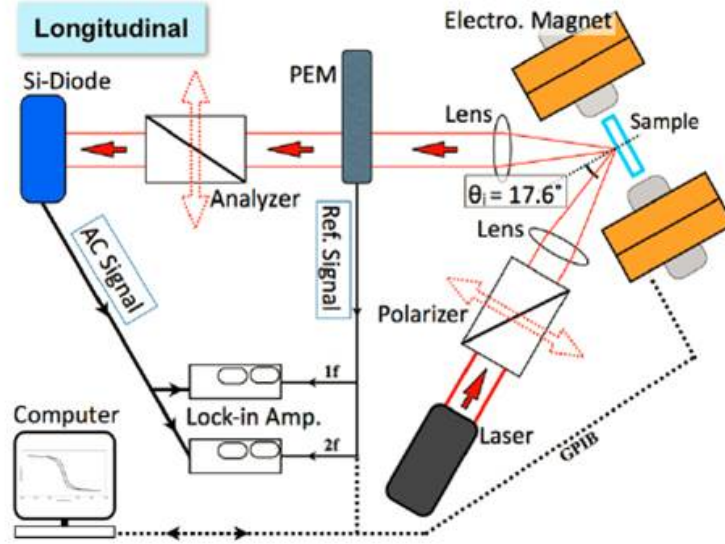


Figure 2.9: SMOKE setup for measurements to be done in longitudinal orientation [156].

- Electrical properties:** For measuring the electrical transport properties of thin films, silver pads were deposited on the four corners of the sample using e-beam evaporation, as described previously. Gold wires were then attached to the silver pads using silver epoxy paste. A Keithley 2400 sourcemeter was used to measure the sheet resistance and the hall mobility of the deposited amorphous oxide. Sheet resistance was measured using the van der Pauw method, where probe contacts are made at the four corners of the sample. Current was supplied at two adjacent contact points while voltage was measured at the two remaining contact points, i.e. if the four contacts were numbered 1, 2, 3, and 4, current was supplied between 1 and 2 ( $I_{12}$ ), while voltage was measured between 4 and 3 ( $V_{43}$ ) to get resistance  $R_{12,43}$ . In this way, the current direction was changed to cover all four sides, making sure to reverse the current direction on each side, resulting in eight total measurements. The four-probe resistance was measured by the Keithley sourcemeter working in 4-wire sensing mode. A LabVIEW code was written to collect data from the Keithley for 1 minute and then display the average value. This method of data collection ensured noise-compensated resistance values. After all the eight resistance values were measured ( $R_{12,43}$ ;  $R_{21,34}$ ;  $R_{34,21}$ ;  $R_{43,12}$ ;  $R_{41,32}$ ;  $R_{14,23}$ ;  $R_{23,14}$ ;  $R_{32,41}$ ), the following formula was used to calculate the sheet resistance:

$$\exp(-\pi R_A/R_S) + \exp(-\pi R_B/R_S) = 1 \quad (2.3)$$

where

$$R_A = (R_{12,43} + R_{21,34} + R_{34,21} + R_{43,12})/4 \quad (2.4)$$

and

$$R_B = (R_{41,32} + R_{14,23} + R_{23,14} + R_{32,41})/4 \quad (2.5)$$

and  $R_S$  is the sheet resistance. The resistivity was calculated as the product of the sheet resistance and the film thickness.

Hall measurements were made by applying current along the contacts 3 and 1, and measuring the voltage between 4 and 2. For each value of current, the magnetic field was varied and the corresponding hall voltages were measured. Just like for sheet resistance measurements, a LabVIEW program was used to collect data to compensate for noise and drift. A plot was then made of Hall voltage vs applied magnetic field and a straight line fit was applied to it to obtain the slope of the plot. The hall mobility,  $\mu$ , was then calculated using:

$$\mu = \left( \frac{dV}{dB} \right) \frac{1}{IR_S} \quad (2.6)$$

where,  $I$  is the current supplied and  $R_S$  is the sheet resistance. The process was repeated with at least three different current values to obtain reliable hall mobilities. The carrier concentration,  $n$ , was calculated as  $n = \frac{1}{e\mu\rho}$ , where  $e$  is the charge on an electron, and  $\rho$  is the resistivity.

Sheet resistance was also measured as a function of temperature using Keithley 2400 sourcemeter. Although the same 4-wire sensing mode was used as for sheet resistance measurement, the contacts for current supply and voltage measurement were fixed to one configuration so as to not disturb the system while the film was being heated with an IR lamp. The temperature was measured periodically using a laser temperature sensor and the corresponding resistance value was noted from the sourcemeter. Once the temperature reached about 450 K, the IR lamp was turned off and the film was allowed to cool down. Temperature and resistance values were obtained in the same manner during the cooling cycle as well.

## 2.2 Theory and modeling techniques

### 2.2.1 Oxide quantification:

The mean field approximation (MFA) model was used to quantify the Co oxidation in CoAg bimetallic nanoparticles. The oxide quantification was then used to theoretically calculate the lifetime of oxide free Ag in Co-Ag nanoparticles. The MFA uses the fraction of materials in a single nanoparticle (i.e. Co, CoO and Ag) to calculate the effective complex dielectric function of a single NP, which is then used to calculate the overall complex dielectric function of the array that is in contact with air and the substrate. By changing the amount of oxide, the best fit for the transmission signal of the array was generated. The effective complex dielectric function of a single nanoparticle was calculated using the binary mixing approach suggested in the ref. [157, 158, 159, 160]. To calculate the effective complex dielectric function of Co-Ag NPs, the binary mixing rule was employed twice, first to get the effective complex dielectric function of the Co-CoO

system and then, after incorporating the Ag dielectric, to get the overall effective complex dielectric function of the NP system. The effective complex dielectric function of Co-CoO-Ag NP system was then used to calculate the theoretical transmission signal of the bimetal NP system in contact with air and substrate using the equation mentioned in ref. [117, 161].

### **2.2.2 NSL simulation:**

The structures synthesized by ARNSL were simulated using the projection of shadows casted by PS beads when placed in the path of the material flux being deposited. The mathematical equation for the shadow is the equation of an ellipse. The area of the ellipse can be controlled by the angle of deposition which will affect the size of the triangular feature [74]. Orientation of the HCP patterns of PS beads also define the size of the patterns formed using NSL [74]. The two critical angles for pattern formation are:  $\phi$ , the angle of the HCP structure with respect to the fixed axis in the x-y plane and  $\theta$ , the angle made by the material deposition vector ( $\vec{p}$ ) with the z-axis. By controlling these two parameters a wide variety of structures with different interface areas can be formed.

### **2.2.3 Bridging Mie, Fresnel and Effective medium approximation theories:**

The idea behind this part of the work is to accurately predict the optical behavior of metal nanoparticle arrays embedded in a dielectric medium in a simple and time efficient way. Most of the theoretical models involve FDTD or DDA calculations which are more time and resource consuming and works for a single nanoparticle system [115]. So, there is a need for a model which can calculate the properties of a single metal NP as predicted by Mie or Rayleigh theory and incorporate it to calculate the optical spectrum from stacked dielectric layers. To achieve this, we have used the approximate Mie theory [125] to calculate the polarizability of the metal NP using Clausius-Mossetti equation. And is then bridged with Fresnel equation using effective medium approximation (EMA) to calculate the optical spectrum of metal nanoparticles embedded in dielectric layers. EMA works on the principle that the embedded NPs are non interacting with each other and the electric field inside them is uniform [162].

## **2.3 Acknowledgment**

All the TEM work was performed by Dr. Gerd Duscher and Jingxuan Ge. The XPS measurements were performed by Dr. Arthur Baddorf and the XRD by Dr. Maulik Patel.

## Chapter 3

# Two-dimensionally ordered plasmonic and magnetic nanostructures on transferable electron transparent substrates

(Reproduced with permission from Abhinav Malasi, Jingxuan Ge, Connor Carr, Hernando Garcia, Gerd Duscher and Ramki Kalyanaraman, *Part. Part. Syst. Charact.*, **2015**, 32, 970-978. Copyright 2015 WILEY-VCH Verlag GmbH & Co. KGaA)

### 3.1 Summary

Discovery of new plasmonic behaviors from nanostructured materials can be greatly accelerated by the ability to prepare and characterize their near field behaviors with high resolution in a rapid manner. Here we report an efficient and cost-effective way to make two-dimensionally (2D) periodic nanostructures on electron transparent substrates for rapid characterization by transmission electron microscopy. By combining nanosphere lithography with a substrate float-off technique, large areas of electron transparent periodic nanostructures can be achieved. For this study, we investigated the synthesis of plasmonic nanostructures of Ag, magnetic nanostructures of Co and bimetallic nanostructures of Ag-Co. Characterization of the materials by a combination of TEM, far field optical spectroscopy, and magnetization measurements revealed that this new approach can yield useful nanostructures on transparent, flexible and transferable substrates with desirable plasmonic and/or magnetic properties.

### 3.2 Method

The procedure yielding large area 2D periodic nanostructures on electron transparent carbon substrates involves three distinct steps (Fig. 3.1). Step 1 is the creation of the NSL mask and involves preparation of ultrathin carbon films on a rigid substrate followed by deposition of an array of close-packed polystyrene (PS) beads onto the substrate. The array of PS beads will serve as the deposition mask for the next step.



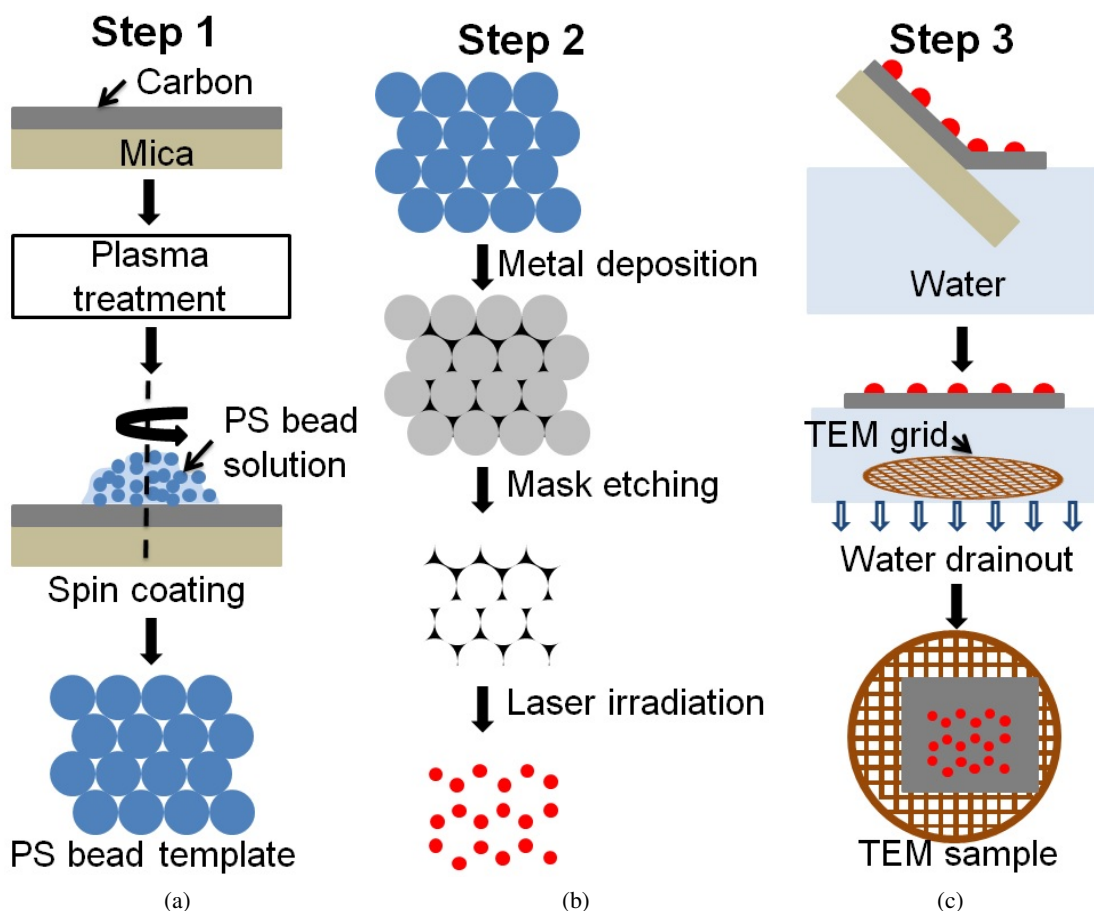


Figure 3.1: The schematic shows the three major steps for the TEM sample preparation. (a) Step 1 of the synthesis, which is focused on NSL template formation. It shows the formation of NSL template on plasma treated carbon film on mica substrates. (b) Step 2 is fabrication of nanostructures, which is achieved by depositing metal films and then etching out the template. Further heat treatment, such as with laser pulses, can be done to the metal nanostructures to change their shape. (c) Step 3 is the float off of the carbon substrate with NSL structures on the water surface which is then captured on the TEM grid by draining the water.

Step 2 is the fabrication of nanostructures of the desired material and involves thin film deposition, etching of the PS spheres, and, if needed, a thermal processing step to transform the nanostructures. The final step, step 3, is the creation of the TEM sample and involves float-off to make the electron transparent material, which is captured directly onto a TEM grid for subsequent analysis. The specific details of the various steps involved are described next.

*Step 1 - Creation of NSL mask [Fig. 3.1(a)]:* The initial substrate for use in the PS deposition was made by depositing carbon onto V-2 grade mica sheets purchased from Electron Microscopy Sciences Inc. Thin films of carbon were deposited on a freshly exposed surface of mica following removal of its top layers with the help of scotch tape. An amorphous carbon (a-C) of thickness in the range of 5 to 25 nm was sputter deposited using a SPI Inc. carbon coater under a vacuum of  $10^{-4}$  Torr with a deposition rate of 5 nm/min [153]. After the deposition, the a-C films were treated in an oxygen plasma to make the top surface of

carbon hydrophilic. The plasma treatment was done for 10 sec using a Technics Inc. instrument operating at 8 V and a current of 10 mA. These plasma treated carbon substrates could retain their hydrophilicity for almost 24 hours. Following the plasma treatment, the carbon substrates were ready for the formation of a monolayer or bilayer of close packed PS beads. PS beads of size 500 nm in diameter were received as 2% w/v suspension in water from Alfa Aesar. NSL masks were then created by spin coating the solution of PS beads diluted with the mixture of Triton-X and methanol (1:400 volume ratio) in 1:1 volume ratio to achieve the hexagonal closed pack (HCP) arrangement of the beads [47]. The role of the surfactant, Triton-X, was to make the substrate wettable for the uniform spreading of the PS beads. To achieve the HCP arrangement, PS bead solution was spin coated at three different speeds using a programmable spin coater from Laurell Technologies Corporation model number WS-400BZ-8TFM/LITE. The three step coating consisted of spin coating at 400 rpm for 10 sec to spread the PS beads uniformly, then at 800 rpm for 2 minutes to remove the excess material, and finally at 1400 rpm for 10 sec to remove the bead accumulation occurring at the edges [152]. After this, the sample was left to dry under controlled environment (temperature maintained at  $22 \pm 1$  with relative humidity at  $40 \pm 5\%$ ). Apart from the carbon substrate, the PS beads were also deposited onto glass, quartz and 400 nm  $SiO_2$  coated Si substrates.

*Step 2 - Fabrication of nanostructures [Fig. 3.1(b)]:* Once the mask was dried, the substrates were ready for the deposition of metal film onto them. Metal films of Ag and Co were deposited inside a vacuum chamber operating at a base pressure of  $2 \times 10^{-8}$  Torr to achieve monometal or bimetal systems. The Ag metal films were deposited using a Mantis QUAD-EV-HP e-beam evaporator while the Co films were deposited using Tectra e-beam evaporator. Metal targets of 99.999% purity from Alfa Aesar Inc. were used. Ag films in the thickness range of 5 to 40 nm were deposited, while Co films were deposited in the range of 2 to 10 nm. The deposition angle of the target metal could be controlled by rotating the sample holder. The deposition of the metals were done at  $0^\circ$  and  $\pm 10^\circ$  with respect to the normal to the plane of substrate. Different samples of Co-Ag were made by depositing them at various angles mentioned. After the deposition of metal films, the PS mask was etched out by dipping the NSL substrates in dichloromethane. Depending on the thickness of the metal film, the etching time varied from few seconds to around 2 minutes. Once the PS beads were etched out, the carbon substrates with NSL or ARNSL were ready to be transferred on to the TEM grid. The deposited metal films on the carbon substrate were in the shape of triangles [47, 48]. We also tested whether the shape could be changed by a thermal treatment of the nanostructures on the C/mica substrate. The Ag triangles made from 5 nm thick film were irradiated using nanosecond laser pulses to form semi-spherical nanoparticles. The Ag samples were irradiated using a 9 ns pulsed width Nd:YAG laser from Spectra Physics, which is a injection seeded Lab-130-50 laser operating at 266 nm wavelength with a repetition rate of 50 Hz. The Ag metal triangles were irradiated at normal incidence in ambient air environment using an energy density of  $90 \text{ mJ/cm}^2$  for 10,000 pulses with a beam size of  $1 \text{ mm}^2$ .

*Step 3 - Creation of TEM sample [Fig. 3.1(c)]:* The periodic arrays fabricated by NSL and ARNSL on carbon substrates were then floated off onto the surface of distilled water. Due to the hydrophobic nature of carbon and the weak forces of adhesion between the carbon and the mica surface, the surface tension of water was able to debond carbon from the mica surface resulting in an electron transparent C + nanostructure substrate. This substrate was directly captured onto a lacey carbon TEM grid by slowly draining of the water

as detailed in ref. [153].

### 3.3 Characterization

The morphology of the NSL samples prepared on glass, quartz or 400 nm  $SiO_2$  coated Si substrates were characterized using a Zeiss Merlin SEM operated at 1.7 kV. The synthesized NSL samples of Ag and Co were also characterized for their optical and magnetic properties. The far-field optical properties were studied in transmission mode using a HR2000+ES spectrometer from Ocean Optics on glass and quartz substrates. The transmission spectrum was then converted to absorption spectrum using Beer-Lambert's law. The magnetic study of the NSL samples was done using an in-house developed surface magneto-optical Kerr effect (SMOKE) system [163, 156]. The SMOKE measurements were done in the longitudinal orientation using an s-polarized laser beam of 635 nm wavelength. The angle of incidence for the laser beam with the normal to the substrate plane was  $12.6^\circ$ . A Zeiss Libra 200 TEM was used to characterize the NSL samples on the carbon substrates by high angle annular dark field (HAADF) mode and electron energy-loss spectroscopy (EELS) at 200 kV. The TEM was equipped with a monochromator and omega shaped energy filter. The semi-convergent and semi collection angles were 9 and 11.9 mrad, respectively. The spatial and energy resolution of the monochromator equipped TEM in STEM mode was 0.3 nm and 0.15 eV, respectively. The low loss EELS was performed using a slit of  $0.5 \mu m$  monochromator slit with a energy dispersion of 0.025 eV/channel for a exposure time of 0.1 sec. Similarly, core loss EELS analysis was performed by using a  $60 \mu m$  monochromator slit with a energy dispersion of 0.1 eV/channel for a exposure of 1 sec. The incident electron beam current recorded for low loss and core loss EELS measurements was 1.577 and 131.58 pA, respectively. Bruker XFlash 5030 energy dispersive spectrometer (EDS) was used to gather the elemental information of the metals in the Zeiss Libra 200.

It is to be noted that the color contrast of the TEM and SEM images have been inverted for visual clarity. Since the imaging in the TEM was done in HAADF mode, so, the Z-contrast that is evident in HAADF imaging will be inverted, i.e. higher atomic number metals will appear darker in contrast in comparison to lower atomic number metals.

### 3.4 Results and discussion

First, the application of NSL + FO leading to electron transparent nanostructures is presented for a prototypical plasmonic metal, Ag. Fig. 3.2(a) shows an SEM image of typical Ag nanotriangles formed by the NSL technique using normal incidence deposition of 5 nm thick Ag film onto quartz substrates. The inset of this image is a computer generated diffraction pattern from Fast Fourier Transform (FFT) analysis of the image contrast. The hexagonal symmetry was clearly evident. Fig. 3.2(b) shows a magnified image to clearly show the repeating hexagonal unit for the Ag nanotriangles. Fig. 3.2(c) shows the Ag nanoparticles formed after irradiating the Ag nanotriangles of Fig. 3.2(a) using laser pulses. Fig. 3.2(d), which is a magnified image of (c), shows that each Ag triangle dewets into a collection of nanoparticles but retains the overall hexagonal symmetry. Fig. 3.2(e) shows the TEM HAADF image of the nanotriangles formed on C substrate following

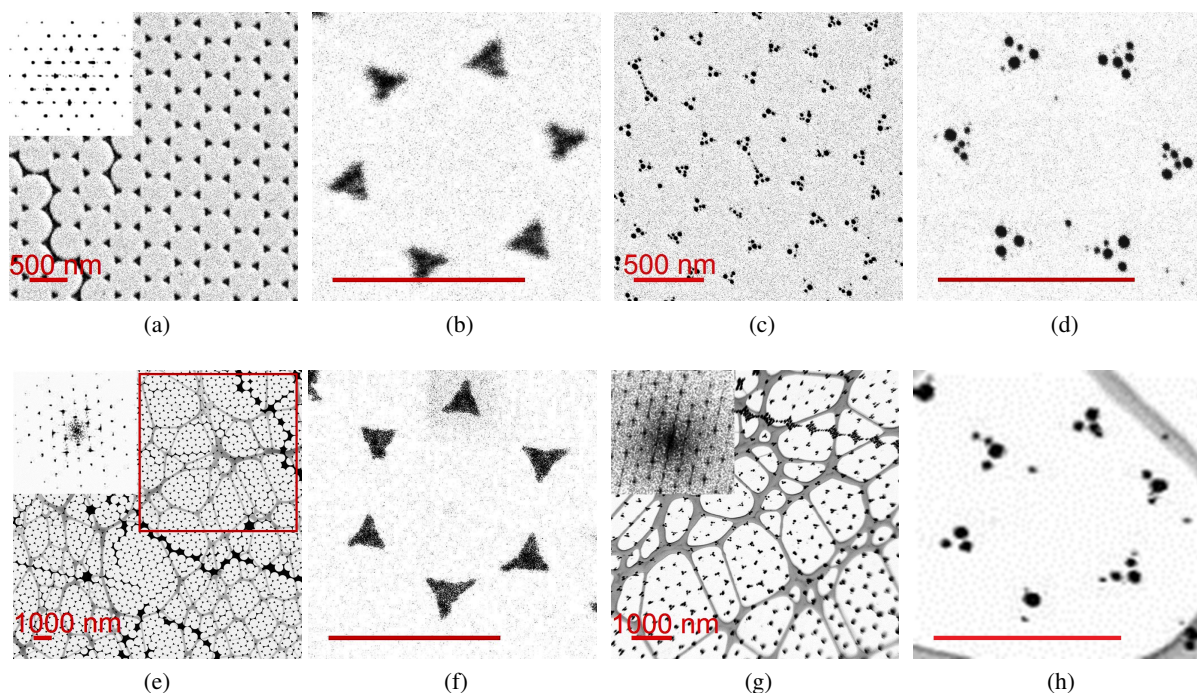


Figure 3.2: (a) SEM images of Ag nanotriangles formed by NSL on quartz substrate. Inset shows the FFT of the contrast in (a) providing clear evidence for the hexagonal symmetry. (b) Magnified image of the repeating Ag nanotriangle hexagonal pattern. (c) SEM image of Ag nanoparticles formed by irradiation of Ag nanotriangles on quartz using pulsed laser heating. (d) Magnified image of the irradiated Ag nanotriangles. (e) TEM HAADF image of the Ag nanotriangles formed by NSL + FO. The underlying lacey carbon film of the TEM substrate is also evident. Inset shows the FFT (taken from the the red square) showing evidence for the hexagonal symmetry of the spatial arrangement. (f) Magnified TEM image of the Ag nanotriangle repeating unit. (g) TEM HAADF image of the Ag nanoparticles transformed from nanotriangles following irradiation by laser pulses formed by NSL + FO. Inset FFT shows the hexagonal symmetry. (h) The magnified image of the irradiated Ag nanotriangle patterns. The scale bar on the individual hexagonal ring images is 500 nm.

the same NSL conditions as in Fig. 3.2(a). The overall pattern morphology and symmetry is similar to that observed in the SEM image [Fig. 3.2(a)]. An area of  $15 \times 15 \mu\text{m}^2$  is covered by an array of nanotriangles arranged in hexagonal symmetry, as confirmed by the FFT shown in the inset of Fig. 3.2(e). This FFT was taken from the marked location of the image. Fig. 3.2(f), which is a magnified HAADF image of (e), was used to calculate the spacing and triangle size. The length of the angle bisector of the largest equilateral triangle than can fit was 115 nm while the spacing between the adjacent triangles was 290 nm. These values were consistent with the size and spacing expected for close packed arrangement of 500 nm sized beads [47]. Fig. 3.2(g) shows the TEM HAADF image of Ag particles formed from the triangles after pulsed laser irradiation of the nanotriangles on C/mica substrate. While there is no change in the hexagonal arrangement of the triangles, as evidenced by the inset FFT, each nanotriangle transformed into a collection of 3 to 6 semi-spherical Ag nanoparticles, similar to that seen by the SEM in Fig. 3.2(d). From these results it was clear that NSL + FO can lead to nanostructures similar to conventional NSL on rigid substrates and that the patterns could be thermally treated on the C substrates in order to further transform them.

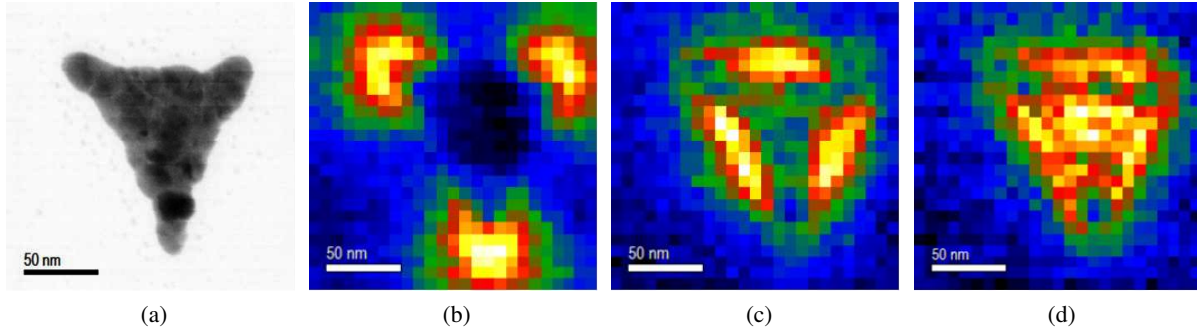


Figure 3.3: *Low loss EELS mapping of a Ag nanotriangle on C substrate. (a) HAADF image of Ag nanotriangle. (b-d) Map of different plasmon modes excited by the e-beam. (b) corresponds to an energy of 1.35 eV, (c) is for 2.5 eV and (d) is 3.2 eV.*

Another motivation for this work was to show that high-quality electron transparent materials can be readily obtained and so we performed a low loss EELS study to characterize the plasmonic behavior of the Ag nanotriangles. Fig. 3.3 shows the low loss EELS study of a single Ag nanotriangle of thickness 10 nm deposited at  $10^\circ$ . Fig. 3.3(a), shows the HAADF image of a single Ag nanotriangle of side lengths 110, 135 and 145 nm, while Fig. 3.3(b-d) shows the EELS map of plasmon excitations at different energies:  $1.35 \pm 0.2$ ,  $2.5 \pm 0.2$  and  $3.2 \pm 0.2$  eV, respectively, excited by the electron beam. The lightest (yellow) region represents the maximum plasmon scattering intensity while the dark (blue) regions represent the minimum scattering. This low loss EELS mapping of the Ag triangle on carbon substrate confirmed that the NSL + FO Ag samples also show various excitable plasmon modes on the Ag nanotriangles, as confirmed by previous TEM studies [44].

Besides the potential applications that utilize the near field properties of plasmons, such as in plasmon resonance sensing, the far field optical and/or magnetic behavior of nanostructures are also important. In addition, in the future, this ability to fabricate large area ordered arrays on which both near field TEM and far field studies can be done simultaneously or sequentially (but on the same regions of the sample), to yield correlated properties from complementary techniques could be tremendously powerful in our quest for new nanomaterials. Here, we performed far field studies of the optical and magnetic properties of the various triangles made on quartz substrates. In Fig. 3.4(a) the far field optical absorbance measured for light incident normal to the substrate plane is compared for Ag nanotriangles formed from different film thickness. As the film thickness increased, the strong absorption peak corresponding to a localized surface plasmon resonance (LSPR) was found to blue-shift, consistent with the earlier studies of Jensen et al and Chan et al [67, 164], who attributed it to a pyramidal-shape effect. The far field LSPR behavior for Ag semi-spherical nanoparticles formed by laser irradiation of 5 nm thick Ag nanotriangles (whose LSPR is not shown here since it is at a wavelength beyond 1000 nm) is shown by the dashed blue line. The LSPR of the Ag nanoparticles is substantially blue shifted as compared to the nanotriangles it was made from, which is consistent with the shape effect discussed previously [67]. Fig. 3.4(b) shows the SEM morphology of Co nanotriangles formed by NSL by deposition of 10 nm thick film at  $10^\circ$ . The inset again depicts the hexagonal symmetry. Fig. 3.4(c), compares the optical absorption spectrum of Co (10 nm) and Ag (29 nm) samples

deposited at  $10^\circ$ . Unlike Ag, pure Co does not show a strong plasmonic signal in the visible wavelength (Fig. 3.4(c), black line), consistent with our recent results on Ag and Co nanoparticles [17]. However, since Co is ferromagnetic, it shows strong magneto-optical character, which can be used to measure its magnetic hysteresis. This measurement is shown in Fig. 3.4(d), which compares the hysteresis of a continuous Co film (solid black line) with the NSL Co nanotriangles (dotted red line).

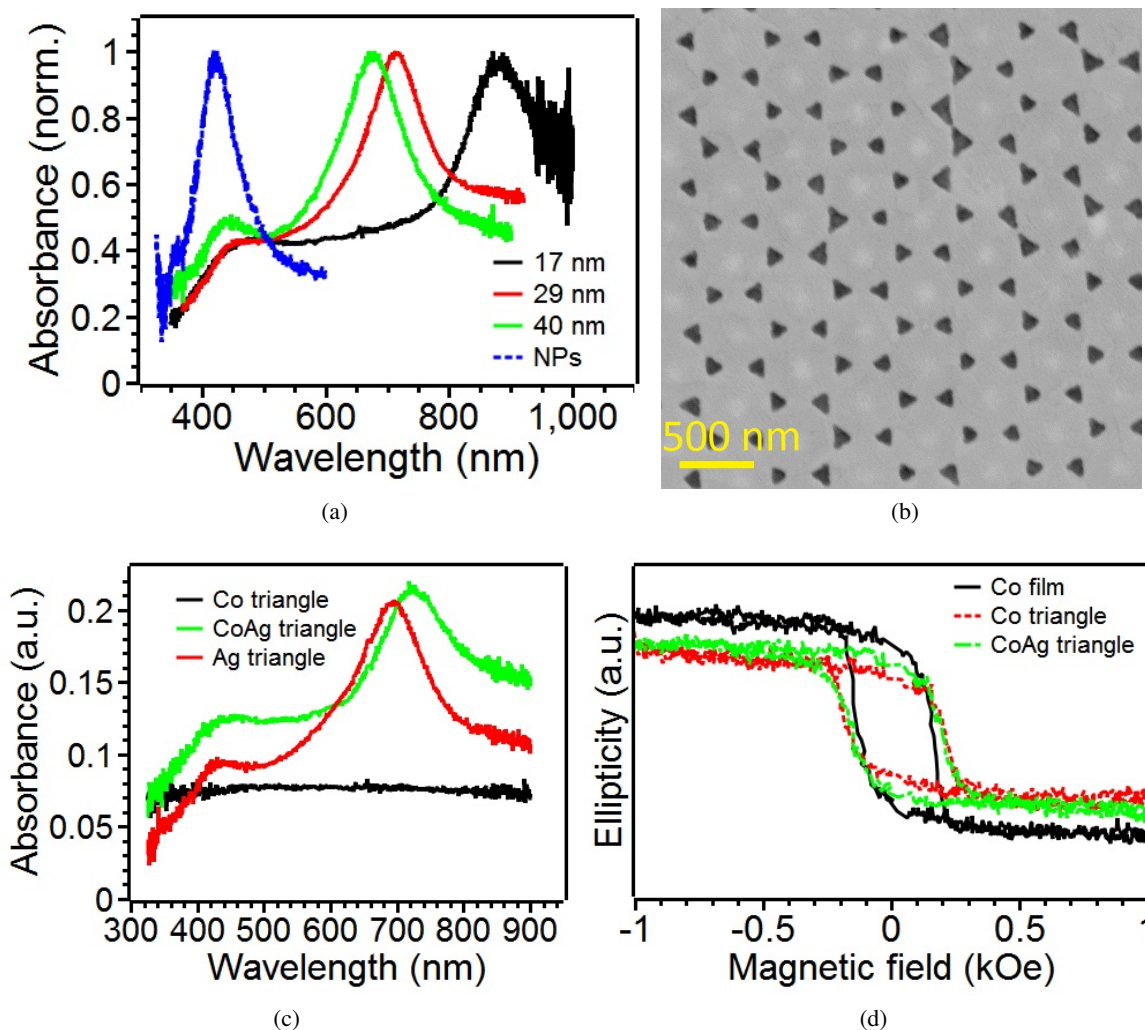


Figure 3.4: (a) Far-field optical absorption spectrum of Ag nanotriangles for various thickness of the triangular nanostructures. Also shown is the absorption spectrum for the Ag nanoparticles formed by pulsed laser heating (dashed blue line). (b) SEM morphology of Co nanotriangles from NSL on quartz, with inset showing the FFT hexagonal pattern. (c) Comparison of the far field optical absorption spectrum from Co, Ag and Co-Ag nanotriangles deposited at  $10^\circ$ , respectively. (d) Magnetic hysteresis measured by SMOKE technique in longitudinal geometry comparing a Co film (solid black line), NSL Co nanotriangles (dotted red line) and NSL Co-Ag triangles (dashed green line). The Co triangles were deposited at  $10^\circ$  and Co-Ag was deposited at  $10^\circ$  and  $-10^\circ$ , respectively.

Given the growing number of plasmonic discoveries related to the use of multi-component materials and interest in applications pertaining to strong magneto-optical behavior from bimetallic materials

[35, 165, 166, 167, 168, 169, 17, 7], we investigated the possibility to control the synthesis of bimetal nanostructures on quartz and the electron transparent C substrates using the NSL technique. As has been shown in ref. [69], ARNSL can yield a variety of geometries of nanostructures made from multiple different materials. Here, we extended this technique to directly making electron transparent substrates, something not demonstrated earlier. We compared the ARNSL model prediction for simple Co-Ag nanotriangle structures and characterized them using TEM and SMOKE techniques, as discussed next.

The capability of making various nanostructures using ARNSL is achieved by using the projection of shadows casted by beads in the path of the material flux being deposited. Mathematically, the shadows can be modelled by simply taking the projection of the bead when obstructed by a light source, which is elliptical in shape. With respect to Fig. 3.5(a), The elliptical shadow of the PS bead can be described as  $y = \frac{R \sin \theta \pm \sqrt{R^2 - x^2}}{\cos \theta}$ , where R is the radius of PS bead and  $\theta$  is the projection angle of material being deposited [74]. The pattern formation for ARNSL depends on the orientation of the HCP structures formed by PS beads with respect to the line of sight of deposition [74]. The difference in the patterns depend on the two different angles as shown in the schematic in Fig. 3.5(a). The angle  $\phi$  tells the orientation of the HCP structure with respect to the fixed axis in the x-y plane and  $\theta$  is the angle made by the material deposition vector ( $\vec{p}$ ) with the z-axis. By controlling these angles a wide variety of structures can be formed as can be seen in Fig. 3.5. Some of these structures have been simulated to show how the variation in the structures can be made using ARNSL. Fig. 3.5(b) shows a single metal deposited at  $\theta = 0^\circ$  and  $\phi = 0^\circ$ . Fig. 3.5(c) and (d) shows the theoretical structure for deposition of bimetals (shown by red and blue color) at  $\theta = \pm 10^\circ$  and  $\phi = 0^\circ$  and  $90^\circ$ , respectively. In Fig. 3.5(e) and (f), the experimental SEM image for bimetal Ag and Co deposition under the conditions of (c) is shown, with (f) being the magnified image of a repeating hexagonal unit. The difference in contrast for the two metals is due to their different atomic (Z) numbers. The comparison shows that each hexagonal ring is made of pairs of metal triangles arranged in a similar fashion for the simulated and experimental cases. Similarly, Fig. 3.5(g) and (h) corresponds to the experimental structure for Ag and Co generated with the conditions for the image shown in (d). Fig. 3.5(h) is a magnified image showing the repeat unit for the SEM image shown in (g). Similarity in arrangement of the pairs of triangles with the theoretical prediction is evident.

Next, the synthesis of bimetal Co-Ag triangles on the electron transparent substrates were also tested. Fig. 3.6(a) shows the TEM HAADF image of the overlapping triangles formed by deposition of the individual metals onto C at  $10^\circ$  and  $-10^\circ$  respectively, with respect to the normal to the substrate plane. The deposited films of Ag and Co were 10 nm each in thickness. The color contrast in the HAADF images comes from the difference in the Z-number of the two elements (inverted as mentioned earlier under the characterization section). The darker triangles correspond to Ag and the lighter ones to Co. In Fig. 3.6(b), a magnified HAADF image of one pair of triangles [marked by the red circle in Fig. 3.6(a)] is shown. This triangle pair was mapped for its elemental distribution using core loss EELS. Fig. 3.6(c) and (d) show the core loss EELS elemental mapping of Ag and Co metal respectively. Fig. 3.6(c) was generated using the Ag-M4,5 ionization edge at 367 eV. The map also represented the thickness profile of Ag using core loss EELS analysis. Similarly, the thickness profile of the Co region is shown in Fig. 3.6(d), and was generated using the Co-L2,3 ionization edge at 779 eV. The optical and magnetic behavior of this Co-Ag is shown in

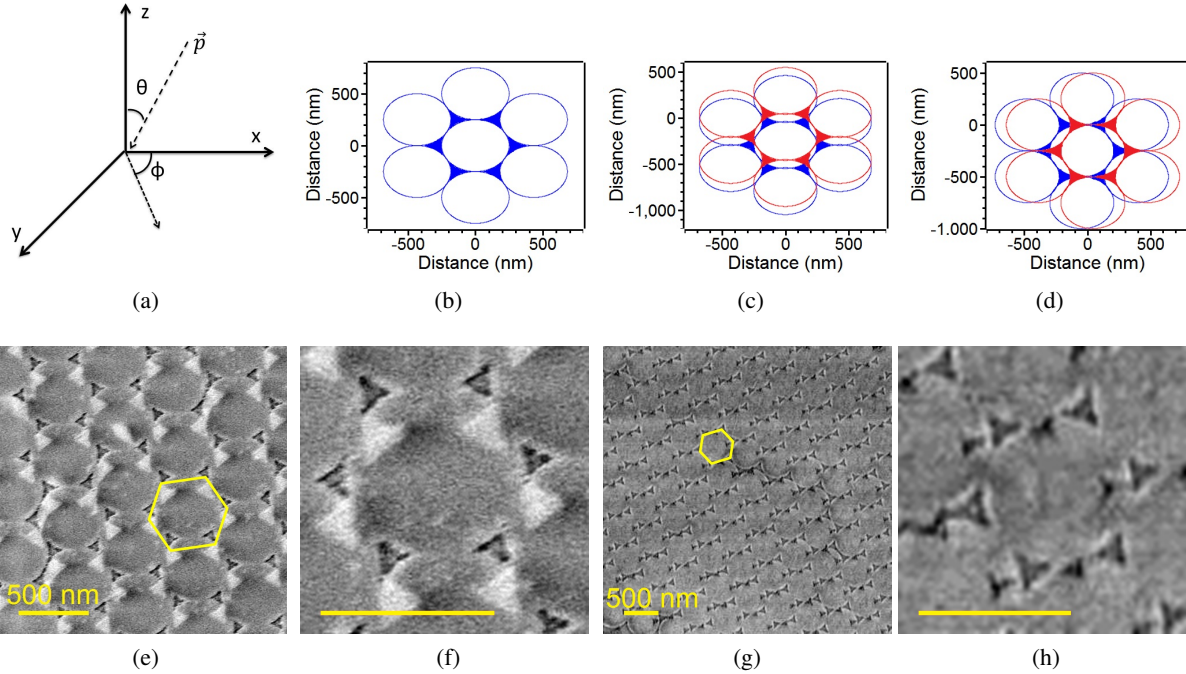


Figure 3.5: (a) The co-ordinate system for the modeling of ARNSL.  $x$ - $y$  is the plane of the substrate with  $z$ -axis acting as the normal to the plane.  $\vec{p}$  is the vector denoting the direction of the metal flux and makes an angle  $\theta$  with the  $z$ -axis.  $\phi$  is the orientation of the HCP with respect to the co-ordinate system. Some of the simulated patterns are shown in: (b) Simulated pattern for a single metal deposition with  $\theta = 0^\circ$  and  $\phi = 0^\circ$ . (c) Simulated pattern of bi-metals deposited at  $\theta = \pm 10^\circ$ ,  $\phi = 0^\circ$ . (d) Simulated pattern for  $\theta = \pm 10^\circ$ ,  $\phi = 90^\circ$ . (e) Experimental SEM image of Ag (bright triangles) and Co (dark triangles) deposited for the conditions in (c). (f) SEM image of repeating hexagonal pattern shown in (e). (g) Experimental SEM image of Ag (bright triangles) and Co (dark triangles) deposited for the conditions in (d). (h) SEM image of the repeating unit shown in (g). A hexagon is marked in the SEM images for reference and to show the repeating units of NSL. The length of the scale bars in (f) and (h) are of 500 nm each.

Fig. 3.4(c) and (d) respectively. The overlap of the Co with Ag shifts the Ag LSPR to red wavelengths, an effect previously reported for bimetallic nanoparticles of Ag-Co [15]. The hysteresis measured by SMOKE, and shown in Fig. 3.4(d, dashed green line) confirmed the ferromagnetic character of the Co triangles in contact with Ag. It should be noted that our SMOKE measurements were made with a 633 nm laser, far from the LSPR peak location of  $\sim 750$  nm seen for this bimetal triangle system in Fig. 3.4(c). Therefore, the enhanced magneto-optical signal that is expected around the LSPR resonance was not detected in our measurements [170]. A different set of Co-Ag triangles on the electron transparent carbon substrate was also investigated by elemental mapping using the EDS technique in the TEM. The hexagonal arrangement of the triangle can be seen in the HAADF image shown in Fig. 3.7(a). The Co and Ag were deposited at  $10^\circ$  and  $-10^\circ$ , respectively. Fig. 3.7(b) and (c) show the EDS maps of Co (blue) and Ag (red) metals, respectively. From these results we concluded that predictable electron transparent samples containing multiple different materials can be prepared by the NSL + FO technique.

*In this chapter we devised a carbon float-off technique to synthesize large 2D arrays of nanostructures*



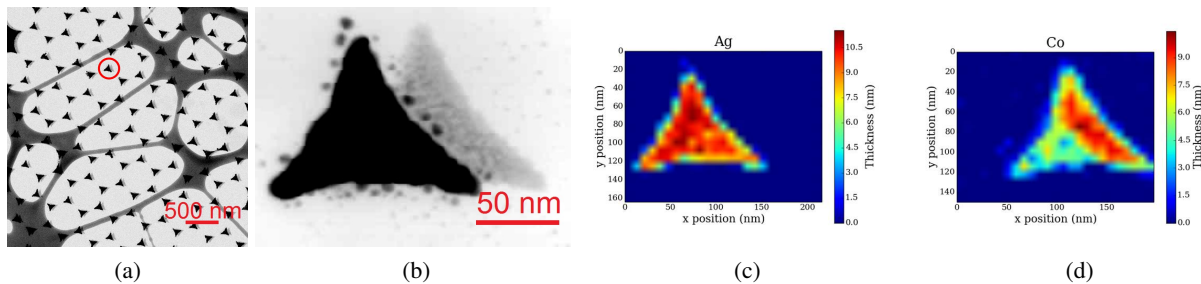


Figure 3.6: (a) The HAADF image of Co-Ag nanotriangles formed by deposition at  $10^\circ$  and  $-10^\circ$ , respectively. (b) A magnified HAADF image of one pair of Co-Ag nanotriangles, encircled in (a). (c) Core loss EELS map yielding the thickness of Ag in the structure shown in (b). Core loss EELS map yielding the thickness of Co for the structure shown in (b).

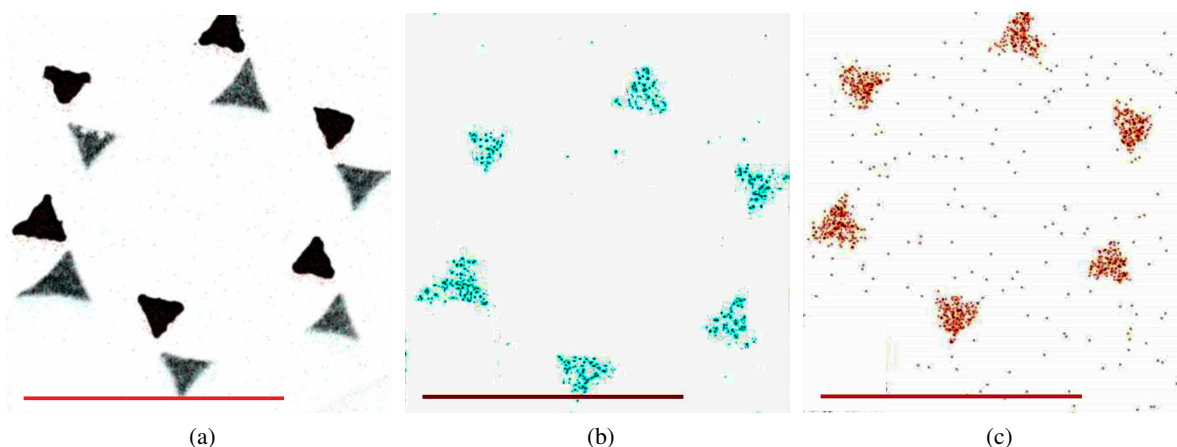


Figure 3.7: Elemental mapping of Ag and Co using EDS in the TEM. (a) HAADF image of Co (dark) and Ag (bright) triangles. (b) EDS map of Co across the HAADF image shown in (a). (c) EDS map of Ag across the HAADF image shown in (a). The scale bar is of 500 nm length.

on electron transparent substrates for TEM studies.

### 3.5 Acknowledgment

The authors acknowledge support by the Army Research Office through grant W911NF-13-1-0428. A portion of this research was conducted under grant CNMS2013-284 at the Center for Nanophase Materials Science, which is sponsored at ORNL by the Scientific User Facilities Division, Office of Basic Energy Sciences, U.S. Department of Energy. The authors would also like to acknowledge the use of TEM facilities housed by Joint Institute of Advanced Materials (JIAM) at University of Tennessee Knoxville. All the TEM related data was obtained by Jingxuan Ge and the carbon substrates were prepared by Connor Carr.

## Chapter 4

# Localized surface plasmon sensing based investigation of nanoscale metal oxidation kinetics

(Reproduced with permission from Abhinav Malasi, Ritesh Sachan, Vanessa Ramos, Hernando Garcia, Gerd Duscher and Ramki Kalyanaraman, *Nanotechnology*, **2015**, 26, 205701. Copyright 2015 IOP Publishing)

### 4.1 Summary

The localized surface plasmon resonance (LSPR) of nanoparticles can be a powerful and sensitive probe of chemical changes in nanoscale volumes. Here we have used the LSPR of silver (Ag) to study the oxidation kinetics of nanoscopic volumes of cobalt (Co) metal. Bimetal nanoparticles of the immiscible Co-Ag system prepared by pulsed laser dewetting were aged in ambient air and the resulting changes to the LSPR signal and bandwidth were used to probe the oxidation kinetics. Co was found to preferentially oxidize first. This resulted in a significant enhancement by a factor of 8 or more in the lifetime of stable Ag plasmons over that of pure Ag. Theoretical modeling based on optical mean field approximation was able to predict the oxidation lifetimes and could help design stable Ag-based plasmonic nanoparticles for sensing applications.

### 4.2 Experimental details

The bimetal nanoparticles (NPs) of Co-Ag were synthesized by a laser self-organization process detailed in previous publications [154, 15, 16, 17, 153]. This system was chosen because Co and Ag are immiscible metals, allowing for formation of nanoparticles with segregated regions of Ag and Co. These bimetal NPs were synthesized on quartz substrates. The substrates were cleaned by sonicating in acetone, isopropanol and deionized water for 20 min each and then dried with  $N_2$  gas and stored in closed containers prior to thin film deposition. The individual metal films of Co and Ag were sequentially deposited onto the optically smooth quartz substrates using e-beam evaporation in high vacuum ( $10^{-8}$  Torr). In the work reported here,

we prepared Co-Ag nanoparticles with two different volume percentages: one containing 16.7 vol% and the other containing 28.5 vol% of Co. This was done by preparing bilayer films with Ag ( $5 \pm 0.5$  nm) deposited on Co ( $1 \pm 0.15$  nm) and Co ( $2 \pm 0.3$  nm) deposited on Ag ( $5 \pm 0.5$  nm), respectively. The thickness and roughness of the deposited metal films were measured by a Nanonics Multiview 1000 atomic force microscope (AFM) working in contact mode. Following deposition, the bilayer metal films were irradiated in ambient air using a Spectra Physics injection seeded Lab-130-50 Nd:YAG laser with wavelength of 266 nm, a pulse width of 9 ns and repetition rate of 50 Hz. The laser irradiation was performed by scanning the laser ( $\sim 2$  mm/min) on the metal film using an energy density of  $100 \text{ mJ/cm}^2$  for 10,000 pulses over an area of  $\sim 1 \text{ mm}^2$  at normal incidence and in ambient air conditions. These Co-Ag samples were aged by storing in a closed container at room temperature (maintained at  $22 \pm 1^\circ\text{C}$  with a relative humidity of  $40 \pm 5\%$ ) for times ranging up to  $\sim 500$  days. The optical properties of the samples were measured in transmission mode using the HR2000+ES spectrometer from Ocean Optics. For the optical analysis to be presented, the transmission spectrum was converted to the absorption spectrum using Beer-Lambert law [171]. The imaging of the NPs was done using a Zeiss Merlin scanning electron microscope (SEM) operated at 5 kV with imaging by a secondary electron detector.

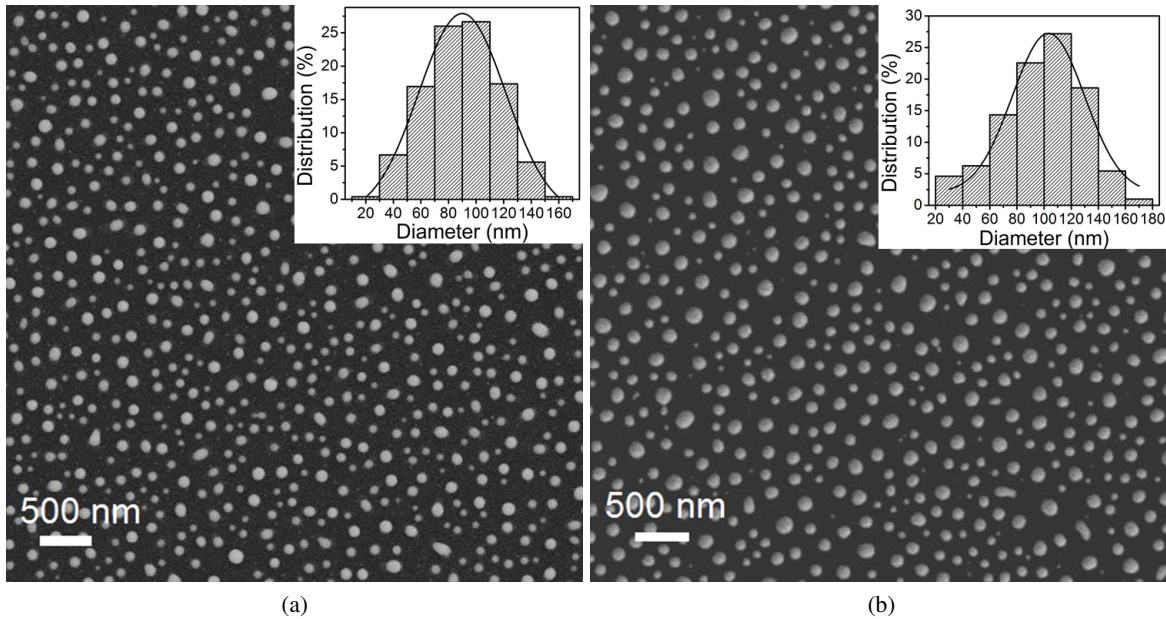


Figure 4.1: SEM images of Co-Ag NP arrays with the particle size distribution shown in the inset. (a) NP made from the Ag(5 nm)/Co(1 nm) case yielding particles of 16.7% Co with an average particle diameter of 91 nm and (b) NP made from the Co(2 nm)/Ag(5 nm) case yielding particles of 28.5% Co with an average particle diameter of 100 nm.

### 4.3 Results and discussion

Fig. 4.1 shows the SEM image of the freshly prepared nanoparticle array following pulsed laser irradiation of the bimetal films. Fig. 4.1(a) corresponds to the case of Ag(5 nm)/Co(1 nm) producing particles with

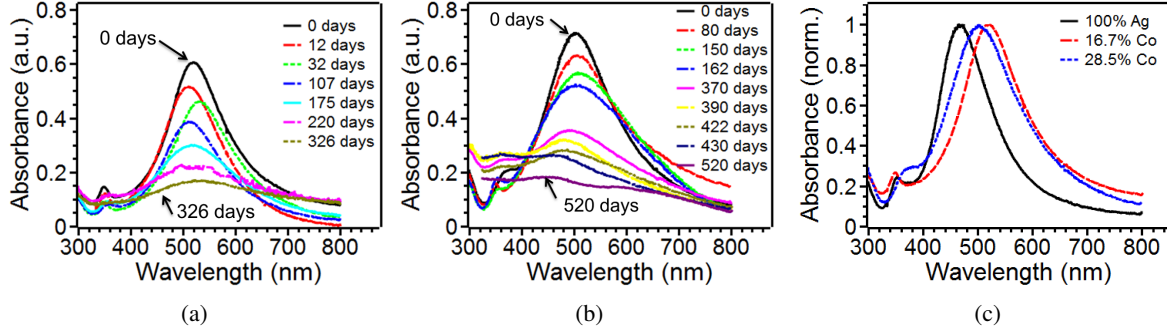


Figure 4.2: *Broadband optical absorption spectra recorded as a function of aging time for the two Co-Ag arrays. (a) Measured spectra for the 16.7% Co array and (b) spectra for the 28.5% case. The strong peak (such as the one at 520 nm for the 0 day 16.7% sample) is the LSPR peak. This peak decays with increasing aging time for both samples. (c) Comparison of the normalized optical absorption spectrums of freshly prepared Ag with 16.7 and 28.5% Co samples.*

16.7% Co, while Fig. 4.1(b) corresponds to the Co(2 nm)/Ag(5 nm) case yielding particles with 28.5% Co. In a previous publication we had detailed that the average ratio of the metal within each particle in the array was similar to the ratio in the original bilayer film [15]. Both arrays showed a monomodal distribution of particles, as evident from the size histograms shown in the inset, with average sizes of  $91 \pm 23$  nm and  $100 \pm 30$  nm for the 16.7 and 28.5% Co cases, respectively.

Fig. 4.2 presents the measurement of the broadband optical absorption spectrum from the nanoparticle samples as a function of the ambient aging detailed in the experimental section. Fig. 4.2(a) corresponds to the 16.7% Co case, while Fig. 4.2(b) corresponds to the 28.5% Co case. The most important feature in the optical behavior is the strong absorption peak around 500 nm that corresponds to the LSPR peak in the Co-Ag bimetal nanoparticles. With reference to the spectrums of the freshly prepared sample (i.e. labeled as 0 days in the figures) the LSPR peak occurred at 520 nm and 504 nm for the 16.7 and 28.5% Co samples, respectively. As a function of aging time, the absorbance peak intensity started to decrease and broaden. This phenomenon of intensity decrease and bandwidth broadening was clearly evident for both Co cases, as seen in Fig. 4.2(a) and (b). In fact, the LSPR peak was found to significantly decrease in intensity with increasing aging time, as clearly evident by the spectral behavior for both the samples. We had previously reported that this decrease corresponds to the oxidation of the metal nanoparticle[16] and can be quantified by measuring the bandwidth (BW) of the LSPR peak, which is the value at its full width at half maximum, as we do next. For comparison purposes, Fig. 4.2(c) shows the normalized optical absorption spectrums of freshly prepared nanoparticles of pure Ag (i.e. 100% Ag) with 16.7 and 28.5% Co NPs. It can be seen that the bandwidth for the three cases are comparable but with different LSPR wavelength positions.

In Fig. 4.3(a) we have quantified the broadening of the LSPR peaks of Fig. 4.2. Specifically, we extracted the bandwidth and normalized it with respect to its value at 0 days. This quantity,  $\Delta\lambda(0)/\Delta\lambda(t)$ , i.e. the inverse normalized bandwidth, has a value of 1 for the freshly prepared samples and decreases with increasing aging time for both Co concentrations, as evident in Fig. 4.3(a). Two distinct trends were seen for both samples. An initial slow decrease in the inverse bandwidth was followed by a rapid change, which occurred at about 166 days for the 16.7 % Co (solid triangles) and at about 365 days for the 28.5% Co (open

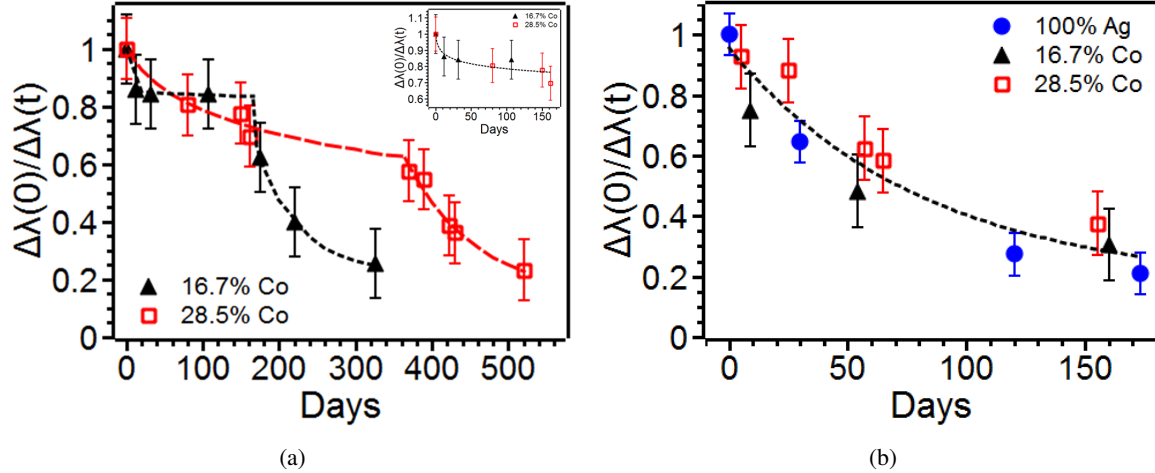


Figure 4.3: (a) The change in the normalized BW of the LSPR peak of the bimetal nanoparticles is plotted. The solid triangles corresponds to the experimental values for the 16.7% Co while the open squares correspond to the 28.5% case. An initial slow decrease is followed by a rapid decrease at a later time for both Co cases. The dashed lines correspond to fits based on the known oxidation behaviors of Co and Ag metals. The inset shows the slow decay portion of the Co-Ag particles for the 16.7% case (solid triangles) and the 28.5% case (open squares). The dashed line is an inverse-log curve as a guide to the eye. (b) The LSPR bandwidth decay of pure Ag nanoparticles (solid circle) taken from ref. [16] overlaid with the rapid decay portions of the Co-Ag nanoparticles from (a). The dashed exponential decay line serves as a guide to the eye.

squares). This initial slow decay is due to the preferential oxidation of Co [16]. Inset in Fig. 4.3(a), replots the slower stage decay for the two cases from Fig. 4.3(a). It can be seen that the slow decrease in the inverse bandwidth for both Co concentrations generally follow a similar trend, in this case an inverse log behavior shown by the dashed line with regression coefficient ( $R^2$ ) value of 0.83. This inverse log behavior of Co was similar to the previously reported trend of preferential decay of Co in the case of 16.7% Co-Ag, as verified by electron microscopy [16].

The second trend observed in Fig. 4.3(a) is the rapid decay in bandwidth at the later times, which had not been seen previously. Our analysis is that this portion of the curve is related to the decay of the remaining Ag in the Co-Ag nanoparticles. We have previously observed the decay of the LSPR bandwidth of pure Ag nanoparticles due to their oxidation in air [16]. This behavior is shown in Fig. 4.3(b, solid circles) and is taken from ref. [16]. We have also included the portions of the Co-Ag decay corresponding to the rapid decay in Fig. 4.3(a), i.e. after 166 and 365 days for the 16.7 and 28.5% Co, respectively. The similarity in the trends of the curves suggested that the rapid decay ( $R^2=0.91$ ) corresponds to the oxidation of Ag in the Co-Ag nanoparticles.

One qualitative conclusion we can draw from the results of Fig. 4.3 is that the Ag metal appears to have a large decay free lifetime when in contact with Co. We further quantified this effect through fitting and modeling, as discussed next.

The bulk oxidation behavior of Co is known to follow an inverse logarithmic behavior [172]. In Fig. 4.3(a), the dashed lines for the slow decay region of the curves are inverse logarithmic best fits to the

Table 4.1: Comparison for 50% bandwidth decay for different Co-Ag samples.

	50% decay (days)	Lifetime increment ratio
0% Co (or 100% Ag)	50 [16]	1
16.7% Co	183	3.7
28.5% Co	392	7.8

behavior and are consistent with oxidation of pure Co, suggesting that Co preferentially oxidizes in the Co-Ag nanoparticles for these concentrations. The best fit trends for the two cases were obtained to be  $\beta = 0.877 - 0.008 \ln(t)$  and  $\beta = 1.502 - 0.147 \ln(t + 30.482)$  with  $R^2$  value of 0.99 and 0.95 respectively for the 16.7 and 28.5% Co cases, respectively. Here  $\beta$  was the inverse normalized bandwidth defined previously as  $\Delta\lambda(0)/\Delta\lambda(t)$ . This result suggested that the mechanism of Co oxidation in Co-Ag does not appear to be dependent upon the amount of Co. However, the amount of Co clearly controlled the total time for the slow decay phase of the oxidation process, it was longer for the higher concentration (365 days for 28.5% Co) than the lower case (166 days for the 16.7% Co). The rapid decay portion of the BW trend with time was similar to that of pure Ag NPs [16], as shown by the dashed lines in Fig. 4.3(a). This region of the 16.7% and 28.5% Co were well described by fits of  $\beta = 0.254 + 2252.098 \exp(-t/20.073)$  and  $\beta = 0.136 + 24.443 \exp(-t/93.096)$  with  $R^2$  value of 0.99 and 0.97 respectively, respectively. Clearly, the transition point of the BW decay from slow to rapid could be used to define the lifetime of decay free Ag, i.e. the time till complete Co oxidation. Furthermore, by controlling the ratio of Co and Ag, lifetime of the decay can be controlled as evident from Fig. 4.3(a). Table 4.1 summarizes the bandwidth decay values for 50% degradation for the pure Ag, and 16.7 and 28.5% Co samples. For reference we have taken the 50% degradation in bandwidth for 100% Ag from ref. [16]. It can be noted that by keeping the amount of Ag fixed and changing the Co amount, the bandwidth decay can be slowed down by almost 8 time leading to more than a year of strong Ag plasmons.

Next, we performed an analysis to predict the oxide concentration for the slow decay region, i.e. the Co oxidation region of the curve. There were two reasons to do this. First, if one can predict the lifetime of Co in Co-Ag then Co-Ag materials can be designed through theory. Second, it could also tell us whether a complete oxidation of Co in Co-Ag NPs takes place before the decay trend changes in the Co-Ag NPs, as noticed in Fig. 4.3(a). We employed a theoretical model to describe the optical transmission signal of the Co-Ag NPs with the help of an optical mean field approximation approach (MFA) [117]. The system that can be view as a thin layer of Co, CoO and Ag nanoparticles that can be described by an effective complex dielectric function, surrounded by the substrate and air. In this form, the optical transmission can be calculated within the Fresnel approximation for the optical transmission in multilayer system. Here, we assumed the oxide of Co to be CoO [172]. The dielectric function of CoO was used to quantify the amount of oxide growth in the respective NP arrays. Due to the unavailability of the oxide data of Co in the visible range, we assumed the dielectric of the oxide as  $2 + .01i$ , independent of the wavelength for simplicity. The choice of imaginary part of the dielectric was in accordance with its low values in the IR range [173, 174] and the real part was close to its mixed oxide dielectric [174, 175]. The volume fraction used in the MFA can be approximated to the individual volume fraction of Co, CoO and Ag in a single nanoparticle. These

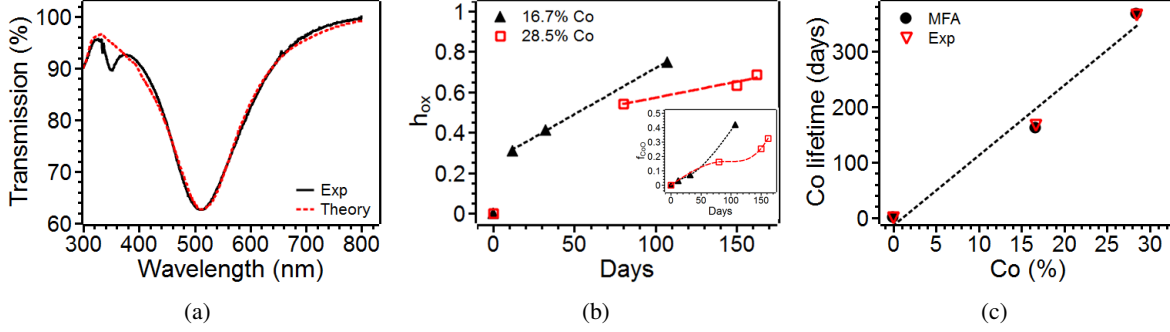


Figure 4.4: (a) The experimental transmission spectrum (solid line) shown is for the 16.7% Co sample taken after day 12. This experimental spectrum was fitted using the MFA by varying the CoO fraction to get the best fit shown by the dashed line. (b) The theoretically calculated 1-dimensional oxide thickness (of CoO) plotted as function of days. An initial period of rapid growth is followed by a slower linear trend. The life time of the Co part of Co-Ag was estimated from the linear regime of oxide growth. The inset shows the CoO volume fraction growth over prolonged time extracted by fitting the experimental transmission spectrums using MFA. The dashed and dotted lines in the inset are guide for the eyes. (c) The plot for theoretically calculated Co lifetime using MFA (solid circles) and experimental values from Fig. 4.3(a) (symbols). The dashed line is a linear fit to the data.

will allows us to calculate the complex effective dielectric function of the whole layer that is in contact to the air and the substrate. By changing the amount of oxide, the best fit for the transmission signal of the array was generated. To calculate the effective complex dielectric function of the Co-CoO-Ag layer we used the lower bound of the Bergman-Milton formalism [159, 160, 157, 158], given by:

$$\epsilon_{eff,NP} = \left( \frac{f}{\epsilon_1} + \frac{(1-f)}{\epsilon_2} - \frac{2f(1-f)(\epsilon_1 - \epsilon_2)^2}{3\epsilon_1\epsilon_2(\epsilon_2\gamma + \epsilon_1(1-\gamma))} \right)^{-1} \quad (4.1)$$

where,  $\epsilon_1$  and  $\epsilon_2$  are the complex dielectric functions of the metals or their respective oxides,  $f$  is the volume fraction of the material in a single nanoparticle and  $\gamma$  is a parameter that is related to the NPs shape. For  $\gamma = 1 - 2f/3$ , Eq. (1) corresponds to the exact Maxwell Garnett approximation as shown in ref. [159]. It is worth mentioning that Eq. 1 works extremely well for low volume fraction and small particle sizes as compared to the wavelength of light. The above equation is employed self-consistently as described in ref. [159]. To calculate the effective complex dielectric function of the Co-CoO-Ag system, Eq. 1 was employed twice, first to get the complex dielectric function of Co-CoO and then, after incorporating the Ag complex dielectric function, to get the overall effective complex dielectric function of Co-CoO-Ag NP system. The overall effective complex dielectric function of NPs in contact with air and quartz substrate was calculated self-consistently using a modified Maxwell-Garnet mixing model approach given by Eq. 1 in ref. [117].

As a final step, the theoretically predicted optical transmission spectrum of the Co+CoO+Ag NP system using the MFA approach was compared to the experimental spectrum. In Fig. 4.4(a), the theoretical fit to the experimental measurement following 12 days of aging for the 16.7% Co sample is shown. It is worth mentioning here that the peak at around 360 nm is the quadrupole plasmon visible due to the hemispherical

shape of the nanoparticle. Due to limitations of the model, it is only able to predict the dipole plasmon. To obtain the best fit to experiment, the volume fraction of Co oxidized ( $f_{CoO}$ ) was used as a fitting parameter in the MFA model. The quantified volume fraction ( $f_{CoO}$ ) obtained was converted into fractional thickness of oxide  $h_{ox}$  through the transformation  $h_{ox} = (f_{CoO})^{1/3}$ . This was done under the assumption that the oxide growth could be considered to follow 1-dimensional growth kinetics. This fractional oxide thickness is plotted in Fig. 4.4(b) for the 16.7% and 28.5% Co samples. The inset of Fig. 4.4(b) shows the  $f_{CoO}$  for the two cases. The oxide thickness grew rapidly during the initial period of aging and then followed a linear trend, as shown in Fig. 4.4(b). This linear regime of data was fitted with a straight line to calculate the fraction of Co converted to CoO. The straight line fits were determined to be  $h_{ox,16.7\%Co} = 0.00457 \times t + 0.26011$  and  $h_{ox,28.5\%Co} = 0.00158 \times t + 0.41329$  (where  $t$  is in days) with  $R^2$  value of 0.99 and 0.94 respectively for the 16.7 and 28.5% Co samples, respectively. The life time for complete oxidation of Co could be obtained by setting the left hand side of these fits to 1 (i.e. the entire Co becomes oxidized yielding  $h_{ox} = 1$ ), and yielded 161 and 367 days for the the 16.7 and 28.5% Co cases, respectively. This theoretically predicted lifetime of Co showed very good agreement with the experimentally observed time at which the slow decay region turned into the rapid decay in Fig. 4.3(a). The various values are plotted in Fig. 4.4(c), with the 0% Co (or pure Ag) case assumed to be 0 days since the Ag starts oxidizing immediately after it has been prepared. The solid circles are the theoretical lifetimes for Co oxidation calculated using MFA while the experimentally determined values are shown by hollow triangles. Clearly, the Co lifetime follows a linear trend ( $R^2=0.97$ ) with Co concentration and the slope has a value of 12.7 days/Co %, implying that the stable lifetime of Ag can be simply controlled by changing the amount of Co. This result confirmed our earlier analysis that the rapid decay is the oxidation of Ag and occurs once all the Co in the Co-Ag has been oxidized. In other words, the Co provides an oxide free Ag for long times, as shown in Fig. 4.4(c) and can be tuned by noting that the slope in Fig. 4.4(c) is 12.7 days/concentration. Besides the evidence for an 8 fold increase in the oxide-free Ag lifetime with the 28.5% Co, which leads to a very stable LSPR signal, we also determined the overall shelf life of Co-Ag NPs as the time required for the complete oxidation of the particles. From this, the increase in shelf life over that of pure Ag was calculated by dividing the lifetime for complete oxidation (i.e. no LSPR peak was evident) of Co-Ag with that of pure Ag (187 days, ref. [16]). The shelf life increments for 16.7 and 28.5% Co came out to be 189 and 295%, respectively.

*In this chapter we established the oxidation lifetimes of different compositions of Co-Ag NPs using MFA model.*

## 4.4 Acknowledgment

The authors acknowledge support by the Army Research Office through grant W911NF-13-1-0428 and the NSF through grant ECCS-0850574. Authors also acknowledge support by the Center for Materials Processing. A portion of this research was conducted under grant CNMS2013-284 at the Center for Nanophase Materials Science, which is sponsored at ORNL by the Scientific User Facilities Division, Office of Basic Energy Sciences, U.S. Department of Energy. Ritesh Sachan helped out with the synthesis of nanoparticles



and Vanessa Ramos did some of the optical measurements.

## Chapter 5

# Plasmonic quality factor and quantum efficiency of hemispherical Ag and bimetal AgCo nanoparticles

### 5.1 Summary

In this chapter, an extensive experimental investigation of the plasmonic bandwidth and quality factor of hemispherical shaped Ag nanoparticles was performed as a function of particle size (volume) and resonance energy. The hemispherical shaped Ag nanoparticles were prepared by pulsed laser dewetting and their optical spectra was investigated for different volumes and for immersing in different environments including air, various dielectric liquids (acetone, methanol, Toluene, glycerol), semiconductors (CdS, and a novel amorphous oxide Fe-Tb-Dy-O) and metal films (Co, Fe). This resulted in a comprehensive understanding of the quality factor of Ag hemispheres as a function of volume and energy. Next, we prepared AgCo hemispherical bimetallic nanoparticles by laser dewetting with a variety of composition and size and characterized their bandwidth in air ambient. By utilizing some approximations to simplify the contributions of various relaxation times that influence the dephasing process of the plasmon resonance and hence its bandwidth, we were able to estimate the independent contributions of radiative and non-radiative components of the plasmon dephasing process. From this the quantum efficiency for radiative energy transfer was calculated. We found that the bimetal nanoparticles can have comparable quality factor and quantum efficiency as the pure Ag nanoparticles.

### 5.2 Results

#### 5.2.1 Optical spectroscopy of Ag nanoparticles

Ag nanoparticle arrays were prepared on transparent glass substrates for transmission spectroscopy characterization. Such particles have been well documented to have a nearly hemispherical shape [176, 15, 16, 17]. We created arrays in which the average particle volume varied between  $4 \times 10^3$  to  $2 \times 10^6$  nm<sup>3</sup>. Fig. 5.1

(a) is a representative SEM image of freshly prepared pure Ag NPs synthesized by pulsed laser dewetting of  $\sim 1.5$  nm thick Ag film. The inset of the image shows the size histogram of the particle size distribution, which is monomodal, and has an average particle diameter of  $36 \pm 11$  nm. Similar such arrays with different average sizes of Ag NPs were synthesized by dewetting of Ag films with different thickness and characterized for their size and optical properties. Fig 5.1 (b) shows the normalized broadband absorption spectrum vs energy for Ag NPs as a function of average diameter. The maxima in the absorption spectra corresponds to the position of the localized surface plasmon resonance (LSPR) or plasmon resonance energy ( $E_{res}$ ) for a metal nanoparticle. It can be seen from Fig. 5.1 (b) that as the NP diameter increases the plasmon resonance energy decreases (i.e. plasmons red shift). Another feature that is evident is that absorption spectrum broadens, i.e. the bandwidth of the peak increases. Both these features are consistent with the size-dependent behavior of nanoparticles [3]. From the optical spectra in Fig. 5.1 (b), it was possible to generate the trend in LSPR energy and the energy bandwidth ( $\Gamma$ ) as a function of particle diameter, and this is shown in Fig. 5.1 (c). In Fig. 5.1(c, left y-axis), the black hollow circles correspond to the plasmon resonance energy, which showed a linearly decreasing trend as a function of diameter and could be expressed as  $E_{res} (eV) = 3.0139 - .0056D (nm)$ , where plasmon resonance energy,  $E_{res}$ , is in eV and the NP diameter  $D$  is in nm. In Fig. 5.1 (c, right y-axis) the solid red circles correspond to the energy bandwidth  $\Gamma$ . The energy bandwidth was obtained from the absorption spectra by fitting a single Lorentzian peak at the resonance energy. It is worth mentioning that this since this bandwidth is from a nanoparticle array with a broad size distribution, it will also intrinsically include contributions from in-homogeneous broadening that arise due to different size-dependent contributions to broadening. However, in-homogeneous broadening appears as a Gaussian correction to the Lorentzian line shape of the plasmonic signal. In Fig. 5.2 we show the comparison between the experiment curve to fits containing either a single Lorentz shape, a single Gaussian shape and Voigt shape. Since the single Lorentz shape showed excellent fits (showed best  $R^2$  values out of the three fits) to the experimental spectra, we inferred that contribution from in-homogeneous broadening was small and ignored this in our subsequent analysis.

## 5.2.2 Pure Ag nanostructures in different environments

Following the above optical investigations of Ag in ambient air environment, we embedded the Ag arrays in various other environment so that the resonance energy could be changed independently of the volume of the particle. These optical measurements and their results are described next.

1. *Embedding in dielectric media:* The Ag NP arrays with different average volumes (ranging between  $6.5 \times 10^4$  to  $3 \times 10^5$  nm<sup>3</sup> that corresponded to diameters between 65 to 105 nm) were placed in dielectric mediums with different refractive index, i.e. methanol, glycerol, acetone, toluene or machine oil, and their optical transmission spectra was recorded. Fig. 5.3 (a) compares the optical absorption spectra for the Ag array in air versus immersion in 5 different fluids. Immersion in all the dielectric fluids red shifted the plasmon energy. From such measurements, the position of the resonance energy and the  $\Gamma$  were calculated for various Ag size and dielectric, and the resulting behavior is shown in Fig. 5.3 (b) and (c) respectively. It was evident that the resonance energy decreased from its value in

air (open circle) following immersion in the different fluids, and the resonance peak broadened, i.e. the energy bandwidth increased.

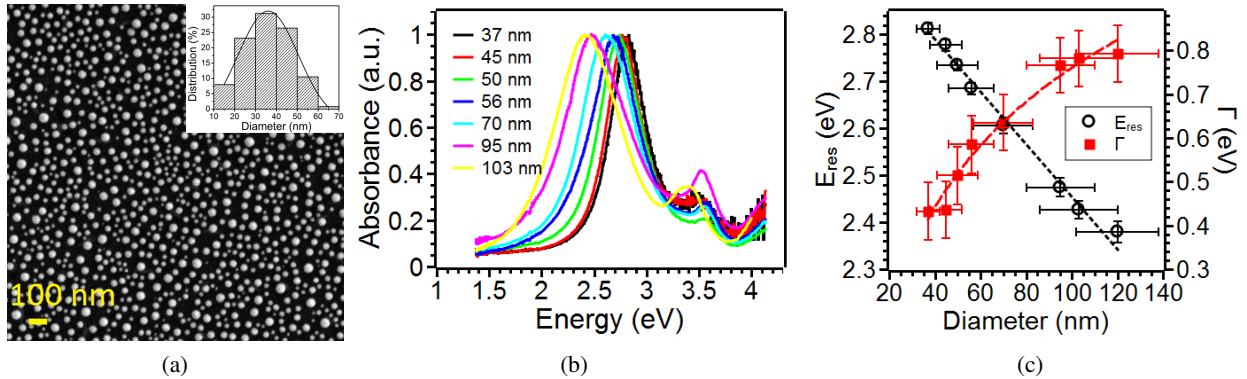


Figure 5.1: (a) SEM image of pure Ag NP array of size  $36 \pm 11$  nm with the particle size distribution histogram is in the inset. (b) The normalized absorption spectrum of different sized hemispherical NPs plotted as a function of energy. (c) The plasmon resonance energy and the bandwidth are plotted as a function of Ag NP size. The black hollow circles and the solid red squares denotes plasmon resonance energy and the bandwidth, respectively. The black dotted and the dashed red lines are the best fits for the experimental data.

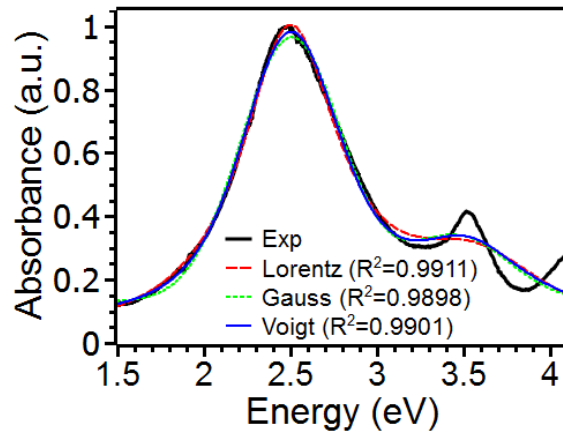


Figure 5.2: Compares the Lorentz, Gaussian and Voigt fits to the experimental optical spectrum.

2. *Ag in semiconductor media*: The Ag NPs were placed in semiconductor-rich environment by depositing thin films of the semiconductor material onto the Ag NPs. Two different semiconductors were used in this study: cadmium sulfide (CdS) and an amorphous ternary semiconductor oxide of type  $(Tb_{0.3}Dy_{0.7})Fe_{1.92}$  [177]. Fig. 5.4 (a) shows the effect of increasing the amorphous oxide semiconductor film thickness from 2 to 9 nm on the Ag NP optical spectra. As the film thickness increased, the plasmon energy red-shifted and the BW increased. Similar behavior was observed recently when CdS films were deposited onto Ag NP arrays [178]. In Fig. 5.4 (b) the collated behavior of bandwidth versus the resonance energy position is shown for Ag in the two dielectric containing varying amounts of semiconductor film. The CdS data was extracted from results published in ref. [178]. The squares

and circles correspond to CdS on Ag NP and the blue diamond symbol corresponds to the amorphous oxide on Ag. Again, like in the case of the dielectric behavior [Fig. 5.3(c)], the bandwidth increased with increasing resonance energy.

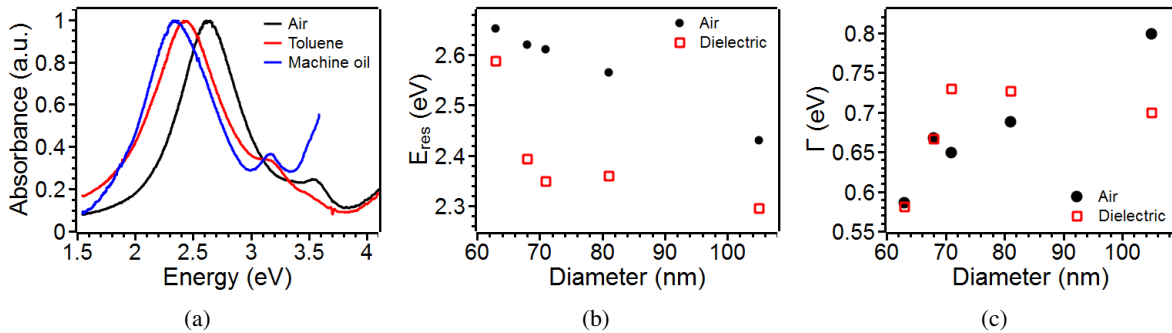


Figure 5.3: (a) Compares the absorption spectrum of Ag NPs in air with that of the Ag NPs dipped in toluene and machine oil. (b) Compares the resonance energy of Ag NPs measured in air and different dielectrics as a function of Ag NP size. (c) Compares the bandwidth of Ag NPs measured in air and different dielectrics as a function of Ag NP size.

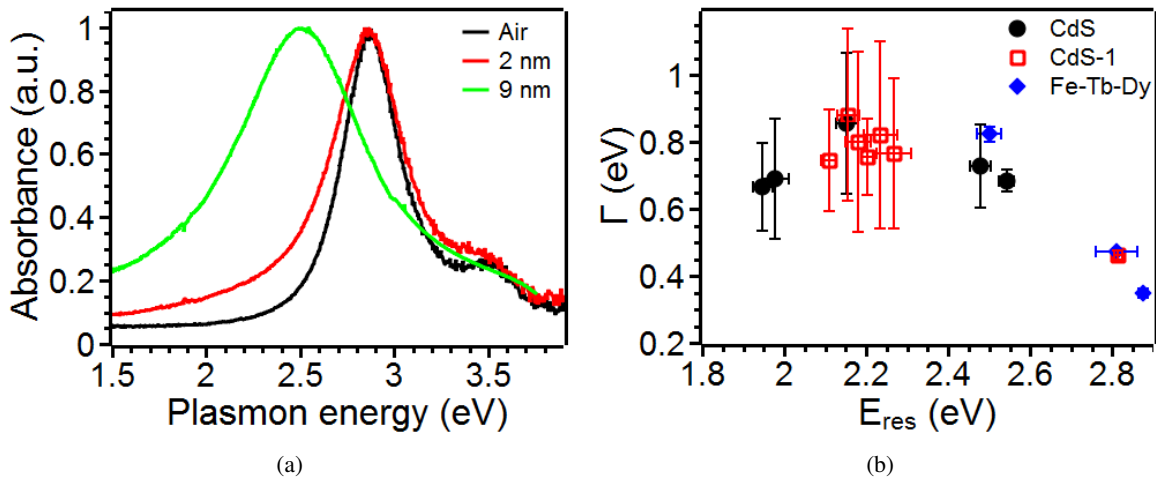


Figure 5.4: (a) Compares the absorption spectrum of Ag NPs embedded in Fe-Tb-Dy amorphous semiconductor oxide. (b) Compares the BW of Ag NPs embedded in Fe-Tb-Dy amorphous semiconductor oxide and CdS film as a function of resonance energy.

3. *Ag in metal media*: Similar to the above semiconductor case, we also embedded synthesized hemispherical Ag NPs in varying thickness of Co and Fe metal films and measured the optical behavior. Fig. 5.5 (a) corresponds to Ag in Co films (with thickness from 1 to 7 nm) while Fig. 5.5 (b) corresponds to the spectra for Ag in Fe films with thickness from 4 to 8 nm. Again, as metal film thickness increased, the plasmon resonance energy shifted to lower energy values and the spectrum broadened. Fig. 5.5 (c) collects together the bandwidth of the Ag NPs embedded in Co and Fe films as a function of the resonance energy. Again, the bandwidth for embedded Ag NPs decreased with increasing energy.

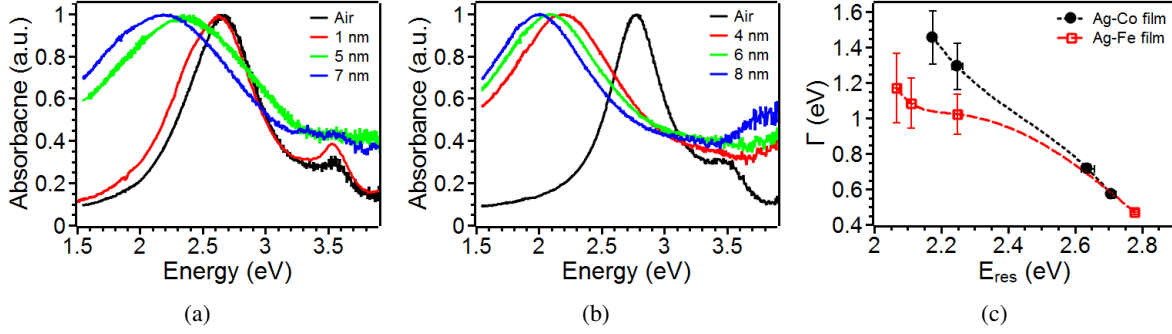


Figure 5.5: Shows the normalized absorption spectrums of Ag NPs embedded in (a) Co film and (b) Fe film. As the thickness of the metal film is increased, the plasmon energy decreases. (c) Compares the BW of Ag NPs embedded in Co and Fe metal film as a function of resonance energy.

### 5.2.3 Bimetallic Ag nanostructures

Bimetallic nanoparticles of Ag-Co were synthesized and their resonance energy and bandwidth were studied for various Ag-Co compositions. Two different initial thin film bilayer configurations of Co-Ag were used to synthesize nanoparticles with varying size and composition through laser dewetting. One configuration, referred to as Co5Ag, consisted of a bottom Ag film thickness fixed at 5 nm with a top Co film thickness varied from 1 to 5 nm. The second configuration consisted of 5AgCo, which meant the top Ag layer thickness was fixed at 5 nm and was deposited onto underlying Co films whose thickness ranged from 1 to 5 nm. From this, different compositions and volumes of Ag-Co bimetal NPs were obtained. A representative SEM of a AgCo NP array synthesized by laser dewetting of a bilayer consisting of 5 nm thick Ag on 2 nm thick Co layer is shown in Fig. 5.6 (a). Shown in the inset is the size histogram, and the monomodal distribution of particles with average size of  $113 \pm 30$  nm. The shapes of these Ag-Co nanoparticles have also been confirmed to be near hemispherical[15, 16, 17]. The normalized absorption spectra of Co5Ag and 5AgCo systems are plotted in Fig. 5.6 (b) and (c). Fig. 5.6(d) compares the plasmon resonance energy of the two bimetallic systems as a function of the total NP size. It was seen that on increasing the NP size, the plasmon red shifted, consistent with previous reports on such bimetallic systems [15, 117]. Next, the plasmon energy was plotted as a function of Co percentage (in volume percent) and is shown in Fig. 5.6 (e). For identical Co %, the plasmon energy was different for the nanoparticles made from the AgCo vs CoAg configurations, and this was due to the fact that the two cases produced different average particle sizes, as detailed in previous studies of bilayer dewetting [154, 179, 180, 15]. In Fig. 5.7 (a) the bandwidth is shown as a function of the resonance energy, Fig 5.7 (b) shows it as a function of the bimetal nanoparticle volume and Fig. 5.7 (c) shows it as a function of Co %. These general trends appeared similar to those found for pure Ag nanoparticles, i.e. bandwidth decreased as resonance energy increased and it decreased as particle volume increased. However, some very unexpected attributes were found in the bimetal nanoparticles upon comparing to pure Ag, as we discuss in the next section.

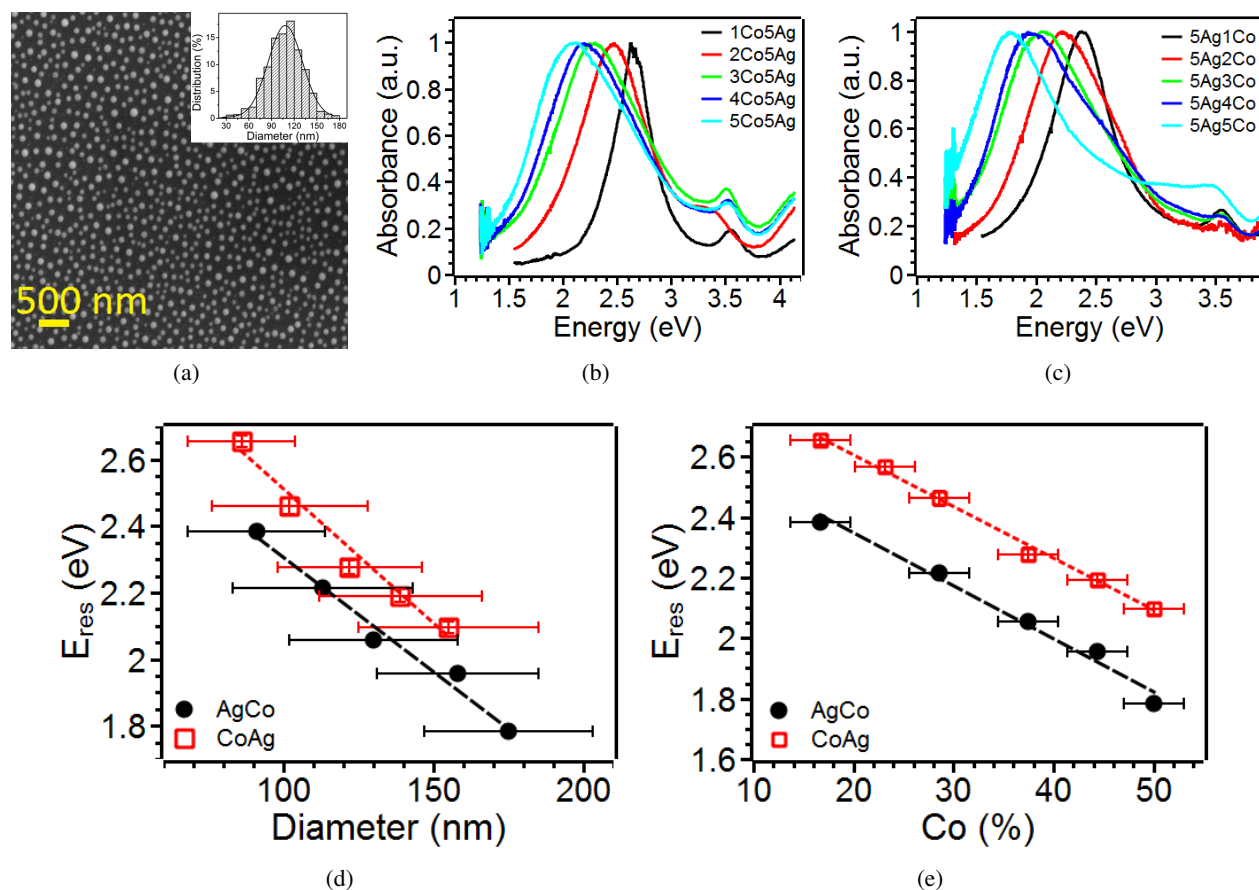


Figure 5.6: (a) Representative SEM image of Co-Ag NP system. The SEM corresponds to Ag (5 nm)/Co (2 nm) with the average NP size of  $113 \pm 30$  nm. The inset shows the size distribution histogram. (b,c) Corresponds to the normalized absorption spectrums of Co-Ag bimetallic system. The Ag film thickness is fixed at 5 nm and the Co thickness is varied from 1-5 nm. The absorption spectrums in (b) are for Co/Ag and in (c) for Ag/Co configuration. (d) Plots the plasmon energy as a function of NP size for the two Co-Ag systems. (e) Plots the plasmon energy as the function of the Co percentage in the NP system.

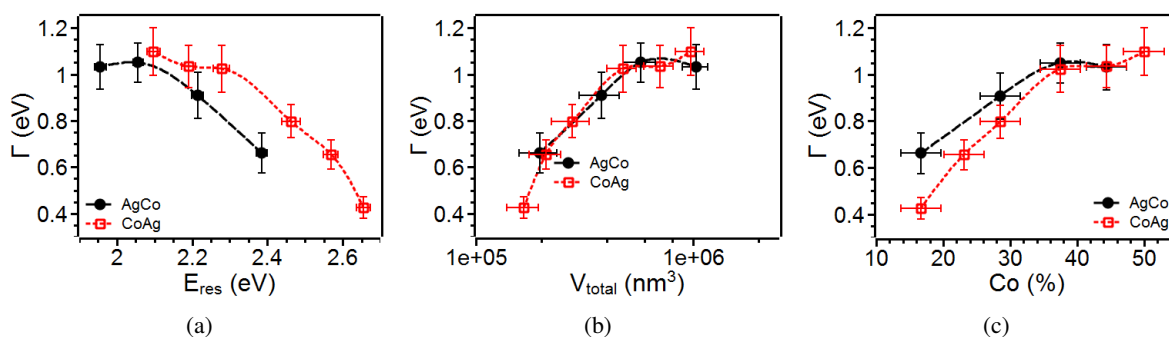


Figure 5.7: BW dependence of CoAg bimetal on (a) resonance energy, (b) volume of the bimetal nanoparticle and (c) Co amount (volume %).

### 5.3 Discussion

The quality factor of a plasmon resonance is one of the most important characteristics in determining the usefulness of a material for plasmonic applications. The quality factor can be calculated experimentally through the function  $Q = \frac{E_{res}}{\Gamma}$ , where  $E_{res}$  corresponds to the resonance energy and  $\Gamma$  is the energy bandwidth. As mentioned in the introduction of this thesis, and shown in ref. [97], the quality factor is a measure of how effectively the nanoparticle interacts with light and only a few metals (Ag, Au etc.) show strong interactions (resonances) because of their high  $Q$ . One of the direct impacts of the quality factor is the ability of nanoparticles to sense changes in their local environment, which is the basis for the technique of localized surface plasmon resonance sensing or LSPR sensing. It is well known that particle with higher quality factor show higher sensitivity to detection[181]. A second characteristic highly relevant to many plasmonic applications is the ability of the plasmonic nanoparticle to efficiently couple to light and subsequent transfer photons into the surrounding environment, such as would be needed in imaging or solar energy harvesting. This ability is measured by the quantum efficiency  $\eta$ , which is defined as  $\eta = \frac{\Gamma_{1R}}{\Gamma_{1R} + \Gamma_{1NR}}$ , where the various quantities are the radiative energy bandwidth ( $\Gamma_{1R}$ ) and the non-radiative energy bandwidth ( $\Gamma_{1NR}$ ). Despite a large number of investigations of the plasmonic quality factor of nanoparticles as a function of material, shape, and size, there is very little known about the quality and quantum efficiency of hemispherical shaped particles of Ag or bimetallic Ag.

#### 5.3.1 Quality factor of hemispherical nanoparticles

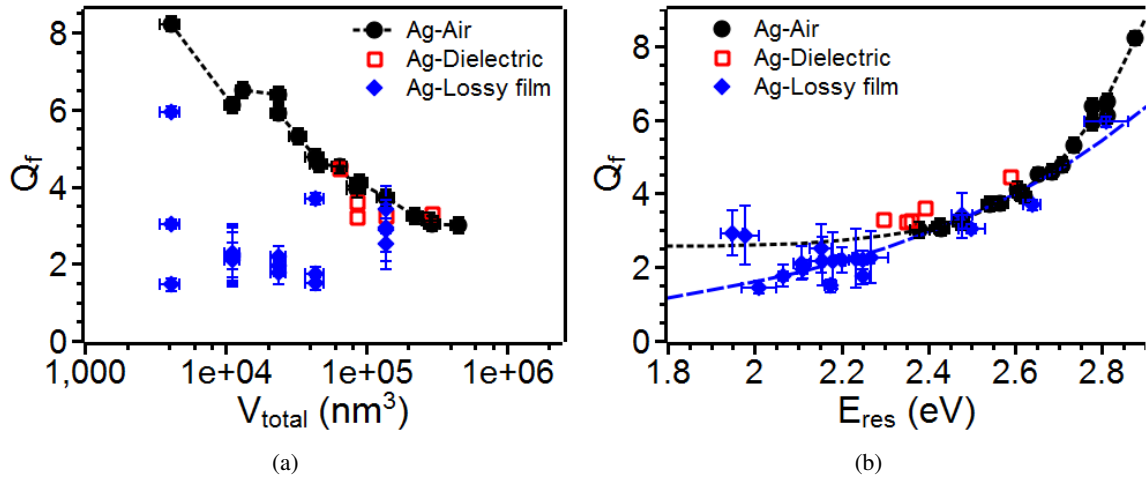


Figure 5.8: *Quality factor for Ag in various environments. (a) Dependence of  $Q$  on particle volume. (b) dependence of  $Q$  on resonance (LSPR) energy.*

In Fig. 5.8 the  $Q$  of hemispherical Ag nanoparticles in the various dielectric, semiconducting, and metal environments is shown as a function of particle volume [Fig. 5.8(a)] and resonance energy [Fig. 5.8(b)]. The overall trends for  $Q$  within each environment class is a decrease with increasing volume and increase with increasing resonance energy. However, as evident from Fig. 5.8(a) the  $Q$  in the metal and semiconductor environment is substantially lower than in the dielectrics for a fixed particle volume. This is consistent with



the intuitive understanding that embedding the plasmonic nanoparticle in a lossy medium (i.e. semiconductor or metal) should generally decrease the strength of the resonance. This decrease in  $Q$  is also evident in the trend of  $Q$  versus  $E_{res}$ , shown in Fig. 5.8(b). While the Ag in air and Ag in dielectric appear to have similar magnitude and lie on a single trend line, the Ag in semiconductor and metal clearly appear to be shifted to lower values. All in all, it is not surprising that the  $Q$  factor for the Ag is significantly lower in the lossy medium.

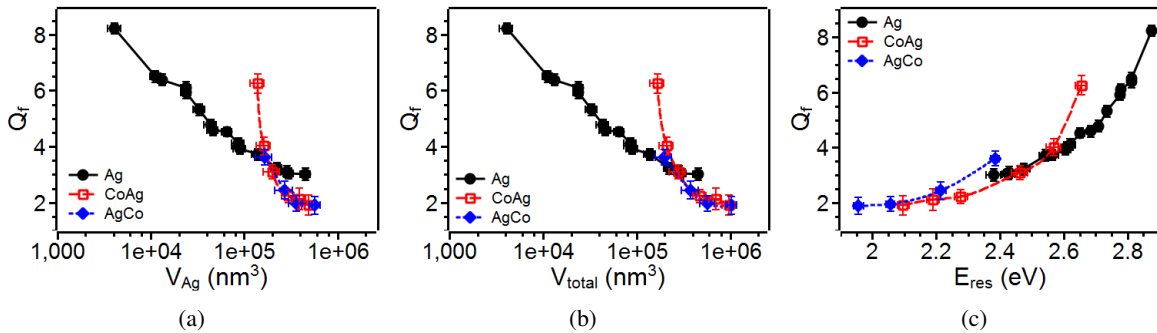


Figure 5.9: *Quality factor for Ag versus AgCo in air. (a) Dependence of  $Q$  on the effective volume of Ag within the nanoparticle. (b) Dependence of  $Q$  on the total volume of nanoparticle. (c) dependence of  $Q$  on resonance (LSPR) energy.*

In Fig. 5.9 the  $Q$  of hemispherical Ag nanoparticles is compared to the  $Q$  of the bimetallic hemispherical AgCo nanoparticles, and both values were for the particles embedded in air environment. Fig. 5.9(a) shows the behavior as a function of the volume of Ag in the nanoparticles. In the case of the laser dewetted AgCo bimetallic nanoparticles, it has been shown by SEM investigations that the average amount of Ag in each AgCo nanoparticle is in the ratio of the original film thickness ratio [15] and so it is possible to calculate the effective Ag volume for the AgCo bimetals. As Fig. 5.9 (a) shows, the AgCo has comparable  $Q$  values to that of Ag. In fact, for a small volume region between  $\sim 1$  to  $2 \times 10^5 nm^3$  (corresponding to diameters of 70 to 90 nm), the bimetallic system has comparable or better  $Q$  than that of pure Ag. This is an astonishing result given the previous findings from Fig. 5.9 (a) that Ag exposed to small quantities of lossy metals leads to significant reduction in  $Q$ . Clearly the bimetallic nanoparticles do not appear to fall into this general rule. In Fig. 5.9 (b) the  $Q$  is shown as a function of the total volume of the particle, i.e volume of pure Ag and the AgCo. Again, it is clearly evident that for large particles with volume between  $\sim 1.5$  to  $2.5 \times 10^5 nm^3$ , the AgCo has comparable or better  $Q$  than an equivalent volume of Ag. This interesting behavior was also clearly evident when the  $Q$  was plotted as a function of the resonance energy, as shown in Fig. 5.9 (c).

### 5.3.2 Model for plasmon bandwidth

To understand the behavior of the bandwidth under the various cases of varying resonance energy and volume, we begin with the interpretation of the change in bandwidth for plasmonic absorption based on a two-level model, analogous to molecular spectroscopy, in which the plasmon decays by dephasing of the coherent oscillations at a total rate given by [96]:

$$\Gamma_2 = \frac{\hbar}{T_2} = \frac{\hbar}{2T_1} + \frac{\hbar}{T_2^*} \quad (5.1)$$

where,  $c$  is the speed of light,  $\hbar$  is Planck's constant,  $T_1$  is the electron relaxation time due to inelastic processes such as radiative loss and non-radiative absorption, and  $T_2^*$  is the dephasing due to elastic scattering processes such as electron collision with other electrons, defects, and/or surfaces. Since the inelastic process has contributions primarily from radiative loss, i.e. emission of photons and non-radiative damping such as due to intra- and inter-band transitions of electrons [80]), so the total dephasing energy bandwidth can then be expressed:

$$\Gamma_2 = 2^{-1}\Gamma_{1,R} + 2^{-1}\Gamma_{1,NR} + \Gamma_{*2} \quad (5.2)$$

where the subscripts  $R$  and  $NR$  refer to radiative and non-radiative components, respectively. To interpret our experimental data we have simplified this function based on certain approximations valid in the particle size range of our investigations (i.e. 20 to 200 nm) so as to be able to independently establish the role of volume and resonance energy on the bandwidth. These approximations are discussed next.

1. *Dephasing by electron scattering*: The broadening of the plasmon peak due to elastic scattering is a result of many events happening locally such as electron-electron, electron-phonon, electron-defect, and electron-surface scattering processes [41, 99]. The damping constant (inverse of the electron relaxation times) of these events are analogues to electrical resistances and are additive. In bulk materials, electron-phonon scattering dominates, but as the size of the NP is decreased other events start to dominate. For a NP whose size is comparable to the mean free path of electron, electron-surface scattering is a dominant effect and in the simplest model the size-dependent elastic dephasing energy rate is given by:

$$\frac{\hbar}{T_2^*} = \frac{\hbar}{T_2^o} + A \frac{2\hbar v_F}{D} \quad (5.3)$$

where  $\frac{1}{T_2^o}$  is the bulk damping constant,  $A$  includes details of the scattering process,  $v_F$  is the Fermi velocity and  $D$  is the radius of the NP. Since the damping rate is inversely proportional to the diameter of the NP so the effect of surface scattering decreases as the size of the NP increases. It is generally believed that the effect is dominant primarily for noble metal (Ag, Au) NPs with diameter less than ~40 nm [99]. As the NP size increases, the percentage contribution of size to dephasing rate decreases very rapidly, and for other parameters being the same, the dephasing rate decreases by factor of 10 on increasing the size from 10 nm to 100 nm. Since our work involves Ag nanoparticles with size range between ~20 to 200 nm in diameter, we can safely assume that surface scattering is a negligible and overall contribution to the size dependent bandwidth or quality factor changes observed experimentally (For example in Fig. 5.1(c) or Fig. Fig 5.7 (b)). A second approximation that can be used is related to the quantitative value of the bulk elastic dephasing energy for Ag metal, which is ~0.02 eV [80]. When this value was compared to the measured values of the bandwidth [for example in Fig. 5.1 (c) or Fig. 5.7 (b)], it was clear that the bulk elastic dephasing is a negligible component

of the total dephasing rate and so could be neglected in all our subsequent analysis. Based on this first simplification, the bandwidth could now be written as:

$$\Gamma_2 = 2^{-1}\Gamma_{1,R} + 2^{-1}\Gamma_{1,NR} \quad (5.4)$$

2. *Quasistatic approximation*: In this quasi-static limit of plasmon excitation, the nanoparticle is sufficiently smaller than the exciting electromagnetic wavelength so such that the entire particle can be considered to be excited by the same phase and magnitude of the electromagnetic field. In this regime two important simplifications enter the interpretation of the bandwidth.

The first is that the non-radiative loss is only dependent on the dielectric function of the metal and is independent of size, shape, and surrounding ambient [182]. This can be understood by the fact that the energy location of the plasmon resonance in the quasi-static limit corresponds to a resonance in the polarizability  $\alpha(\omega)$  of the nanoparticle, which, for a spherical nanoparticle, can be written as [3]:

$$\alpha(\omega) = \frac{\pi D^3}{2} \frac{\epsilon_m(\omega) - \epsilon_h(\omega)}{\epsilon'_m(\omega) + i\epsilon''_m(\omega) + 2\epsilon_h(\omega)} \quad (5.5)$$

where  $\epsilon_h(\omega)$  and  $\epsilon_m(\omega)$  are surrounding media and metal dielectrics, respectively. Since the metal can have a negative value of the dielectric function, the Mie or Frohlich resonance condition for the appearance of the plasmons is when  $\epsilon'_m(\omega) = -2\epsilon_h(\omega)$ . At this point, the width of the resonance is given only by the magnitude of the imaginary part of the metal dielectric, i.e.  $\epsilon''$  [100, 101]. In Fig. 5.10, the imaginary part of the dielectric function for Ag and Co are shown as a function of energy. From this one can predict that as the energy increases in the window of 1 to 3 eV, the bandwidth should decrease due to the decrease in the imaginary component of the dielectric. Indeed, this is generally what is observed in our experimental measurements [Fig. 5.1 (c) and Fig. 5.7 (b)]. A second important feature evident from this figure is that the loss in Co metal is significantly higher than that of Ag and can directly explain the significantly increased bandwidth (decreased quality factor) when the Ag nanoparticles are embedded in thin layers of the Co (or Fe) metal film, as seen in Fig. 5.5 (a) or 5.5 (b).

3. *Volume dependence*: The radiative loss is only function of the volume of the nanoparticle and can be expressed as  $\Gamma_{1,R} = KV$ , where  $K$  is a constant and  $V$  is the volume of the particle. This behavior was verified by Sonnichson et al. in their studies comparing the behavior of Au spheres with Au nanorods [95].

Based on these two simplifications, the total bandwidth can now be expressed as a sum of two contributions that are independently dependent on the particle volume and energy in the form:

$$\Gamma_2(V, E) = 2^{-1}\Gamma_{1,R}(V) + 2^{-1}\Gamma_{1,NR}(E_{res}) \quad (5.6)$$

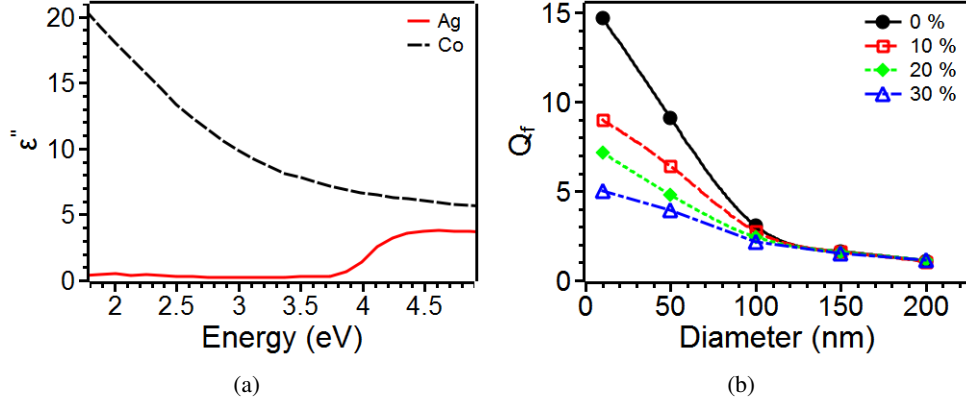


Figure 5.10: (a) Imaginary component of the dielectric function  $\epsilon''$  of Ag (solid line) and Co (dashed line) as a function of energy. (b) The quality factor for AgCo bimetal spheres calculated using Mie theory with an effective medium approach to calculate the dielectric function.

### 5.3.3 Calculation of the non-radiative and radiative dephasing rates

Based on eq. 5.6, the experimentally measured bandwidth can be utilized to extract the radiative and non-radiative components provided independent measurements of the total bandwidth can be made with a fixed volume and varying plasmon energy or vice-versa. Here we have performed this decoupling of the two contributions by varying the energy of the plasmon resonance energy through change in the volume of the Ag nanoparticle. This was done by preparing triangular shaped truncated pyramid nanoparticles of Ag through NSL, which has been described earlier. In Fig. 5.11 (a) a representative SEM image for the nanotriangles synthesized using a 200 nm PS mask template is shown. Fig 5.11 (b) shows the absorption spectrum for different volumes of the Ag nanotriangles achieved by changing the base of the triangle and keeping the height of the triangle fixed at 25 nm. This was achieved by forming the triangles with NSL using PS beads of size 100, 200 and 500 nm diameter. The plasmon resonance energy decreased on increasing the volume of the triangle and is consistent with the volume argument that on increasing the aspect ratio of a nanostructure, the plasmon resonance energy red shifts [155]. Fig 5.11 (c) and (d) shows the variation of the plasmon resonance energy and BW as a function of the volume of the triangles. Both plasmon resonance and BW increases with increasing volume. The increase in plasmon energy with increase in volume can be explained by the fact that the plasmon resonance energy decreases with increase in the aspect ratio. For the nanotriangle case, the aspect ratio is defined as base/height of the triangle hence the small volume of nanotriangles will have lower resonance energy. The BW increases with increase in the volume of nanotriangles due to the radiative part of the BW starts to dominate.

Next, we compared the bandwidth of the Ag triangles with the Ag nanoparticles as a function of the resonance energy for values measured in air ambient, and this is shown in Fig. 5.12(a). It was observed that as the plasmon resonance energy increased, the BW for the hemisphere decreased while for nanotriangles, it increased. More importantly, from the data in Fig. 5.12(a) it was possible to extract the direct contribution of the radiative energy bandwidth as follows. As mentioned previously, in the quasi-static approximation, the difference in bandwidth for a given energy can only come from a difference in volume and this can be used

to explicitly calculate the radiative component  $\Gamma_{1,R} = KV$ . From Fig. 5.12(a), we estimated the bandwidth difference  $\Delta\Gamma$  arising from the volume difference  $\Delta V$  between the hemisphere and triangle for various values of the resonance energy and the averaged out value for  $K$  came out to be  $8.88 \times 10^{-7} \text{ eV/nm}^3$ , shown in Fig. 5.12(b) as the dashed line. Now it was possible to explicitly estimate the radiative contribution and non-radiative contributions for the various Ag nanoparticles, and this is shown in Fig. 5.13(a) as a function of the resonance energy and in Fig. 5.13(b) as a function of the particle volume measured in air. From this we determined that the non-radiative contribution in hemispherical Ag was a larger contribution to the bandwidth for energies  $> 2.38 \text{ eV}$  and particle volumes between  $10^3 \sim 4 \times 10^5 \text{ nm}^3$ .

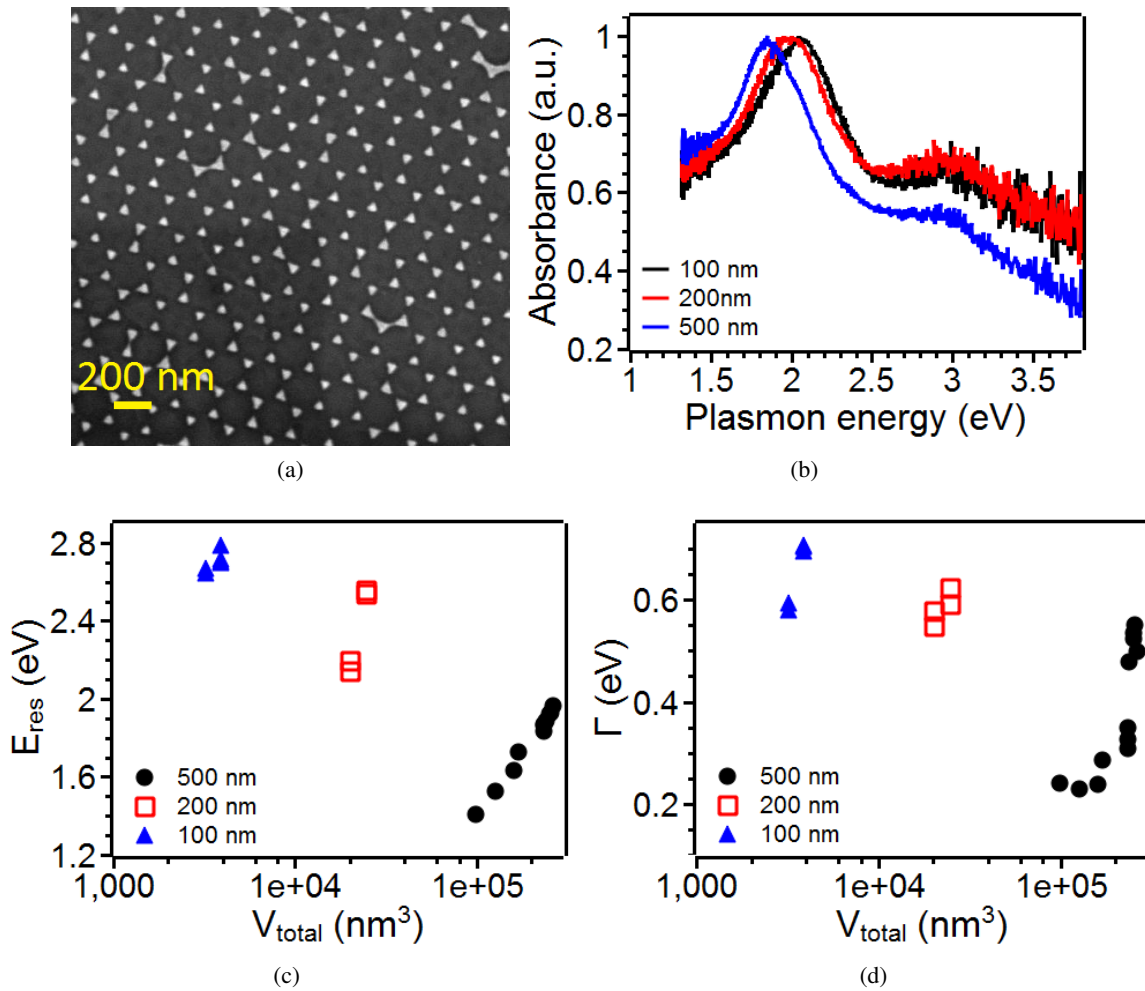


Figure 5.11: (a) SEM image of the Ag nanotriangle array synthesized by NSL using a template of 200 nm PS beads with the height of the triangles equal to 25 nm. (b) Normalized absorption spectrums of Ag nanotriangles of height 25 nm formed by PS bead templates of 100, 200 and 500 nm. As the size of the PS bead is increased, the Ag plasmon shifts toward lower energy (red shifts). (c) Plots the plasmon resonance energy and (d) BW as a function of volume of the nanotriangles formed by different PS bead templates.

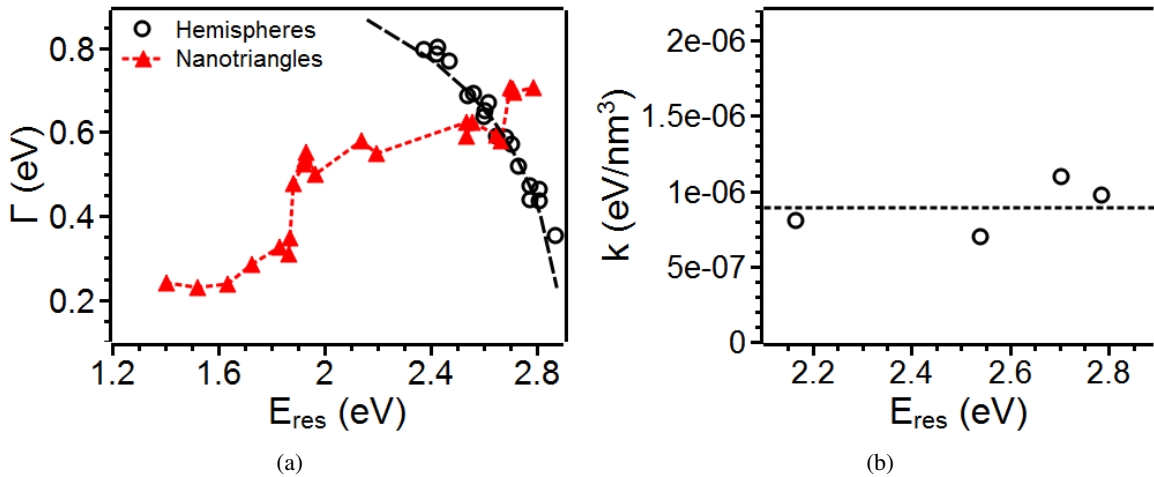


Figure 5.12: (a) Compares the BW of hemispherical Ag NPs with Ag nanotriangles plotted against the plasmon energy. As the plasmon resonance energy increases, the BW of nanotriangles increased while that of hemisphere decreased. (b) Plots the K values calculated at the different plasmon resonance energies. The dashed line represents the average K value for the data set plotted.

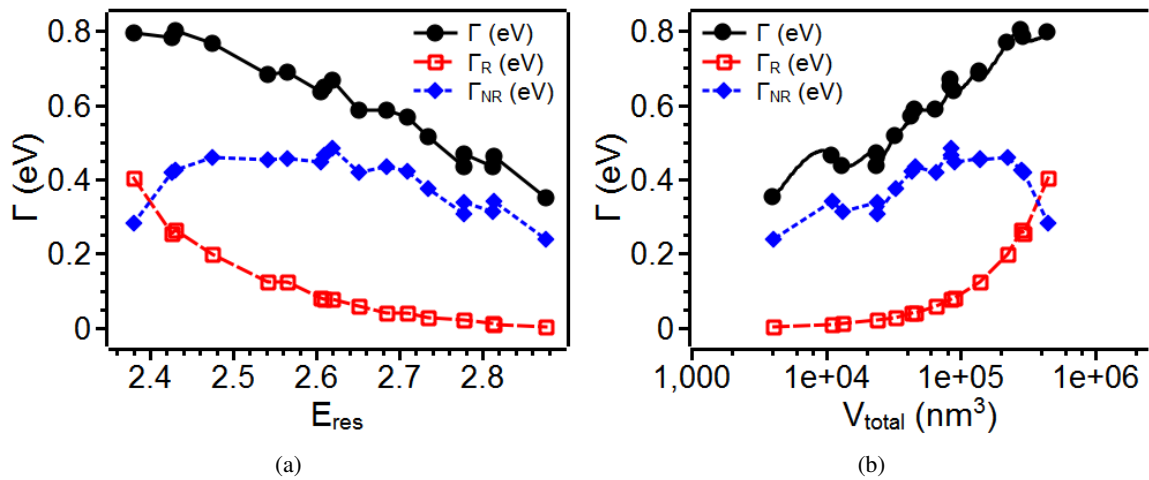


Figure 5.13: Radiative and non-radiative contributions to the total bandwidth of Ag NPs. (a) Energy dependence of the bandwidth contributions. (b) Volume dependence of the bandwidth contributions (note log scale on x-axis).

### 5.3.4 Ag vs AgCo: Radiative and non-radiative contributions

Having established the values of the radiative and non-radiative contributions to the plasmon bandwidth in pure Ag, we can now interpret the behavior for AgCo. As has been detailed previously, the AgCo bimetal consists of distinctly segregated regions of Ag and Co, due to their immiscibility. In other words, the Ag region is identical to pure Ag in its composition. On this basis, one can expect that, for the Ag region, the intrinsic loss effects such as bulk elastic dephasing rate and the non-radiative contribution to the dephasing should be identical to that of pure Ag. Overall, since the total bandwidth is an additive sum of the various contributions, we considered that the overall response of a Ag+Co nanoparticle should be the sum of various contributions as:

$$\Gamma_2^{Ag+Co} = 2^{-1}(\Gamma_{1,R}^{Ag} + \Gamma_{1,R}^{Co}) + 2^{-1}(\Gamma_{1,NR}^{Ag} + \Gamma_{1,NR}^{Co}) + \Gamma^{Ag} *_{2} + \Gamma^{Co} *_{2} \quad (5.7)$$

From Fig. 5.10, we saw that the non-radiative contribution from Co must be significantly larger than that of Ag, and hence irrespective of the other contributions from Co, the overall bandwidth for the AgCo nanoparticles should be larger than the pure Ag case. Therefore, the quality factor of the AgCo must be lower for given energy and volume in comparison to the pure Ag. However, as we saw from Fig. 5.9, the quality factor for the AgCo system can be comparable to or even larger than pure Ag for energies between 2.3 to 2.7 eV [Fig. 5.9 (b)] or volumes between 1 to  $2 \times 10^5 \text{ nm}^3$  [Fig. 5.9 (b)]. Clearly, this is not consistent with the predictions from eq. 5.7. A similar reasoning suggests that any effective medium approach based on describing the AgCo system with an effective dielectric function will also not yield quality factors comparable to Ag because a similar additive effect of the various damping mechanisms will result. In Fig. 5.10 (b), we show the calculation of the  $Q$  factor for Ag-Co spheres using the Mie theory and a dielectric function calculated using the effective medium model [159, 117, 133]. It is evident that the  $Q$  factor decreases from the pure Ag value for sizes with increasing Co content.

One way to understand the unusual behavior of the AgCo system is that the Co nanoparticle in contact with Ag modifies the radiative bandwidth of the Ag plasmonic nanoparticle. While such effects are known to occur in coupled pairs of molecules and nanoparticles with well defined absorption levels [183, 184], there is no prior evidence that it can occur in two contacted metallic nanoparticles with significantly different plasmonic character (Ag), i.e. one is strongly plasmonic while the other is not (Co). To estimate the change to the radiative component, we assumed that the AgCo behaves like a Ag nanoparticle and calculated the modified radiative BW by assuming the entire AgCo NP as pure Ag NP. After calculating the radiative BW, the non-radiative BW component was calculated as  $\Gamma_{1,NR}^{AgCo} = \Gamma^{AgCo} - \Gamma_{1,R}^{Ag}$ . The result of this analysis is shown in Fig. 5.14 for the CoAg. From this analysis the non-radiative loss is larger than the radiative contribution for energies beyond  $\sim 2.1$  eV and volume  $> 5.1 \times 10^5 \text{ nm}^3$ .

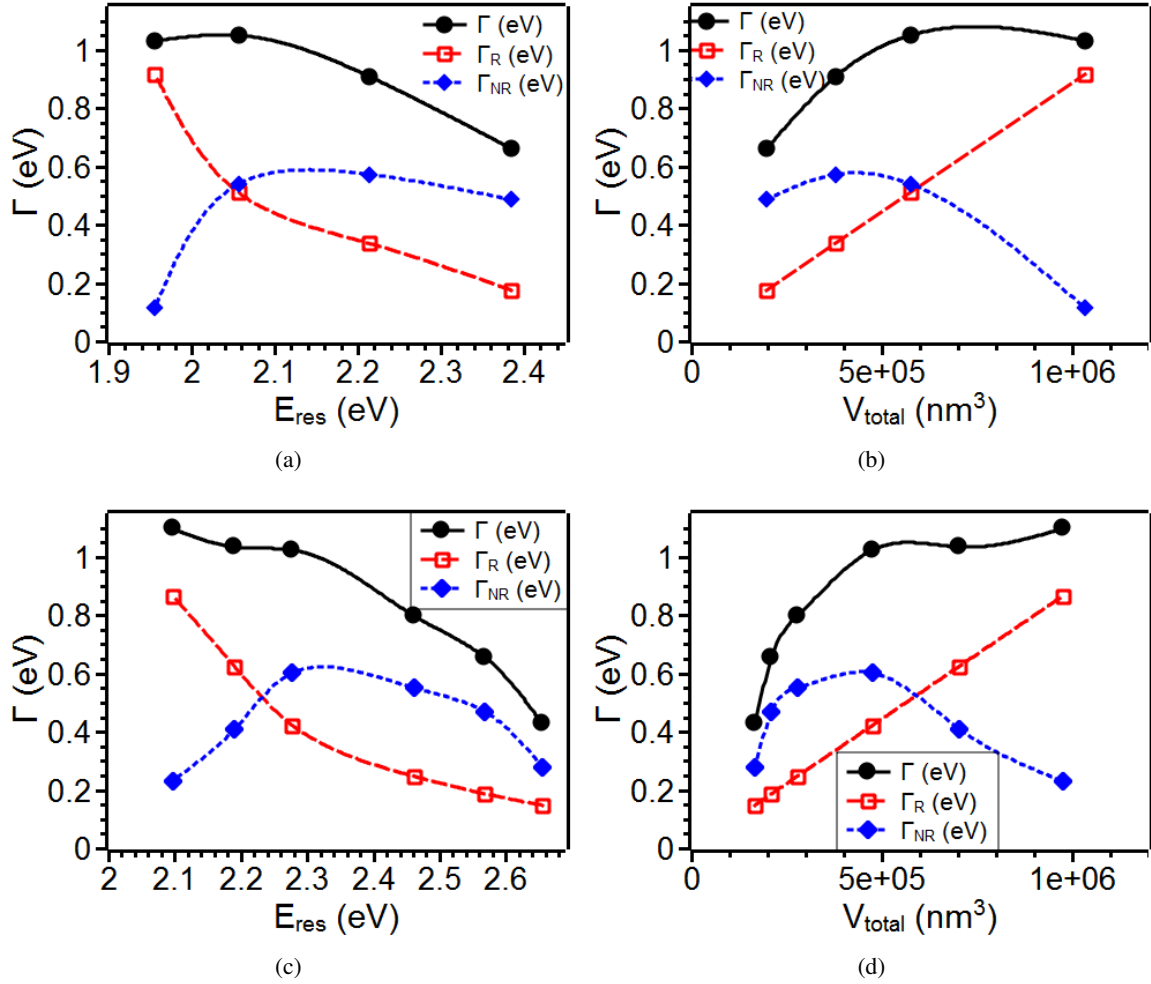


Figure 5.14: Radiative and non-radiative contributions to the total bandwidth of bimetallic NPs. (a) Energy dependence of bandwidth contributions for AgCo. (b) Volume dependence of the bandwidth contributions for AgCo (note log scale on x-axis). (c) Energy dependence of bandwidth contributions for CoAg. (d) Volume dependence of the bandwidth contributions for CoAg (note log scale on x-axis).



### 5.3.5 Quantum efficiency of plasmonic scattering from Ag and AgCo

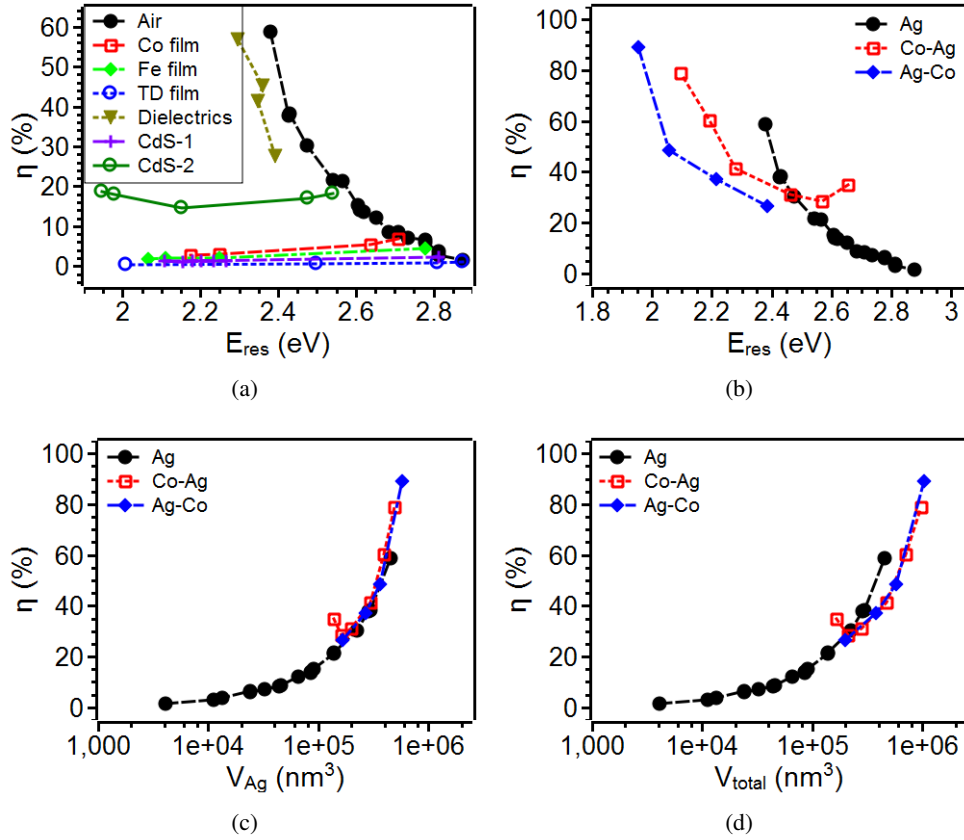


Figure 5.15: (a) Quantum Efficiency of Ag in different dielectric and lossy mediums. Quantum Efficiency of Ag and bimetal AgCo. (b) Energy dependence of  $\eta$ . (c) Variation of  $\eta$  with effective volume of Ag in the nanoparticle. (d) Variation of  $\eta$  with total volume of nanoparticle.

Since the individual contributions from radiative and non-radiative decays were estimated for the pure Ag and bimetallic AgCo systems, we were able to calculate the quantum efficiency for radiative energy transfer from the plasmonic system to its surrounding using as  $\eta = \frac{\Gamma_{IR}}{\Gamma_{IR} + \Gamma_{INR}}$ . In Fig. 5.15 (a) we have compared the quantum efficiency of Ag in different environments. The Ag NPs in dielectric medium does lose the quantum efficiency but in lossy mediums they tend to loose due to the dominance of the non-radiative component of the medium. Similarly, the quantum efficiency comparison of Ag to bimetal AgCo for various cases is shown in Fig. 5.15 (b-d). In Fig. 5.15(b) the variation with resonance energy showed that  $\eta$  for the bimetal was comparable to Ag and could also be larger than that of Ag for energies  $> 2.5$  eV. The volume dependent behaviors shown in Fig. 5.15(c) and (d) suggest that the bimetal systems can emulate the scattering efficiency of pure Ag nanoparticles.

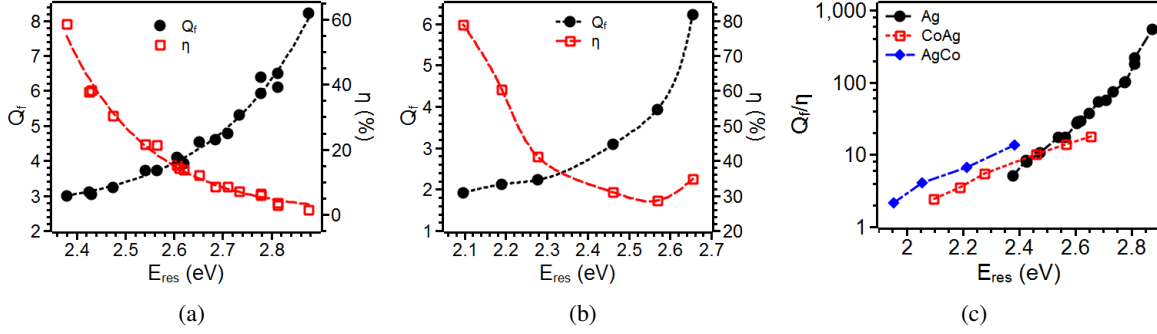


Figure 5.16:  $Q$  and  $\eta$  versus resonance energy for (a) pure Ag nanoparticles and (b) CoAg nanoparticles. (c) Comparison of the ratio  $Q/\eta$  versus resonance energy for the various pure Ag and bimetallic AgCo nanoparticles.

Since plasmonic applications require either optimizing the quality factor or the efficiency independently, such as for LSPR sensing or solar energy harvesting, we have compared the respective quantities in Fig. 5.16. The complementary behavior exhibited by  $Q$  and  $\eta$  implies that creating particle with higher energy resonances is preferred with radiative energy transfer is required. The benefit of making the bimetallic nanoparticles, as seen in Fig. 5.16(b) is that the quantum efficiency (or  $Q$  factor) can be enhanced over that of pure Ag at different energy positions thus broadening the energy regime for excellent plasmonic response. In Fig. 5.16(c) the ratio of  $Q/\eta$  is shown for the different cases and it is evident that the bimetal system can be used to tune this ratio in order to access values not feasible by pure Ag (within given constraints).

## 5.4 Conclusion

In this work, we have investigated the size and energy dependence of the plasmonic quality factor in hemispherical Ag and AgCo bimetallic NPs. The effect of different ambient environments such as insulating, semiconducting and metallic films on the Ag plasmon showed that the quality factor of the plasmons decreased with placing the Ag in these media. To ascertain the contribution from radiative and non-radiative effects we compared Ag hemispherical nanoparticles to triangular particles. From this the explicit dependence of size and volume on the radiative and non-radiative effects was estimated and the quantum efficiency was also calculated. Comparison with AgCo bimetallic systems with the quasi-static and effective medium models revealed that the AgCo bimetal system can significantly influence the radiative energy transfer from the plasmonic nanoparticles. This resulted in the bimetallic systems having comparable or better quality factor and or quantum efficiency to that of pure Ag in certain regimes of resonance energy and particle volume. These results demonstrate that the bimetal nanostructures provide a pathway to tune the quality factor and quantum efficiency of plasmonic processes.

## 5.5 Acknowledgment

The authors acknowledge support by the Army Research Office through Grant No. W911NF-13-1-0428. A portion of this research was conducted under Grant No. CNMS2013-284 at the Center for Nanophase

Materials Science, which is sponsored at ORNL by the Scientific User Facilities Division, Office of Basic Energy Sciences, U.S. Department of Energy. Humaira Taz helped in some of the NSL sample synthesis and SEM imaging. Mikayla Ehram and Jesse Goodwin created monolayer templates for NSL using the air-water interface technique which were then used for depositing metal film to create nanotriangles.

## Chapter 6

# From Mie to Fresnel through effective medium approximation with multipole contributions

(Reproduced with permission from Abhinav Malasi, Ramki Kalyanaraman and Hernando Garcia, *J. Optics*, **2014**, 16, 065001. Copyright 2015 IOP Publishing)

### 6.1 Summary

The Mie theory gives the exact solution to scattering from spherical particles while the Fresnel theory provides the solution to optical behavior of multilayer thin film structures. Often, the bridge between the two theories to explain the behavior of materials such as nanoparticles in a host dielectric matrix, is done by Effective Medium Approximation (EMA) models which exclusively rely on the dipolar response of the scattering objects. Here, we present a way to capture multipole effects using EMA. The effective complex dielectric function of the composite is derived using the Clausius-Mossotti relation and the multipole coefficients of the approximate Mie theory. The optical density of the dielectric slab is then calculated using the Fresnel approach. We have applied the resulting equation to predict the particle size dependent dipole and quadrupole behavior for spherical Ag nanoparticles embedded in glass matrix. This dielectric function contains the relevant properties of EMA and at the same time predicts the multipole contributions present in the single particle Mie model.

### 6.2 Theory

The most familiar form of EMA is the Clausius-Mossotti (CM) approximation where the system is described by an effective dielectric function  $\epsilon_{eff}$  given by

$$\frac{\epsilon_{eff}(\omega)}{\epsilon_h(\omega)} = 1 + \frac{\frac{n\alpha}{\epsilon_o}}{1 - \frac{n\alpha}{3\epsilon_o}} \quad (6.1)$$

where,  $n$  is the microscopic volume density of the number of spheres in the system,  $\alpha$  is the particle polarizability and  $\epsilon_h$  is the dielectric constant of the host. If only the dipole contribution is taken into account, the polarizability is given by

$$\alpha(\omega) = 4\pi\epsilon_0 r^3 \frac{\epsilon_i(\omega) - \epsilon_h(\omega)}{\epsilon_i(\omega) + 2\epsilon_h(\omega)} \quad (6.2)$$

where  $\epsilon_i$  is the dielectric constant of the inclusion and  $r$  is its radius.

On substituting Eq. 6.2 in Eq. 6.1, one gets the widely used Maxwell-Garnett approximation [185]. The CM approximation in the EMA is a consequence of considering that the randomly distributed dipoles and the induced dipole moment can be approximated as the mean induced dipole moment given by [186]

$$p_j = \frac{P(R_j)}{n(R_j)} \quad (6.3)$$

where  $P(R_j)$  is the macroscopic polarization of the system at location  $R_j$  and  $n(R_j)$  is the macroscopic density of the metal spheres at location  $R_j$ . If this approximation is used then the CM relation is rigorous.

As mentioned earlier, as the particle radius increases, quadrupole and higher order multipole contribution becomes important [3, 125], and the question arises as to how to incorporate these effects into EMA theories. Here, we propose to use CM equation in conjunction with Mie's solution. This will contain all the multipole contributions to the particle polarizability, thereby giving a multipole EMA for the dielectric function of a composite, such as nanoparticles embedded in a host medium. This will also provide us with a fundamental binary mixing rule that can be used consistently to obtain the effective dielectric constant of multicomponent systems, as done in Ref. [118].

There are several key aspects of EMA theories. The key fundamental definition of an effective dielectric function is that the local field effect should contribute to the total Hamiltonian of the system but should not by any means alter the causal nature of the material. Also, as the inclusion concentration tends to zero the behavior of the effective dielectric function should tend asymptotically to the dielectric function of the host, which obeys causality, and it must therefore be true that the effective dielectric function should follow the Kramers-Kronig relation [187].

The second and more deeper aspect of EMA is that for particles for which  $d/\lambda \geq 10^{-2}$ , light scattering becomes dominant and an EMA becomes irrelevant. When this happens the system, according to the generalized view, cannot be described by an effective dielectric function, it does not follow the laws of geometrical optics, and neither can it be described by the Fresnel equation [188]. But this aspect is more controversial, because if one performed a Gedanken experiment where a black box that contained the material is subjected to the excitation by an electromagnetic optical field, then the main question will be: is the spectral distribution of the input electromagnetic field collected at the output affected entirely by scattering or due to absorption? If we assume that the system follows Beer-Lambert law then the output intensity can be expressed as

$$I = I_0 e^{-\phi d} \quad (6.4)$$

where  $\phi$  is the absorption coefficient and  $d$  is the medium thickness. The absorption coefficient can be related to the imaginary part of an “effective dielectric” constant, and then, assuming that the system is causal, the real part of this effective dielectric function can be calculated. In fact one can go further to say that the system can be described by an effective dielectric constant that incorporates multipole expansion of Mie’s solution and at the same time can be used for multilayer systems in a Fresnel-type approach as follows. The optical density predicted by Mie, is given by

$$OD = \log \left( (1 - R_{eff})^2 e^{\sigma_{ext} \rho d} \right) \quad (6.5)$$

where,  $\rho$  is the particle density,  $\sigma_{ext}$  is the extinction coefficient,  $d$  is the sample thickness and  $R_{eff}$  is the reflection losses coming from the walls where the sample is contained. On the other hand, the optical density predicted by EMA is given by

$$OD = \log \left( (1 - R_{eff})^2 e^{\phi d} \right) \quad (6.6)$$

where, the absorption coefficient is given by

$$\phi = \frac{2\pi}{\lambda Re(\sqrt{\epsilon_{eff}})} Im(\epsilon_{eff}) \quad (6.7)$$

and the reflection coefficient by

$$R_{eff} = \frac{\left[ (Re(\sqrt{\epsilon_{eff}} - 1))^2 + (Im(\sqrt{\epsilon_{eff}}))^2 \right]}{\left[ (Re(\sqrt{\epsilon_{eff}} + 1))^2 + (Im(\sqrt{\epsilon_{eff}}))^2 \right]} \quad (6.8)$$

It is worth mentioning that the above equation can easily be extended to the case of oblique incidence and the results show perfect agreement with the Mie approach.

The suggestion we make here is that if both the equations predict the same spectral behavior then one must accept that the system can be described by an effective dielectric via Mie theory (that includes multipole expansions) and at the same time be applicable for multilayer systems in a Fresnel type approach.

To bridge the Mie, Fresnel and EMA, an effective polarizability is required which will contain the multipole expansion terms of the Mie theory. This can then be used in conjunction with CM to get the optical density of the relevant system. To achieve this, the concept of an effective polarizability was used in the context of CM equation by Barrera et al [189]. They were able to include local-field fluctuations in a system consisting of small spheres embedded in a dielectric medium and expressed the bare polarizability used in the CM by an effective polarizability. This polarizability is given by an algebraic equation that depends on the polarizability of the inclusion, the volume fraction and on the two particle distribution function [189]. It was also shown that the use of an effective polarizability can account for the effects of radiation-reaction, which is necessary for scattering. Further it was shown that on expansion of the effective polarizability, the first term accounted for the absorption while the second term accounted for scattering [102]. Our central hypothesis is therefore based on the main idea of a Gedanken experiment (the uncertainty in distinguishing between scattering and absorption when one only knows the input and output of the field)

and on the idea that an effective polarization can be defined such that it may be able to contain terms responsible for absorption and scattering [102] with the extinction cross-section given as:

$$\sigma_{ext} = \frac{k}{\epsilon_o} \text{Im}(\alpha_{eff}) \quad (6.9)$$

where,  $k = \frac{2\pi n_d}{\lambda}$ ,  $n_d$  is the refractive index of the medium and  $\lambda$  is the wavelength of light. As we show, while using  $\sigma_{ext}$  does the job adequately, using the absorption cross section instead of the extinction cross-section fails in two aspects; First, it does not obey causality because it ignores scattering, and second, it does not predict the same output as Mie theory [162].

To obtain the expression for the effective dielectric function we use the definition of the extinction cross section given by Eq. 6.9, where, for the Mie solution, the extinction coefficient can be expressed as:

$$\sigma_{ext} = \frac{2\pi r^2}{q^2} \text{Re} \left\{ \sum_{l=1} (2l+1) ({}^e a_l + {}^m b_l) \right\} \quad (6.10)$$

where,  $a$  and  $b$  correspond to the Mie coefficients and are given in terms of the Ricaty-Bessel cylindrical functions, and  $e$  and  $m$  correspond to the electric and magnetic multipole contributions, respectively. The  $l$  corresponds to the order of the contribution such that  $l = 1$  is the dipole, while  $l = 2$  corresponds to the quadrupole. The quadrupole contribution has a strong dependency on particle size and become important as the particle size increases. If  $z$  is a complex number then it is easy to say that

$$\text{Re}(z) = \text{Im}(iz) \quad (6.11)$$

Using the above relation, the extinction coefficient can be expressed as

$$\sigma_{ext} = \frac{2\pi r^2}{q^2} \text{Im} \left\{ \sum_{l=1} i(2l+1) ({}^e a_l + {}^m b_l) \right\} \quad (6.12)$$

On comparing Eqn's 6.9 and 6.12, the polarizability is given by:

$$\alpha = \frac{2\pi r^3 \epsilon_o}{q^3} \left\{ \sum_{l=1} i(2l+1) ({}^e a_l + {}^m b_l) \right\} \quad (6.13)$$

and using this expression, the effective dielectric function in the CM can be written as:

$$\epsilon_{eff} = \epsilon_h - \frac{\frac{3f\epsilon_h}{2q^3} \text{Im} \left\{ \sum_{l=1} i(2l+1) ({}^e a_l + {}^m b_l) \right\}}{1 + \frac{f}{2q^3} \text{Im} \left\{ \sum_{l=1} i(2l+1) ({}^e a_l + {}^m b_l) \right\}} \quad (6.14)$$

where,  $f$  is the volume fraction of the inclusion, and  $q$  is the size parameter defined below. In the cases where the particle radius is much smaller than the wavelength of the electromagnetic wave or that the size parameter  $q$  satisfies  $q = \frac{2\pi r n_h}{\lambda} \ll 1$ , then by using the power expansion of the cylindrical function (using terms of the leading order), it can be found that for the electric and magnetic dipole and quadrupole terms [125]:

$${}^e a_l = \frac{\Re_l^e}{\Re_l^e + i\Im_l^e} \quad (6.15)$$

$${}^m b_l = \frac{\Re_l^m}{\Re_l^m + i\Im_l^m} \quad (6.16)$$

where

$$\Re_l^e \approx q^{2l+1} \frac{(l+1)}{[(2l+1)!!]^2} n^l (n^2 - 1) \quad (6.17)$$

$$\Im_l^e \approx n^l \frac{l}{2l+1} \left[ n^2 + \frac{l+1}{l} - \frac{q^2}{2} (n^2 - 1) \left( \frac{n^2}{2l+3} + \frac{l+1}{l(2l-1)} \right) \right] \quad (6.18)$$

$$\Re_l^m \approx -\frac{nq^2}{2l+1} \Re_l^e \quad (6.19)$$

$$\Im_l^m \approx -n^{l+1} \left[ 1 + \frac{1-n^2}{2(2l+1)} q^2 \right] \quad (6.20)$$

and  $n = \frac{\varepsilon_i(\omega)}{\varepsilon_h}$ . Finally the effective dielectric function can be expressed as

$$\varepsilon_{eff} = \varepsilon_h - 3f\varepsilon_h \frac{3({}^e a_1 + {}^m b_1) + 5({}^e a_2 + {}^m b_2)}{2iq^3 + f(3({}^e a_1 + {}^m b_1) + 5({}^e a_2 + {}^m b_2))} \quad (6.21)$$

It is interesting to note that in the above equation when  $q$  is set to zero, the MG approximation is recovered. The above expression lacks symmetry in the sense that when  $f = 1$ , the dielectric function of the mixture is not equal to the dielectric function of the inclusion, and this asymmetry prevents it from being used as a bound. As mentioned earlier, this equation must obey causality. Therefore we have first calculated the real part of the dielectric function using the imaginary part predicted by the above equation for Ag nanoparticles (in a glass matrix). We have used the experimental values for the dielectric constant of Ag nanoparticles, suitably corrected for the modification of the relaxation time due to the small particle radius, as explained below. The method employed here is based on the approach of Bachrach and Brown [190], and is called the subtracted Kramers-Kronig relation, which can be derived assuming that one has an independent experimental point given by:

$$\text{Re}(\varepsilon(\omega_1)) = \frac{2}{\pi} P \int_0^\infty \frac{\omega' \text{Im}(\varepsilon(\omega_1))}{\omega'^2 - \omega_1^2} d\omega' \quad (6.22)$$

where  $\omega_1$  is a reference frequency. By subtracting this equation from the general form of the Kramer-Kronig relation we obtain the following relations:

$$\text{Re}(\varepsilon(\omega) - \varepsilon(\omega_1)) = \frac{2}{\pi} P \int_0^\infty \frac{\omega' \text{Im}(\varepsilon(\omega'))}{\omega'^2 - \omega^2} d\omega' - \frac{2}{\pi} P \int_0^\infty \frac{\omega' \text{Im}(\varepsilon(\omega'))}{\omega'^2 - \omega_1^2} d\omega'$$



$$\begin{aligned}
&= \frac{2}{\pi} P \int_0^\infty \frac{\omega' \text{Im}(\varepsilon(\omega')) (\omega'^2 - \omega_1^2) - \omega' \text{Im}(\varepsilon(\omega')) (\omega'^2 - \omega^2)}{(\omega'^2 - \omega^2) (\omega'^2 - \omega_1^2)} d\omega' \\
&= \frac{2}{\pi} P \int_0^\infty \frac{\omega' \text{Im}(\varepsilon(\omega')) (\omega^2 - \omega_1^2)}{(\omega'^2 - \omega^2) (\omega'^2 - \omega_1^2)} d\omega' = \frac{2}{\pi} (\omega^2 - \omega_1^2) P \int_0^\infty \frac{\omega' \text{Im}(\varepsilon(\omega'))}{(\omega'^2 - \omega^2) (\omega'^2 - \omega_1^2)} d\omega' \quad (6.23)
\end{aligned}$$

where,  $\varepsilon(\omega)$  is the complex dielectric function and  $\varepsilon(\omega_1)$  is a known value of the real part of the dielectric function. The  $P$  stands for the principal value of the integral. This equation is easier to implement and converges more rapidly than the standard Kramers-Kronig relation. It is used to reduce errors that are introduced in evaluating the integral over the whole range of frequencies when, experimentally, only a finite range of frequencies are accessible. The anchor or reference point in our calculation is given by a value calculated using Eq. 6.21. Using the effective dielectric function of the system in the above equation for particles of radius 10 nm and 100 nm, and a volume fraction  $f = 0.01$ , we calculated the real part of the dielectric function and compared it with the results predicted by the theory, as shown in Fig. 6.1. The result is remarkably good taking into account the fact that most of the values for the dielectric function of Ag above 4 eV and below 1 eV are extrapolated as a piecewise polynomial.

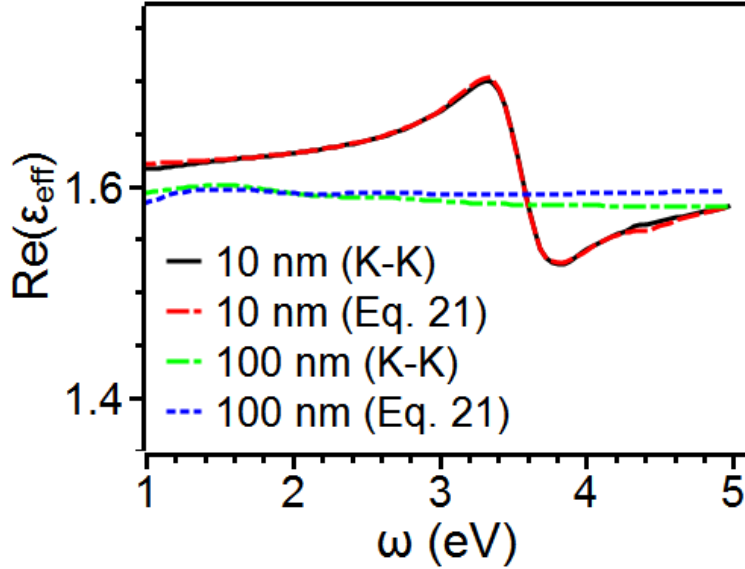


Figure 6.1: *Real part of the effective dielectric function for two different particle sizes, as predicted by K-K relation and by our theory result, Eq. 6.21.*

### 6.3 Results

In Fig. 6.2 we show the optical density (OD) as a function of wavelength, for the case of 10 and 100 nm radius Ag, respectively, using the most common approaches (MG, GH, and Mie theory) as well as Eq. 6.21 for a volume fraction of  $f = 0.01$  in glass. The dielectric function used in the calculation was corrected for the electron collision with the surface, which, in general, changes the scattering contribution from phonons, impurities, and defects with respect to the electron relaxation time. This correction can be incorporated in the analysis using the following expression [78]:

$$\varepsilon(\omega, r) = \varepsilon_{bulk}(\omega) + \omega_p^2 \left( \frac{1}{\omega^2 + \Gamma_\infty^{-2}} - \frac{1}{\omega^2 + \Gamma(r)^2} \right) + i \frac{\omega_p^2}{\omega} \left( \frac{\Gamma(r)}{\omega^2 + \Gamma(r)^2} - \frac{\Gamma_\infty^{-1}}{\omega^2 + \Gamma_\infty^{-2}} \right) \quad (6.24)$$

In the above equation  $\omega_p$  is the electron plasma frequency,  $\Gamma_\infty$  is the electron conductivity relaxation time, and  $\Gamma_r$  is given by

$$\Gamma(r) = \frac{1}{\Gamma_\infty} + A \frac{v_F}{r} \quad (6.25)$$

where,  $v_F$  is the Fermi velocity, and  $A$  is a constant of the  $O(1)$ , and for spheres,  $A \approx 1$  [191]. The refractive index for Ag was obtained from [192], while the additional information for Ag to be used in the subsequent calculations was taken from ref. [193], including  $\omega_p$  of 9.6 eV,  $\Gamma_\infty$  of  $2.89 \times 10^{-14}$  s and the  $v_F$  of  $1.39 \times 10^6$  m/s.

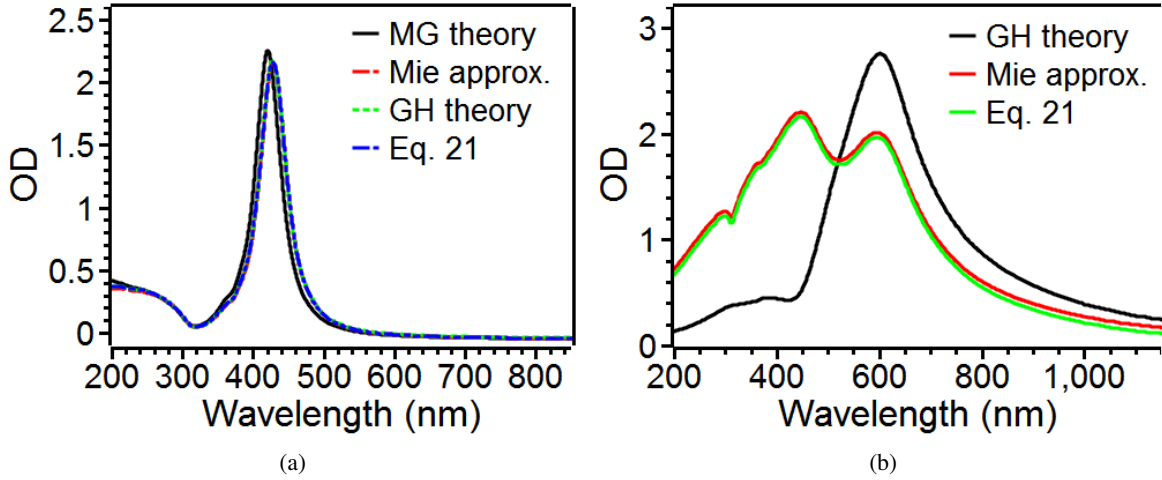


Figure 6.2: OD for a) 10 nm and b) 100 nm radius Ag nanoparticles embedded in glass matrix. The plots were calculated using the Maxwell-Garnett (MG), Gans-Happel (GH), and approximate Mie theories, as well as by our new theory, Eq. 6.21.

To compare the results, it was necessary to ensure consistency of the particle radius  $r$  with the volume fraction and volume density of particles ( $\rho$ ), which was estimated for  $f = 0.01$  to be:

$$r = \sqrt[3]{\frac{3f}{4\pi\rho}} \quad (6.26)$$

for values of  $\rho = 2387\mu m^{-3}$  for the 10 nm radius and  $\rho = 2.387\mu m^{-3}$  for the 100 nm radius particles.

In an attempt to incorporate the full Mie theory in an EMA scheme and obtain an effective dielectric function, Gans and Happel (GH) [194] incorporated electric dipole and quadrupole as well as magnetic dipole and quadrupole contributions in a single expression, using the full Mie coefficients. In Fig. 6.2, we have compared their results with predictions of the optical density using the MG approach, GH result, approximate Mie solution from Ref. [125], and our Eq. 6.21 for the two different particle sizes. It is quite evident that our result gives remarkably similar results to the Mie, and Gans & Happel approaches. From Fig. 6.2(b), it can be seen that Eq. 6.21 predicts the quadrupole and dipole more accurately than predicted by GH approach. The GH approach does not predict the absorbance in accordance with the Mie theory and shows a highly damped behavior for the quadrupole mode. The results of Fig. 6.2 indicate that the effective dielectric function in our model, given by Eq. 6.21, is quite accurate and its use within the EMA model accurately predicts higher order plasmonic modes for various particle sizes.

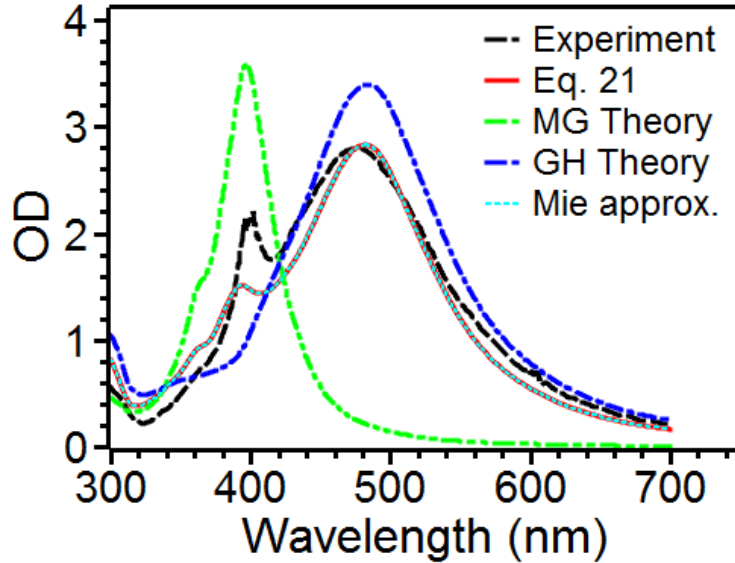


Figure 6.3: Comparison of our theoretical prediction based on Eq. 6.21 (solid red curve) to the experimental measurement (dashed black curve) of OD of nanoparticles of Ag with average size of 40 nm embedded in a glass matrix (experimental data was taken from Ref. [78]). Results of the MG theory (green dashed curve, scaled by a factor of 0.5), GH (dark blue dashed curve), and Mie (light blue dashed curve) theories are also shown. Our new EMA theory result of Eq. 6.21 overlays the Mie theory result very well, while predicting both the dipole and quadrupole peaks.

In Fig. 6.3 we have compared the optical density of experimental data extracted from Ref. [78] for a composite made from Ag clusters embedded in a glass matrix. The clusters have an average size centered around 40 nm, but their volume fraction and the medium thickness was not provided. We have utilized Eq.

6.21 to obtain a theoretical prediction based on a best fit to the experimental data. The free parameters in the fit were the particle radius, the volume fraction, and the thickness of the composite. In Fig. 6.3, the Eq. 6.21 result is for an average radius of 42.31 nm, with a volume fraction of 0.003046 in a glass matrix of dielectric function equal to 2.0, propagating through a composite of thickness 6.83  $\mu\text{m}$ . We have also included the results from the various other theories, including Mie, GH, and MG. The MG theory curve (scaled by a factor of 0.5) only predicts the dipole peak contribution of the system and is way off from the experimental value. While the Mie and GH theory predict the dipole peak accurately, the quadrupole peak is only predicted by Mie. More interestingly, the prediction of our Eq. 6.21 overlays the Mie result very well. In addition, our theory is in excellent agreement with experiment, despite incomplete information on details of the material provided in Ref. [78].

In Fig. 6.4(a), we show the resonance wavelength for the dipole and the quadrupole as a function of particle radius calculated using Eq. 6.21 for the system studied in Fig. 6.3. We observed that the red shift of the quadrupole resonance is less dramatic as compared to the dipole resonance. In Fig. 6.4(b), the OD curves for Ag nanoparticles embedded in glass matrix of different average size are compared to show that our model can easily capture the plasmon modes and can also show the changing intensity of the plasmon mode as a function of size.

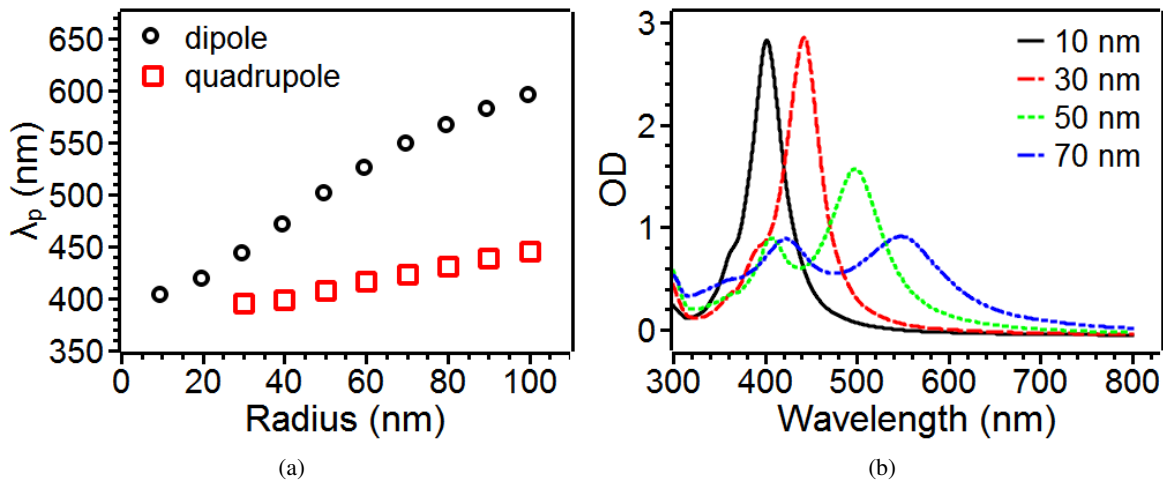


Figure 6.4: *a) The resonance wavelength of the dipole (open circles) and quadrupole (open squares) excitation of Ag nanoparticles embedded in glass as a function of the particle radius calculated using Eq. 6.21. b) Plot of the absorption curves generated for Ag nanoparticles of different radius embedded in glass matrix.*

## 6.4 Limitations of the Model

The first limitation of the model is its inability to predict the phenomenon of percolation threshold that is common in effective medium theories of the Bruggeman type [195], and in extended Maxwell-Garnett approximations [196, 197]. This is due to the fact that in our present case the role of the inclusion and the role of the host are not symmetric. In other words, the complementary mixture that results in the exchange

of the host and the inclusion and at the same time exchanging their volume fraction is not possible in our model. In our opinion, it is not a major limitation in the sense that the model was derived in the spirit of low volume fraction. What we would like to focus now is on identifying the criteria for the applicability of Eq. 6.21, which is given in detail by Mackay & Lakhtakia [198] where they studied the applicability of Lewin's homogenization formula. They raised three objections to the applicability of a homogenization theory.

a) *The inclusion should be small relative to the wavelength in the host material as well as in the inclusion material.* In this regard we believe that this restriction must be implemented with caution because the theory resides in incorporating higher multipole terms in the expression, and the higher resonance is what we are after. In the particular approximation that we used in the paper, we retained up to the quadrupole term, but we can include more terms in the expression and reproduce the multipole resonances pointed out by this restriction. This restriction is already implemented in Mie's approximation.

b) *If the conditions  $Re\{\epsilon_i\}Re\{\epsilon_h\} < 0$  and  $Im\{\epsilon_i\} \ll Re\{\epsilon_i\}$  are satisfied, then it is inappropriate for arbitrary values of the volume fraction.* This is more demanding because it can easily be satisfied by typical noble metals used commonly in plasmonic applications. However, we have argued that the strong resonances that appear as a function of volume fraction tend to happen in the large inclusion concentration and for large negative values of the dielectric function. In fact for typical values of  $Ag$ , these resonance tend to appear in volume fraction greater than 0.5.

c) *The restriction on the volume fraction is related to the size parameter  $q$  of the model.* As was mentioned earlier, the phenomenon of percolation can be predicted by the Bruggeman formalism where the inclusion and the host are on equal footing. This is not the case in our present work. One interesting aspect of the Eq. 6.21, is that if the second term in the denominator is ignored, we recovered Foldy's result. This is achieved by assuming that the propagation constant in its formulation can be identified to be related to an effective dielectric function of the mixture and the extinction cross section is given by Mie's result. Phenomenologically we have found that the agreement with Mie's results at normal incidence is correlated to the size parameter and the volume fraction such that

$$\frac{f}{q^3} = \left(\frac{\lambda}{n}\right)^3 \frac{\rho}{6\pi^2} < 1$$

Or using the density of modes on an electromagnetic wave in k-space given by [199]:

$$\rho_k = \frac{8\pi n^3}{3\lambda^3}$$

Then the restriction can be written as

$$\frac{\rho}{\rho_k} < 2\pi$$

This condition implies that the volume occupied by one particle in the host must be smaller by the volume occupied by the mode of the electromagnetic field in k-space. This restriction will determine the particle density which in turn will determine the volume fraction and the particle radius through Eq. 6.26. The estimated values for particles of the order of 20 nm at  $\lambda \approx 800$  nm have volume fraction of the order of

$f = 0.02$ , while for particle of 80 nm radius at  $\lambda \approx 800$  nm the volume fraction is of the order of  $f = 0.2$ . Of course, the restriction of percolation must be taken into account such that in general  $f < 0.3$ .

*In this chapter we bridged the Mie theory and the Fresnel equation using the EMA model to incorporate the contributions of multipolar resonances.*

## **6.5 Acknowledgement**

HG acknowledges support by the NSF through grant CMMI-0757547 while RK acknowledges support by grants ARO grant W911NF-13-1-0428, and NSF EPS-1004083. HG also acknowledges support by the Fullbright program for international exchange. RK and AM also acknowledge support by the Sustainable Energy Education and Research Center and Center for Materials Processing.

## Chapter 7

# Novel Iron-based ternary amorphous oxide semiconductor with very high transparency, electronic conductivity, and mobility

(Reproduced with permission from Abhinav Malasi, Humaira Taz, Annette Farah, Maulik Patel, Benjamin Lawrie, Raphael Pooser, Arthur Baddorf, Gerd Duscher and Ramki Kalyanaraman, *Scientific Reports*, **2015**, accepted. Copyright 2015 Nature Publishing Group)

### 7.1 Summary

Here we report that ternary metal oxides of type  $(\text{Me})_2\text{O}_3$  with the primary metal (Me) constituent being Fe (66%) along with the two Lanthanide elements Tb (10%) and Dy (24%) can show excellent semiconducting transport properties. Thin films prepared by pulsed laser deposition at room temperature followed by ambient oxidation showed very high electronic conductivity ( $> 5 \times 10^4$  S/m) and Hall mobility ( $> 30$   $\text{cm}^2/\text{V}\cdot\text{s}$ ). These films had an amorphous microstructure which was stable to at least  $500^\circ\text{C}$  and large optical transparency with a direct band gap of  $2.85 \pm 0.14$  eV. This material shows emergent semiconducting behavior with significantly higher conductivity and mobility than the constituent insulating oxides. Since these results demonstrate a new way to modify the behaviors of transition metal oxides made from unfilled d- and/or f-subshells, a new class of functional transparent conducting oxide materials could be envisioned.

### 7.2 Results

Our investigations were motivated by the study of the magneto-optical properties of the giant magnetoresistive material terfenol-D [metal composition of Fe(65.7%):Tb(10.3%):Dy(24%)] for applications in optical sensing and computing. Films of thickness from 9 to 37 nm were deposited by the pulsed laser deposition (PLD) technique onto quartz substrates under high vacuum conditions ( $\sim 5 \times 10^{-8}$  Torr base pressure) at room temperature. However, instead of a metallic sheen, these films showed optical transparency in their as-

prepared (AP) state, as shown in Fig. 7.1(a) for the sample labeled AP. This transparency was quantitatively evaluated as a function of film thickness by transmission spectroscopy. The dashed curves in Fig. 7.1(b) show that the as-prepared films had a coefficient of transmission (T) of >50% in a energy range spanning the UV to NIR (1.5 to 4 eV) and could reach as high as T >90% for the thinner films (9 nm thickness). We confirmed that this high transparency was not due to a discontinuous film morphology. Fig. 7.1(c) and (d) show a scanning electron microscope image and an atomic force microscope image of the 25 nm thick as-prepared films, respectively. The films were continuous with a random distribution of nanoparticles typical of the PLD process. The root mean square surface roughness of the film in the particulate free regions was estimated to be between 1 to 2 nm, depending on the film thickness [Fig. 7.2(c-inset)], as ascertained from the atomic force microscopy measurements. To further understand this optical transparency, we estimated the absorption coefficient ( $\alpha$ ) from  $\alpha = -\ln(T)/L$ , where L is the film thickness and then generated the dependence of  $(\alpha hv)^{1/m}$  versus  $hv$ , which represents the photon energy as the product of Planck's constant ( $h$ ) and photon frequency  $\nu$ , while  $m$  represents the type of absorption. This Tauc plot is shown in Fig. 7.1(e) for the case  $m = 1/2$ , i.e. for a direct allowed transition for the films of 25 nm thickness (as-prepared is dashed curve). The rapid change in the slope of the curve indicates large interband absorption and extrapolating this linear region permitted estimation of the direct allowed energy band gap  $E_g^d$ . We found that the as-prepared film of L = 25 nm film had a  $E_g^d$  of 2.82 eV. Similar analysis of the other as-prepared films (see supplemental material) yielded values between 2.72 and 3.0 eV, as shown in the inset of Fig. 7.1(e), giving an average direct band gap of  $2.85 \pm 0.14$  eV. No evidence for an in-direct gap could be found from a similar Tauc plot analysis.

The optical data suggested that the films were very likely oxidizing rapidly upon exposure to air since the transparency was not consistent with forming metallic films (for comparison, films of metals like Au, Ag, Cu, Fe etc. achieve such high transmission at thicknesses of only a few nm). We further modified the oxidation state of the films by a high temperature anneal (500°C for 2 hours) in either a N<sub>2</sub>- rich or O<sub>2</sub>-rich environment (air). The optical photograph in Fig. 7.1(a) shows that the transparency increased following annealing of 25 nm thick films (i.e. optical images marked as N<sub>2</sub> and O<sub>2</sub> corresponding to the N<sub>2</sub> and O<sub>2</sub> annealing). The qualitative increase was also evident from the optical transmission curves [Fig. 7.1(b), solid curves] for the annealed films in comparison to the as-prepared film. The Tauc plot analysis of the annealed samples [Fig. 7.1(e, solid lines)] yielded  $E_g^d \sim 2.89$  and 2.82 eV for the N<sub>2</sub> and O<sub>2</sub> samples respectively. These estimated band gap values were within the measurement uncertainty of the average value estimated for the as-prepared films, as seen in the inset of Fig. 7.1(e), implying that the high temperature anneal did not significantly influence the microstructure of the films. The optical behavior of the as-prepared and thermally annealed films pointed to an oxidized film that behaved like a semiconductor and one whose band gap was unchanged upon annealing to high temperatures.



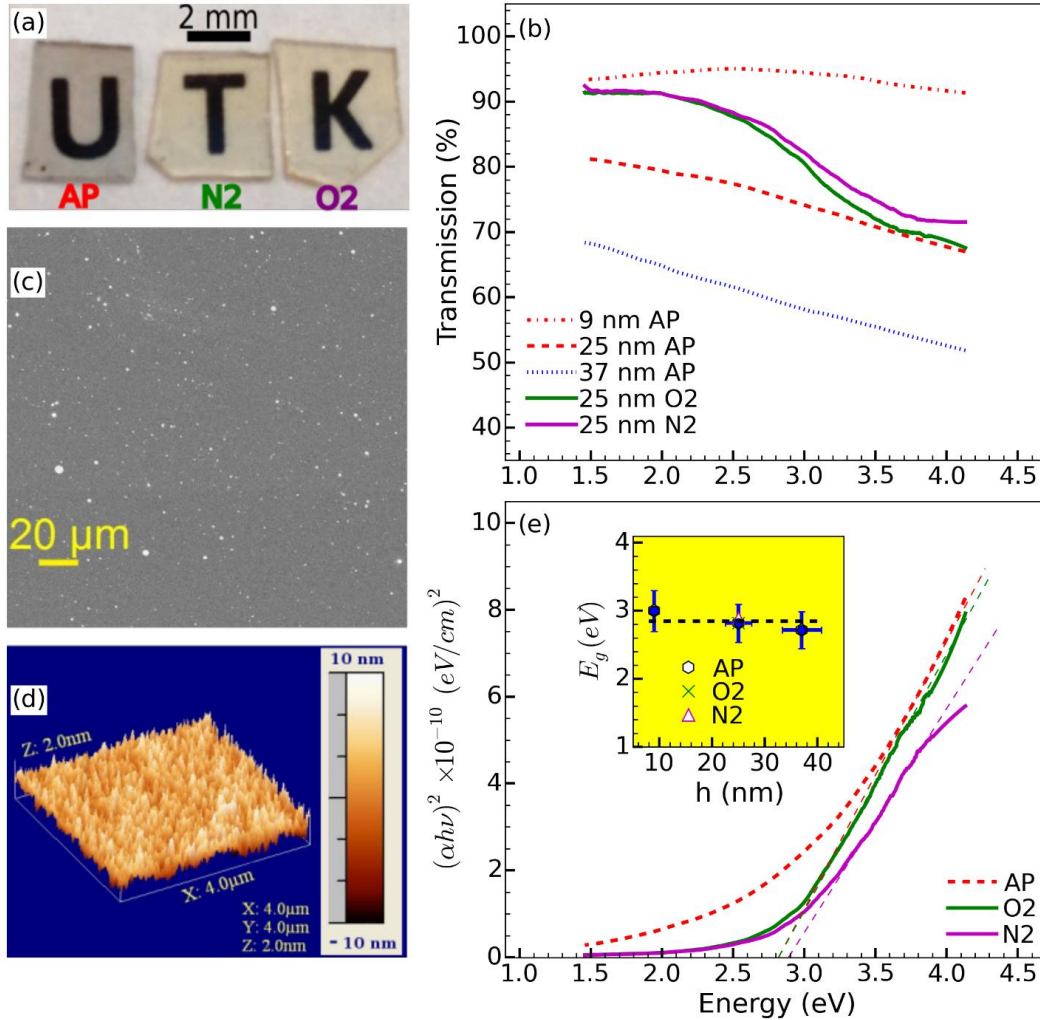


Figure 7.1: (a) Optical photograph of lettered blocks showing the large transparency of 25 nm thick films in as-prepared state (marked as AP), and following annealing in nitrogen (marked as N2) and oxygen (marked as O2) at 500°C for 2 hrs. (b) Optical energy (and wavelength) dependent transmission of as-prepared films with thickness between 9 to 37 nm (dashed curves) and following annealing of the 25 nm film solid curves). (c-d) SEM (c) and AFM (d) information from a 25 nm as-prepared film respectively. (d) Tauc plot comparing the direct optical absorption in 25 nm films (as prepared is dashed line while annealed are solid lines). The extrapolations from the strongly absorbing linear regimes are shown and were used to estimate the band gap. Inset shows the Tauc direct band gap values as a function of thickness of the as-prepared films and following annealing of the 25 nm film. A line corresponding to the average band gap value from measurements of various as-prepared films is also shown in the inset.

To understand the origin of this semiconducting behavior, we performed a detailed study of the structure and chemical composition of the as-prepared and O<sub>2</sub> annealed films. Glancing incidence X-ray diffraction (GIXRD) from the target material used for the PLD process showed peaks corresponding to polycrystalline terfenol-D. However, the as-prepared films were featureless, indicating an amorphous microstructure, and remained so even following the 500°C thermal treatments (see supplemental material). We next prepared films by PLD onto ultrathin membranes (C or Si<sub>3</sub>N<sub>4</sub>) for evaluation by transmission electron microscopy (TEM). Fig. 7.2(a) shows that the typical microstructure of as-prepared films was amorphous, confirmed by the TEM diffraction pattern shown in the inset. A similar amorphous microstructure was evident for the 500°C O<sub>2</sub> annealed films (shown in supplemental material). Therefore, the TEM results along with the GIXRD observation independently established that the as-prepared and 500°C O<sub>2</sub> annealed films were amorphous. The chemical constituents, homogeneity, and composition of the films were measured by two different approaches: core-loss electron energy loss spectroscopy (EELS) in the TEM was used to obtain the film volume averaged information while X-ray photoelectron spectroscopy (XPS) was used to analyze the film surface. From the core loss peak positions only four elements were detected, the three metals (Fe, Tb, Dy) and O. Fig. 7.2(b) compares the core-loss spectrum for as-prepared (dashed line) and O<sub>2</sub> annealed (solid line) films for the energy window containing Fe and O, while Fig. 7.2(c) is for the energy window containing Tb and Dy. Quantitative analysis of the core-loss peak intensities established that the as-prepared films were metal oxides with a metallic composition of Me=Fe(66%):Tb(10%):Dy(24%) and a metal to oxygen ratio of 2:3 with an inherent error of ~10% (<4% error on the individual elemental concentrations). The composition of the as-prepared film could therefore be expressed as Me<sub>2</sub>O<sub>3-x</sub>. The composition was found to be very homogeneous in its metal and oxygen concentration, with no evidence for any chemical segregation effects throughout the film. Similar analysis of the O<sub>2</sub> annealed film gave an identical metal composition and a more fully oxygenated metal oxide Me<sub>2</sub>O<sub>3</sub>, consistent with a Fe to O ratio found in Fe<sub>2</sub>O<sub>3</sub> EELS standards. From these measurements it was also clear that only the state of Fe changed upon O<sub>2</sub> annealing while the Tb and Dy oxidation states did not change. XPS survey scans from the surface of the as-prepared and O<sub>2</sub> annealed film (see supplemental material) yielded similar results in terms of the constituents present, i.e. the three metals and oxygen. A carbon peak was also detected and attributed to hydrocarbon contamination following exposure to atmosphere. Fig. 7.2(d) shows the XPS spectra of the Fe 2p signal, which can be used to differentiate between metallic Fe and its various oxidized states. The as-prepared film (dashed line) showed the Fe to be predominantly in Fe<sup>3+</sup> oxidation state, as evidenced by the satellite peak near 718.8 eV (marked as Fe<sup>3+</sup> on Fig. (d) and is the known position for the Fe<sup>3+</sup> oxidation state in pure Fe<sub>2</sub>O<sub>3</sub> [200]). Since the satellite position was shifted to slightly lower energies than in pure Fe<sub>2</sub>O<sub>3</sub>, some contribution from a lower oxidation state, such as Fe<sup>2+</sup>, was also evident. A small peak at 707.4 eV for the as-prepared film also indicated the presence of Fe<sup>0</sup> [marked on Fig. (d)]. However, this unoxidized iron appeared to be discontinuously distributed on the film surface as TEM-EELS measurements did not detect any Fe<sup>0</sup> in the film regions but only showed evidence for it within the PLD particulates. This was evidenced by the EELS spectra from the particulates, shown by the dotted line in Fig. 7.2(b), in which no oxygen O<sub>K</sub> peak was evident, implying that the iron was in metallic state in the particulates. Upon oxygen annealing, the intensity of the oxide peaks increased significantly while the metallic Fe peak disappeared, as

seen in Fig. 7.2(d, dashed curve). The position of the satellite peak was closer to  $Fe^{3+}$  (as seen in  $Fe_2O_3$ ) indicating that it was the primary oxidation state. The increase in oxygen concentration following annealing was also evidenced from XPS O 1s spectra [Fig. 7.2(e)] and corroborated the TEM results. In Fig. 7.2(f) and (g), the normalized XPS spectra corresponding to Tb 3d 5/2 and Dy 3d 5/2 levels, respectively, are shown for as-prepared (solid line) and  $O_2$  annealed cases (dashed line). The energy positions of these peaks were correlated very well with the signals from the respective oxides of the form  $Tb_2O_3$  (which occurs at 1241.4 eV) and  $Dy_2O_3$  (which occurs at 1298.9 eV) [201] (and are indicated on the figure). Further, the XPS peak positions were unchanged between the as-prepared and annealing case suggesting that the oxidation state of the Lanthanide metals did not change upon annealing. In totality, these findings pointed to amorphous films in which the amount of O and  $Fe^{3+}$  increased in going from the as-prepared to the  $O_2$  annealed films, but without change in the oxidation state of the Lanthanide metals. The formation of an amorphous oxide film is not entirely surprising and we attribute it to the combination of forming an amorphous microstructure during the PLD process followed by its instantaneous oxidation upon exposure to air. Previous works focused on the magnetic behaviors of similar compounds (Fe-Tb-Dy) have shown that it is possible to synthesize amorphous metallic films by techniques such as sputtering [202, 203]. Also, the surfaces of such compounds have been reported to oxidize fairly quickly in air leading to an oxide layer of thickness between 10 to 30 nm, while the bulk material continues to oxidize at a much slower rate, thus necessitating a capping layer to prevent degradation.

Given the importance of transparent amorphous oxides to the electronics industry, we investigated the electrical properties of these films. Conductivity ( $\sigma$ ) and Hall mobility ( $\mu_H$ ) measurements were made using the 4-probe van der Pauw geometry for films between 9 and 74 nm in thickness deposited onto  $SiO_2/Si$  substrates (i.e. Si containing a 400 nm thermally grown oxide layer). First we verified the nature of electrical conduction in these films by performing temperature-dependent conductivity measurements. As shown for a 25 nm as-prepared film in the inset of Fig. 7.3(a), the electronic transport confirmed a semiconductor-type material since the conductivity increased exponentially with temperature T. This result also ruled out any role of the discontinuously distributed metallic iron on the film surface in playing a role on the electronic properties. Fig. 7.3(a) shows the room temperature conductivity for as-prepared films with various thickness. The measured conductivity ranged from  $\sim 5 \times 10^3$  to  $5 \times 10^4$  S/m. These values are many orders of magnitude higher than that found in the constituent metal oxides noted in the previous section [204, 205]. To understand the origin of the large conductivity (and its change with thickness), we measured the Hall mobility since it contributes directly to  $\sigma$  through the expression  $\sigma = \mu_H n e$ , where  $n$  is the carrier concentration, and  $e$  is the magnitude of electron charge. Fig. 7.3(b) shows that the Hall mobility had a negative sign for all the as-prepared films studied, indicating an n-type semiconductor. Since its magnitude was relatively unchanged it could not be responsible for the drop in conductivity with increasing thickness L. However, the measured value of  $32 \pm 4$   $cm^2/V\cdot s$  (averaged over the various as prepared films) was extraordinarily high, and comparable to the best known s-band amorphous oxide materials [135]. We were unable to detect any evidence for room temperature magnetism through hysteresis, coercivity or saturation behavior (see supplemental material), consistent with the fact that oxidation destroys magnetism in such alloys [203]. This also confirmed that the measured mobility was the *regular* hall mobility and therefore was directly contributing

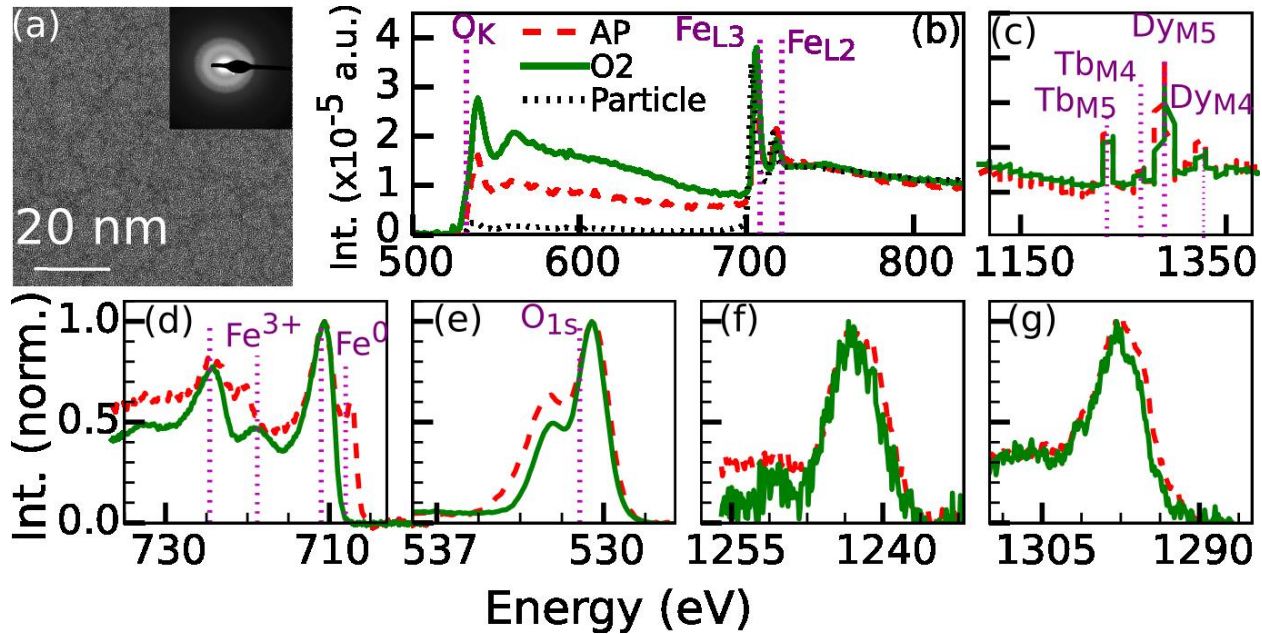


Figure 7.2: (a) Amorphous microstructure of the as-prepared films was evidenced by TEM imaging and selected area diffraction (inset). (b-c) EELS analysis of the as-prepared and O<sub>2</sub> annealed films only detected Fe, and O (Fig. c) and Tb and Dy (Fig. d). In Fig. (b) the EELS spectrum from a PLD nanoparticle is also shown by dotted curve. (d-g) XPS measurements showing the various detected components in the as-prepared vs O<sub>2</sub> annealed films. (d) Fe 2p signal (e) O 1s signal. (f) Tb 3d 5/2 signal, (g) Dy 3d 5/2 signal. In figures b-g, the as-prepared (AP) films are shown by dashed curves while the O<sub>2</sub> (O<sub>2</sub>) annealed films are shown by solid curves. The vertical dotted lines mark the position of the various absorption edges (EELS) and peaks (XPS) as indicated. The additional vertical lines in Fig. (d) correspond to the additional Fe<sub>3d</sub> absorption peaks found in the hematite and magnetite form or iron oxides.

to the high electrical conductivity. The unchanging mobility with thickness implied that the change in conductivity with thickness was due to a change in the free carrier concentration, which was estimated from  $n = \frac{\sigma}{\mu_{He}}$  and is shown in Fig. 7.3(c). The values decreased from  $9.4 \times 10^{19}$  to  $1.15 \times 10^{19}$  cm<sup>-3</sup> for the 9 to 74 nm films respectively. While such an effect has been reported before for ultrathin semiconducting films [206], we speculate that the change in conduction could be partly attributed to the increase in surface roughness observed with increasing thickness of the films, as shown in the inset of Fig. 7.3(c).

The transport behavior following thermal treatments up to 500°C was measured for 25 nm thick films. Fig. 7.3(d) shows that while the conductivity of the film decreased following the annealing, the magnitude of the drop was very different,  $\sim 3\times$  decrease for the N<sub>2</sub> case vs  $\sim 17\times$  for the O<sub>2</sub> case. To understand this change, the hall mobility was also measured, and, as shown in Fig. 7.3(b) n-type conductivity was observed in all cases, but the magnitude decreased from 35.4 cm<sup>2</sup>/V-s (for the as-prepared film) to 12 cm<sup>2</sup>/V-s for the N<sub>2</sub> anneal and 2.2 cm<sup>2</sup>/V-s for the O<sub>2</sub> case, which correlated very well with the magnitudes of the drop in conductivity shown in Fig. 7.3(d). Despite the changes following thermal annealing, the combination of conductivity and mobility observed in these as-prepared and thermally treated films was still orders of magnitude higher than in the component oxides (Fe<sub>2</sub>O<sub>3</sub>, Tb<sub>2</sub>O<sub>3</sub>, and Dy<sub>2</sub>O<sub>3</sub>) as we discuss next. These annealing results also hinted at a potential future path to control and modify the electronic and optical

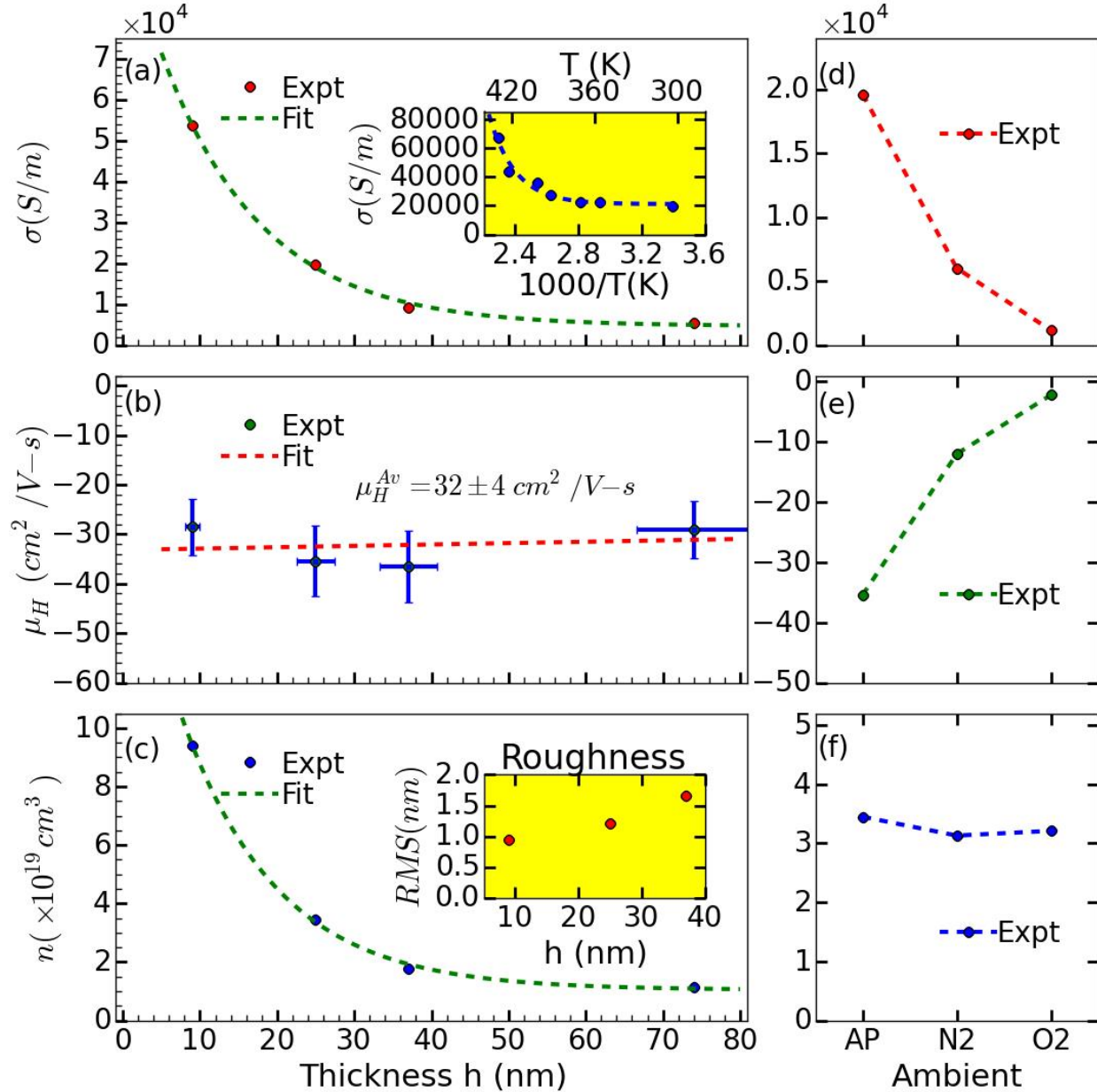


Figure 7.3: Transport properties of the as-prepared (a-c) and annealed films (d-f). (a) Dependence of conductivity on thickness of as-prepared films. Inset shows that the conductivity  $\sigma$  increased exponentially with temperature for a 25 nm as-prepared film. (b) The mobility of the as-prepared films showed n-type conductivity and its magnitude was relatively unchanged with thickness yielding an average value of  $32 \pm 4 \text{ cm}^2/\text{V-s}$ . (c) The electron carrier concentration in the as-prepared films decreased exponentially with increasing film thickness. This correlated with an increased surface roughness of the films (inset). (d) Conductivity change for 25 nm films following annealing in nitrogen ( $\text{N}_2$ ) or oxygen ( $\text{O}_2$ ) at  $500^\circ\text{C}$  for 2 hrs. (e) Mobility change with annealing. (f) Carrier concentration remained relatively unchanged following annealing. In figures d-f, the as-prepared films are indicated as AP while the  $\text{O}_2$  and  $\text{N}_2$  annealed films are marked as O2 and N2 respectively. The dashed lines in (a-c) correspond to best fits to the experimental data. The dashed lines in (d-f) correspond to guides to the eye.

properties of this material.

### 7.3 Discussion and conclusion

Based on the substantial knowledge developed over the past decade, it is possible to summarize two common features found in all the ternary amorphous oxides that show high mobility ( $>10 \text{ cm}^2/\text{V}\cdot\text{s}$ ), such as the a-IGZO system. First, overlap of the large spherically symmetric *ns* levels involved in the metal cation bonding produces large s-conduction band curvature and consequently, a high mobility for carriers excited from the valence band formed by oxygen 2p states [140, 142]. Second, the ternary oxide cannot have a mobility and/or conductivity far exceeding that of *all* of its constituent oxides, as exemplified by the relation between the ternary composition and the measured mobility values [135, 143]. In fact, it can be stated that the primary reason to use a ternary system is to stabilize the amorphous microstructure.

Based on the dominant metal oxidation states measured by XPS investigations, it is tempting to interpret our observed optical and electronic behaviors in the above context, i.e. as arising from a mixture of the different semiconducting sesquioxides (i.e.  $\text{Fe}_2\text{O}_3$ ,  $\text{Tb}_2\text{O}_3$  and  $\text{Dy}_2\text{O}_3$ ). But, all of these oxides are well-known insulators with no contribution from the s-band to their conductivity and mobility behaviors [207]. Semiconducting iron oxide (hematite or  $\alpha - \text{Fe}_2\text{O}_3$ ) is a charge transfer insulator in which the indirect optical band gap of 2.1 eV excites electrons from a valence band which is primarily from the oxygen 2p levels into a conduction band which comes from the Fe 5d levels. In the band structure model, the extremely flat d-band (i.e. low curvature) results in very heavy electrons and the resulting low conductivity and mobility of  $<0.01 \text{ cm}^2/\text{V}\cdot\text{s}$  [208]. Despite attempts to dope iron oxide, the best conductivity and mobility still remains at  $\sim 4 \text{ S/m}$  and  $<0.6 \text{ cm}^2/\text{V}\cdot\text{s}$  respectively in high-quality crystalline thin films [204], orders of magnitude lower than the values observed here for the as-prepared and thermally annealed amorphous films. The low mobility has also been explained as the consequence of conduction by polaron hopping, with polarons having a very large effective mass due to the strong interaction between electrons and the lattice in such ionic crystals [209]. The Lanthanide oxides are materials with potential applications as high-K dielectrics because of their electrically insulating nature and large band gaps [210, 205]. These oxides also have valence band showing primarily O 2p character and conduction band coming from the 5d levels. However, their unique feature is that the 4f levels can introduce filled and/or empty states at different positions with respect to the optical band-gap [211]. Nevertheless, the extremely flat nature of the f-levels as well as the d-conduction band again results in exceedingly low room temperature conductivity ( $< 10^{-12} \text{ S/m}$ ) and electron mobility values ( $<2 \text{ cm}^2/\text{V}\cdot\text{s}$ ) [205].

Clearly, the s-subshell of these metal cations (Fe, Tb and Dy) are highly unlikely to contribute to the conduction band [207]. Therefore, this ternary amorphous oxide has a profoundly different origin of its high mobility as compared to the existing s-band high mobility amorphous oxides. This material also shows an emergent behavior because its conductivity and mobility far exceeds that of its constituent oxides. Our future work towards identifying the origin of this condensed matter behavior will focus on the hypothesis that there is a strong interaction between the Fe 5d and Lanthanide 4f levels. We conclude by speculating that the electronic properties of this material could be indirect evidence for an interesting new band structure physics

arising from the interaction of the transition and lanthanide metal cations. Additionally, this material could also be technologically relevant because it shows a combination of electrical conductivity and mobility that rivals that of the best known Indium-based transparent semiconducting oxides. Perhaps the most important implication of this work is that, given the vastly greater number of transition metals which have unfilled d-levels as compared to metals which show  $(n - 1)d^{10}ns^0$  behavior, it presents the intriguing possibility of creating a whole new class of functional oxide electronic materials.

## 7.4 Methods and Techniques

### 7.4.1 Material synthesis and processing

Thin films of Fe:Tb:Dy were deposited using the pulsed laser deposition (PLD) technique. Terfenol-D, which has a composition of  $(\text{Tb}_{0.3}\text{Dy}_{0.7})\text{Fe}_{1.92}$ , was used as a PLD target to deposit the thin films. This material was purchased from Etrema Products Inc., USA. The films were deposited on quartz or  $\text{SiO}_2/\text{Si}$  wafers having 400 nm of thermally grown oxide. Before deposition, the substrates were cleaned by sonicating them in acetone, isopropanol and DI water for 30 min each and then dried with nitrogen and stored. PLD was done using a Spectra Physics injection seeded Lab-130–50 Nd:YAG laser with wavelength of 266 nm, a pulse width of 9 ns and repetition rate of 50 Hz in a ultra high vacuum at a base pressure of  $5 \times 10^{-8}$  Torr. A laser energy density of  $0.56 \text{ J/cm}^2$  was used for deposition. Following the deposition the samples were removed and exposed to ambient air and stored in metallic sample boxes under ambient conditions. The annealing of the samples were done either in oxygen rich (air) or nitrogen rich environment (99.9% purity of  $\text{N}_2$  gas supplied by Airgas Inc., Knoxville, USA) in a programmable oven from MTI corporation (model no.: OTF-1200X) at  $500^\circ\text{C}$  for 2 hours. The contact pads for electrical measurements were made by masking the samples with Al foil and then depositing Ag pads on the amorphous films. The Ag pads were deposited using the e-beam evaporator at a base pressure of  $2 \times 10^{-8}$  Torr and were approximately 40 nm thick.

### 7.4.2 Surface characterization

Scanning electron microscopy (SEM) was used to obtain the morphology of the surface of the films deposited using PLD. The imaging was done using Zeiss Merlin SEM operated at 2 kV using an inlens detector. Roughness measurements of the as-prepared films were made by atomic force microscopy (AFM). Areas of  $4 \times 4 \mu\text{m}^2$  were scanned for the various films and root mean square (rms) roughness was calculated by averaging over multiple (up to 256) line profiles at different areas. The film roughness measurements were done using Nanonics Multiview 1000 AFM, which was operated in line-by-line tapping mode at a resolution of 256-by-256 and a rate of 8 ms per point. The cantilever tip had a radius of curvature measuring less than 40 nm.

### 7.4.3 Material characterization

#### TEM

The TEM sample for as-prepared film investigation was made by depositing 9 nm thick films onto ultrathin C substrates on mica. The film/C system was floated off from mica by immersion in water, yielding the electron transparent material (as described by Sachan et al. in ref. [153]). The O<sub>2</sub> annealed sample was prepared by depositing a 25 nm thick film onto electron transparent Si<sub>3</sub>N<sub>4</sub> grids (which had thickness 10 nm) with window size of 100 × 100 μm<sup>2</sup> supplied by Norcada, Canada. Oxidation of this sample was performed as described earlier. High resolution TEM images and diffraction patterns were taken in a Zeiss Libra 200MC at an acceleration voltage of 200kV, while the Z-contrast images and EELS spectra were taken with an aberration corrected (Nion, Inc.) dedicated STEM VG 501 UX operated at 100kV. This instrument is equipped with a cold field emission electron source and a Gatan Enfina EELS spectrometer.

#### XPS

XPS measurements were carried out at room temperature by using a SPECS Focus 500 monochromated Al Kα X-ray source operated at 380 W and a SPECS PHOIBOS-150 hemispherical electron analyzer at normal emission and 40 eV pass energy. Relative atomic concentrations were taken from comparison of Dy3d, Tb3d<sub>5/2</sub>, O1s, and Fe2p<sub>3/2</sub> core levels, analyzed and corrected for sensitivity and transmission factors in CasaXPS software.

#### XRD

As-deposited and annealed thin films were characterized using grazing incidence X-ray diffraction (GIXRD). These measurements were performed using a Panalytical X'Pert3 MRD X-ray diffractometer equipped with Cu Kα source (1.54059 Å) radiation and a Xe-proportional detector. The GIXRD patterns were recorded in a 2θ scanning mode using a parallel beam mirror on the incident beam side and a parallel plate collimator of 0.27 divergence on the diffracted beam side. A combination of beam mask and divergence slits was selected to illuminate the sample surface without illuminating the sample holder. In order to avoid diffraction from the sample holder the samples were mounted on a 2-inch single crystal silicon wafer oriented slightly off axis. The GIXRD patterns were collected in the 2θ range between 10-90° with a step size of 0.02° and step time of 7 sec/step.

### 7.4.4 Optical properties

The optical properties of the doped amorphous Fe<sub>2</sub>O<sub>3</sub> were measured using HR2000+ES spectrometer from Ocean Optics in transmission mode. The Tauc plots were generated by first converting transmission values (T in %) to absorption spectra using Beer-Lambert's law and then dividing by the film thickness (L) to convert to absorption coefficient ( $\alpha (cm^{-1}) = \frac{-1}{L} \ln \left( \frac{T\%}{100} \right)$ ) as a function of wavelength of light. The optical band gaps were then calculated by plotting Tauc plots with y-axis as  $(\alpha h\nu)^{1/m}$  as a function of  $h\nu$  (the photon energy given by product of Planck's constant  $h$  and frequency  $\nu$ ). Tangents were drawn at the



interband absorption region (rapid rise in spectrum) and were extrapolated to cut the x-axis, which gave the optical band gap values.  $m = 2$  was used to obtain direct band gap values.

#### 7.4.5 Magnetic properties

The magnetic properties of the as-prepared and annealed films were studied using surface magneto-optical Kerr effect (SMOKE) technique. The SMOKE measurements were done in the longitudinal orientation using an s-polarized laser beam of 633 nm wavelength making  $12.6^\circ$  angle of incidence with the normal to the substrate plane.

#### 7.4.6 Electrical properties

For measuring the electrical properties, silver pads were deposited on the four corners of the sample using e-beam evaporation, as described previously. Gold wires were then attached to the silver pads using silver epoxy paste. A Keithley 2400 sourcemeter was used to measure the sheet resistance and the hall mobility of the deposited amorphous oxide. Sheet resistance was measured using the van der Pauw method, where probe contacts are made at the four corners of the sample. Current was supplied at two adjacent contact points while voltage was measured at the two remaining contact points, i.e. if the four contacts were numbered 1, 2, 3, and 4, current was supplied between 1 and 2 ( $I_{12}$ ), while voltage was measured between 4 and 3 ( $V_{43}$ ) to get resistance  $R_{12,43}$ . In this way, the current direction was changed to cover all four sides, making sure to reverse the current direction on each side, resulting in eight total measurements. The four-probe resistance was measured by the Keithley sourcemeter working in 4-wire sensing mode. A LabVIEW code was written to collect data from the Keithley for 1 minute and then display the average value. This method of data collection ensured noise-compensated resistance values. After all the eight resistance values were measured ( $R_{12,43}$ ;  $R_{21,34}$ ;  $R_{34,21}$ ;  $R_{43,12}$ ;  $R_{41,32}$ ;  $R_{14,23}$ ;  $R_{23,14}$ ;  $R_{32,41}$ ), the following formula was used to calculate the sheet resistance:  $\exp(-\pi R_A/R_S) + \exp(-\pi R_B/R_S) = 1$ , where  $R_A = (R_{12,43} + R_{21,34} + R_{34,21} + R_{43,12})/4$ ,  $R_B = (R_{41,32} + R_{14,23} + R_{23,14} + R_{32,41})/4$ , and  $R_S$  is the sheet resistance. The resistivity was calculated as the product of the sheet resistance and the film thickness.

Hall measurements were made by supplying current along the contacts 3 and 1, and measuring the voltage between 4 and 2. For each value of current, the magnetic field was varied and the corresponding hall voltages were measured. Just like for sheet resistance measurements, a LabVIEW program was used to collect data to compensate for noise and drift. A plot was then made of Hall voltage vs applied magnetic field and a straight line fit was applied to it to obtain the slope of the plot. The hall mobility,  $\mu$ , was then calculated using:  $\mu = \left(\frac{dV}{dB}\right) \frac{1}{IR_S}$ , where  $I$  is the current supplied and  $R_S$  is the sheet resistance. The process was repeated with at least three different current values to obtain reliable hall mobilities. The carrier concentration,  $n$ , was calculated as  $n = \frac{1}{e\mu\rho}$ , where  $e$  is the charge on an electron, and  $\rho$  is the resistivity.

Sheet resistance was also measured as a function of temperature using Keithley 2400 sourcemeter. Although the same 4-wire sensing mode was used as for sheet resistance measurement, the contacts for current supply and voltage measurement were fixed to one configuration so as to not disturb the system while the film was being heated with an IR lamp. The temperature was measured periodically using a laser tempera-

ture sensor and the corresponding resistance value was noted from the sourcemeter.

## **7.5 Acknowledgments**

This work was primarily supported by ARO grant W911NF-13-1-0428, and a Science Alliance JDRD grant U013960010. One of the students was partly supported by NSF TNSCORE grant EPS-1004083 while XPS and SEM characterization was conducted through proposals CNMS2013-284 and CNMS2014-327 at the Center for Nanophase Materials Sciences, which is a DOE Office of Science User Facility. Some of the authors would also like to thank Prof. K. Islam at UT Knoxville for access to critical equipment for transport property measurements. The GIXRD experiments were performed using the instruments that were procured through the general infrastructure grant of DOE-Nuclear Energy University Program (DE-NE0000693). A portion of this work were performed at Oak Ridge National Laboratory, operated by UT-Battelle for the U.S. Department of energy under contract no. DE-AC05-00OR22725. RCP and BL acknowledge support from the Lab Directed Research and Development Program at ORNL.

## **7.6 Author Contributions Statement**

AM, HT, AF, GD, AB, and MP performed the materials synthesis and various characterization tasks. RK and AM designed the materials synthesis experiments and RK wrote the main manuscript text. RCP and BL, along with the other co-authors were involved in analyzing the data and concluding the results. All authors reviewed the manuscript.

## 7.7 Supplemental Information

### 7.7.1 Film roughness

Typical AFM line scans from the as-prepared films of 9, 25 and 37 nm thickness are shown in Fig. 7.4. From 256 such lines scans for each film thickness, the average root mean square (RMS) roughness was estimated as 0.944, 1.208 and 1.659 nm for 9, 25 and 37 nm films, respectively.

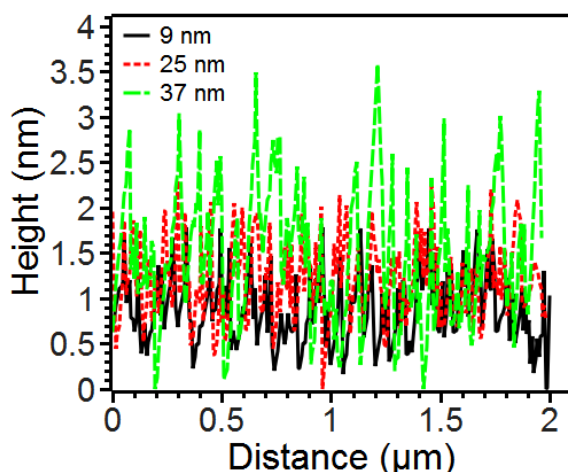


Figure 7.4: Surface roughness profile of as-deposited films measured using AFM.

### 7.7.2 GIXRD measurements of films

Fig. 7.5(a) shows the GIXRD scan of the Terfenol-D target which confirmed that the starting materials had the right metallic composition of Terfenol-D. In Fig. 7.5(b) GIXRD scans of 25 nm thick films in as-prepared and the two annealed cases is shown and compared to GIXRD from the SiO<sub>2</sub>/Si substrate. Since no features were evident from the films we concluded that they had an amorphous microstructure. The indexing of the XRD peaks was done using the ICSD database [212]. For the indexing of Terfenol-D, indexing till 70° was done with the help of ICSD database, while the remainder was based on published literature [213, 212].

### 7.7.3 Tauc plot measurement

Fig. 7.6(a), the Tauc plot of the three as-prepared films (with thickness of 9, 25 and 37 nm) is shown. The Band gap value was 3, 2.82, and 2.7 eV respectively. From these measurements, the average band gap value was obtained as  $2.85 \pm 0.14$  eV.

### 7.7.4 Magnetic measurements by SMOKE

The as-prepared and annealed films showed no Kerr rotation within the detection limit of the SMOKE system. The Kerr plots for the as-prepared and O<sub>2</sub> annealed film with 25 nm thickness are shown in Fig.

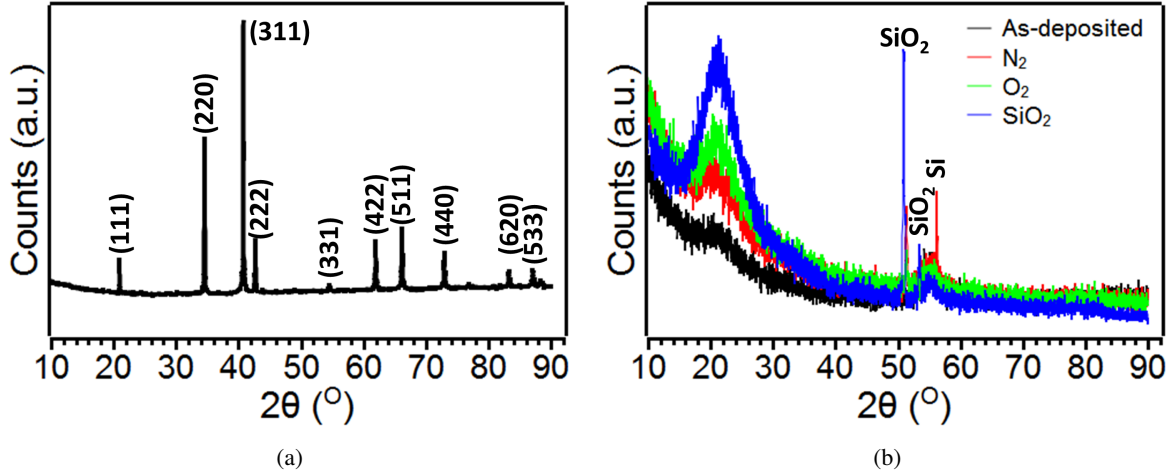


Figure 7.5: (a) Shows the XRD of the Terfenol-D target. Indexing of the various peaks showed that the target was consistent with the original Terfenol-D composition. (b) Comparison of GIXRD scans of as-prepared, nitrogen annealed, and oxygen annealed films of 25 nm thickness as well as the underlying substrate which was SiO<sub>2</sub>(400 nm)/Si. The only features evident from the films were the underlying substrate features, as indicated on the figure. This confirmed that the films were amorphous.

7.6(b). Similar results were obtained for all other films (i.e. as-prepared 9, 37, 74 nm) and N<sub>2</sub> annealed sample. From this it was concluded that no room temperature magnetism was present in these films.

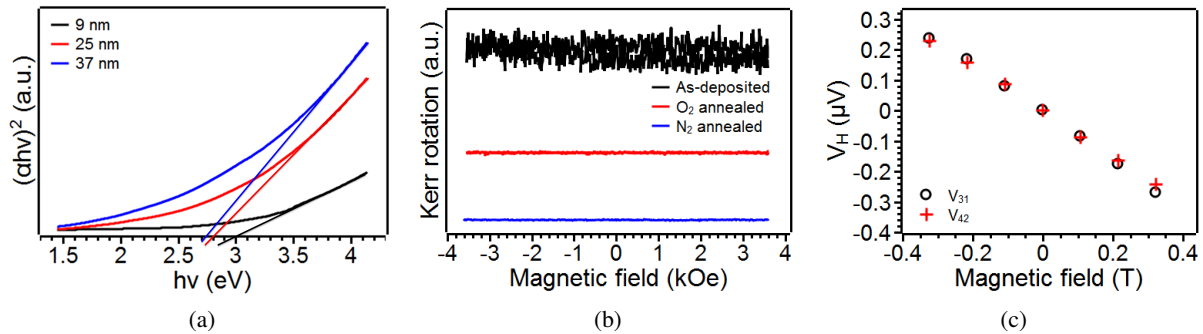


Figure 7.6: (a) Tauc plot of as-deposited films. (b) Kerr rotation measurements of as-prepared and annealed films. (c) Plot of Hall voltage as a function of applied magnetic field for a 74 nm thick as-prepared film studied for two different voltage configurations for an applied current of 100  $\mu$ A.

### 7.7.5 Hall Effect Measurement

The hall voltage versus magnetic field data was used to calculate the hall coefficient and mobility. The hall voltage versus magnetic field curve was linear, and a typical case is shown in Fig. 7.6(c) for the 74 nm thick as-prepared film. Similar linear curves were obtained for all other samples measured (as prepared and annealed).

### 7.7.6 XPS Measurements

Survey scans from the surface of as prepared and O<sub>2</sub> annealed films are shown in Fig. 7.7. Analysis based on the energy position of the various features compared to standards noted in the Handbook for XPS [201] revealed that Fe, Tb, Dy and O were the primary components while hydrocarbon peaks were also present due to handling conditions.

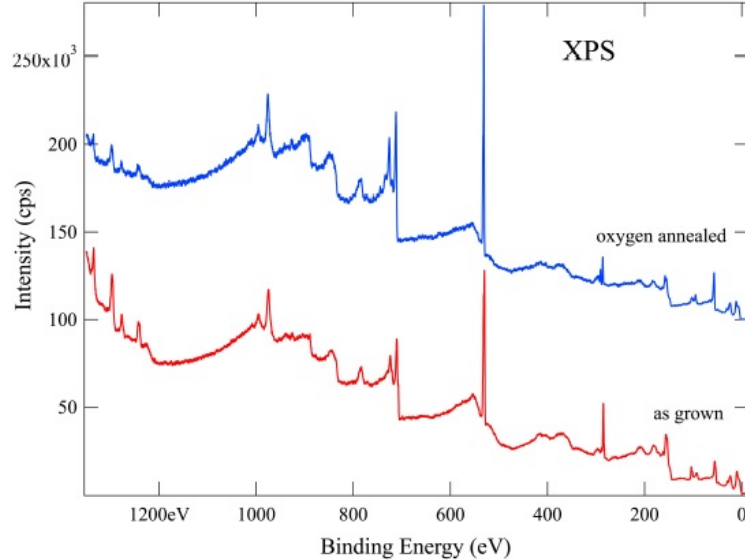


Figure 7.7: XPS survey scans to determine elements present in the as-prepared and annealed films.

### 7.7.7 SEM Measurement

In the as-prepared films large surface nanoparticles or PLD chunks could be seen on the surface of the films, and this was characteristic of the PLD process (as shown in manuscript Fig. 1c). Upon annealing in air there was a decrease in the size of particulates presumably due to oxidation, as evident from the SEM images of the annealed samples shown in Fig. 7.8(a).

### 7.7.8 TEM and EELS measurements

Fig. 7.8(b) shows the micrograph of a 25 nm thick film made by deposition onto a Si<sub>3</sub>N<sub>4</sub> electron transparent grid and annealed in O<sub>2</sub> at 500°C for 2 hours. Like the as-prepared films, the microstructure was amorphous for this film as well.

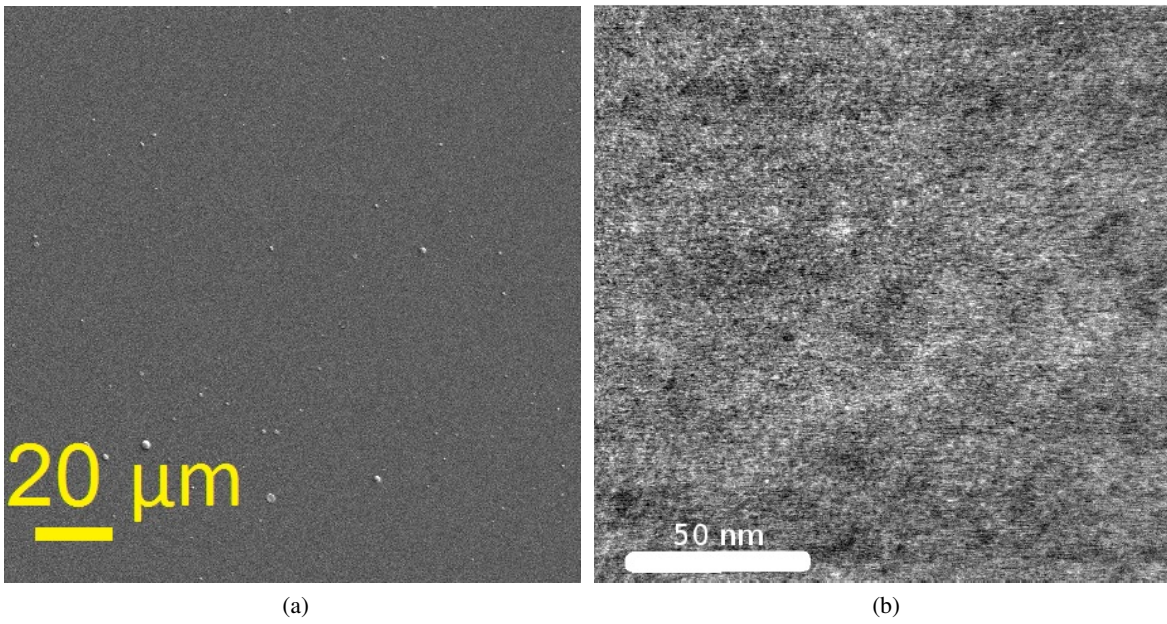


Figure 7.8: (a) SEM micrograph of the surface of an  $O_2$  annealed film shows a smooth morphology and a decrease in the nanoparticles from the PLD process in comparison to the as-prepared films (shown in manuscript Fig. 1(c)). (b) TEM micrograph of  $O_2$  annealed film.

## Chapter 8

# Conclusion and Future work

In this chapter we summarize the key findings of this thesis and will discuss potential future problems that could be pursued.

### 8.1 Conclusion

- *In Chapter 3*, we have described a simple and efficient way to make 2D periodic nanostructures of different metals on electron transparent substrates. Nanostructures of plasmonic Ag, ferromagnetic Co, and bimetal structures of Co-Ag were synthesized by nanosphere lithography on ultra thin carbon films. The nanostructure array/carbon system could be easily detached from an underlying mica support by immersion in water, resulting in transferable, flexible, and large area electron transparent materials. This technique could help accelerate discovery of new plasmonic phenomenon and/or better nanostructured materials for plasmonic and magnetic applications. The sample preparation technique has been summarized in the schematic shown in Fig. 8.1.

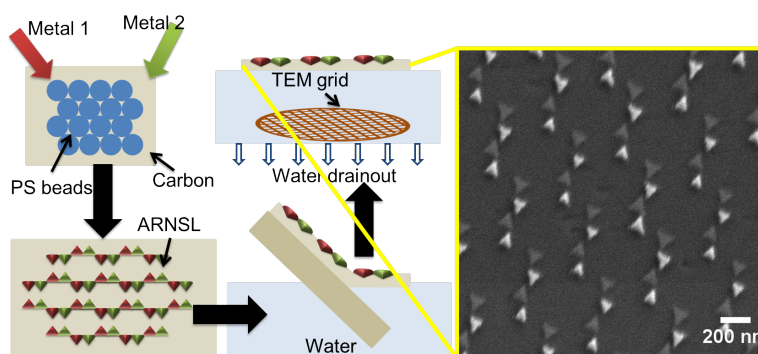


Figure 8.1: Schematic showing the various steps to form 2D periodic nanostructure arrays on electron transparent substrate [155].

- *Chapter 4*: We have demonstrated that the measurement of the plasmonic behavior of metallic nanoparticles using UV-vis spectroscopy could be useful towards investigations of their oxidation kinetics.

Investigations of the Co-Ag immiscible nanoparticle system show that the LSPR behavior can accurately predict the oxide growth in the nanoparticle system. For the Co-Ag case, the Ag oxide-free lifetime could be tuned to increase by 12.7 days per volume % of Co and was enhanced 8 fold for the 28.7% Co case (a schematic summarizing it in Fig. 8.2 ). This behavior could be described by a theoretical model based on optical mean field approximation. Thus, these Ag bimetal systems which are very stable in ambient air environment could potentially be employed for various plasmon related applications like surface enhanced Raman sensing and LSPR sensing due to refractive index change from chemical and biological effects.

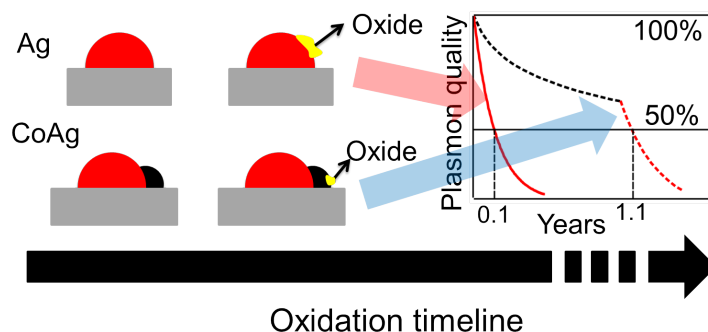


Figure 8.2: Schematic showing by synthesizing bimetallics of CoAg, the lifetime of Ag increases.

- *Chapter 5:* We have investigated the size and energy dependence of the plasmonic quality factor in hemispherical Ag and AgCo bimetallic NPs. The effect of different ambient environments such as insulating, semiconducting and metallic films on the Ag plasmon showed that the quality factor of the plasmons decreased with placing the Ag in these media. To ascertain the contribution from radiative and non-radiative effects we compared Ag hemispherical nanoparticles to triangular particles. From this the explicit dependence of size and volume on the radiative and non-radiative effects was estimated and the quantum efficiency was also calculated. Comparison with AgCo bimetallics withing the quasi-static and effective medium models reveled that the AgCo bimetal system can significantly influence the radiative energy transfer from the plasmonic nanoparticles. This resulted in the bimetallic systems having comparable or better quality factor and or quantum efficiency to that of pure Ag in certain regimes of resonance energy and particle volume. These results demonstrate that the bimetal nanostructures provide a pathway to tune the quality factor and quantum efficiency of plasmonic processes.
- *Chapter 6:* We have developed a simple approach to express Mie's multipole expansion within effective medium approximation theories. This theory captures the physical behavior of the plasmon resonance as a function of size and adequately describes the quadrupole resonance. The derived result can be easily applied to multicomponent system analysis and can potentially be used in conjunction with other EMA approaches for analysis of reflection and transmission in nanostructured systems. Future work, will be aimed at utilizing this approach to investigate the optical transmission and reflection



from metal multicomponent systems.

- *Chapter 7:* We synthesized an amorphous transparent semiconductor oxide of the ternary alloy Fe-Tb-Dy and characterized the semiconductor for its optical and electrical properties and characterized the material properties. This ternary semiconductor oxide showed high conduction and mobility values comparable to the IGZO material. All currently known amorphous oxide semiconductors with high mobility have metals with  $(n-1)d^{10}ns^0$  electronic configuration. Clearly, our new material containing Fe, Tb and Dy, breaks this paradigm and so its high mobility must come from a different reason. This material also shows an emergent behavior because its conductivity and mobility far exceeds that of its constituent oxides. Perhaps the most important implication of this work is that, given the vastly greater number of transition metals which have unfilled d-levels as compared to metals which show  $(n-1)d^{10}ns^0$  behavior, it presents the intriguing possibility of creating a whole new class of functional oxide electronic materials.

## 8.2 Future work

### 8.2.1 Bimetal related work

- *Bimetal NP synthesis:* The detailed morphology dependent optical and MO studies can be done. By synthesizing bimetal structures using NSL, the nanoparticle morphology can be tuned in a controlled manner. Few of the NSL structures achieved as a interplay of film thickness, angle of deposition and the laser energy are summarized in Fig. 8.3.

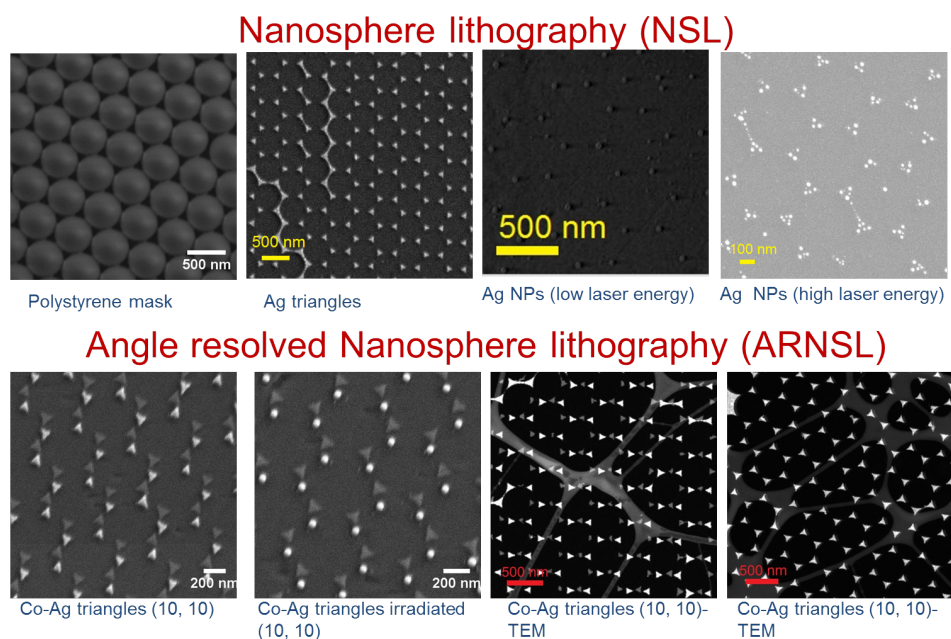


Figure 8.3: Possible different morphologies of NPs synthesized using NSL.

- Oxidation stability:** As shown in Chapter 3 of the thesis, by synthesizing different compositions of Co-Ag NPs, the oxidation stability of the NP can be greatly enhanced. This study can be further extended to incorporate other metals like Fe and Ni, which follow the guideline stated in the introduction chapter for material selection. Here in Fig. 8.4, we demonstrate that these bimetal of Fe and Ni can also stabilize the Ag part of the bimetal by galvanic coupling in a single nanoparticle. These bimetal NPs were synthesized using pulsed laser dewetting. Fig. 8.4 (a) shows the optical spectrums of Co-Ag, Fe-Ag and Ni-Ag bimetals of equal thickness and Fig. 8.4 (b) compares the oxidation behavior of these bimetals as a function of time.

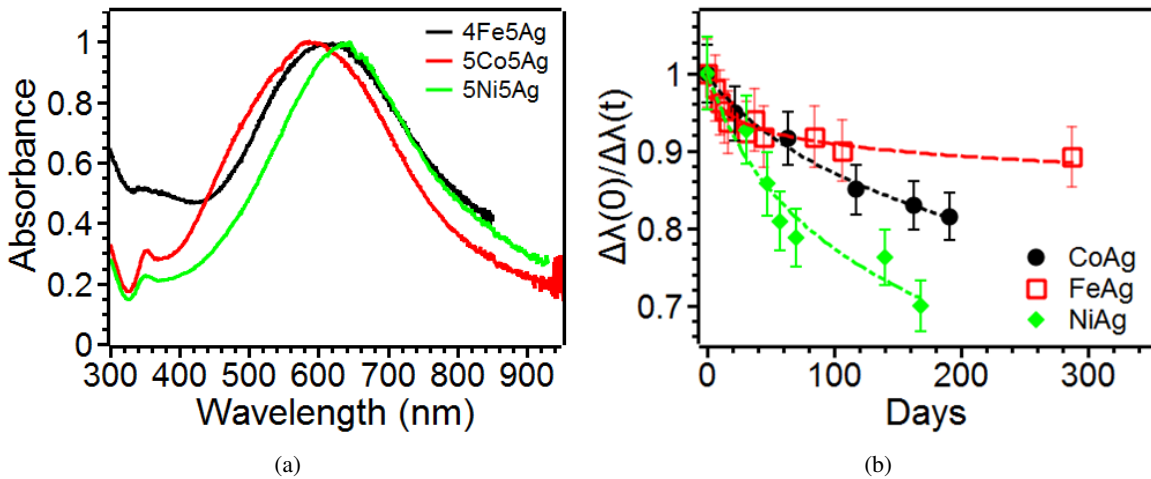


Figure 8.4: (a) Compares the absorption spectrum of Co-Ag, Fe-Ag and Ni-Ag NPs of almost equal thicknesses. (b) Compares the optical bandwidth degradation of the bimetals in (a).

- Magneto-optical properties:** The bimetals of ferromagnetic materials (Co, Fe, Ni) with plasmonic materials (Ag) can be synthesized using pulsed laser dewetting and NSL for the magneto-optical studies. Current measurements were done using a single probing wavelength of 633 nm using the SMOKE setup. The MO study could be done using with a tunable light source that spans a larger wavelength range. Some of the initial MO results for Co-Ag bimetallic NPs synthesized using pulsed laser dewetting are shown in Fig. 8.5. Similar MO studies conducted on Fe-Ag nanotriangles synthesized using NSL are summarized in Fig. 8.6. Similar MO studies can be done by controlling the spacing between the individual nanotriangles using ARNSL.
- Plasmon quality factor:** The plasmon quality factor study could be extended to other particle morphologies such as triangles and bimetal systems such as Fe-Ag and Ni-Ag. Here are some preliminary results of plasmon quality factor and bandwidth study done on monometallic and bimetallic Ag nanotriangles synthesized using NSL. The results are shown in Fig. 8.7.

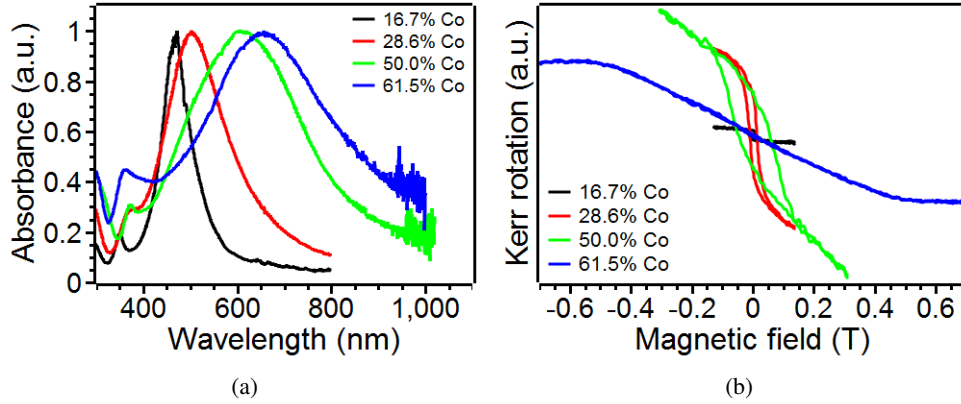


Figure 8.5: (a) Compares the absorption spectrum of Co-Ag NPs arrays for different Co percentage. (b) Compares the Kerr hysteresis loops for different Co compositions for longitudinal.

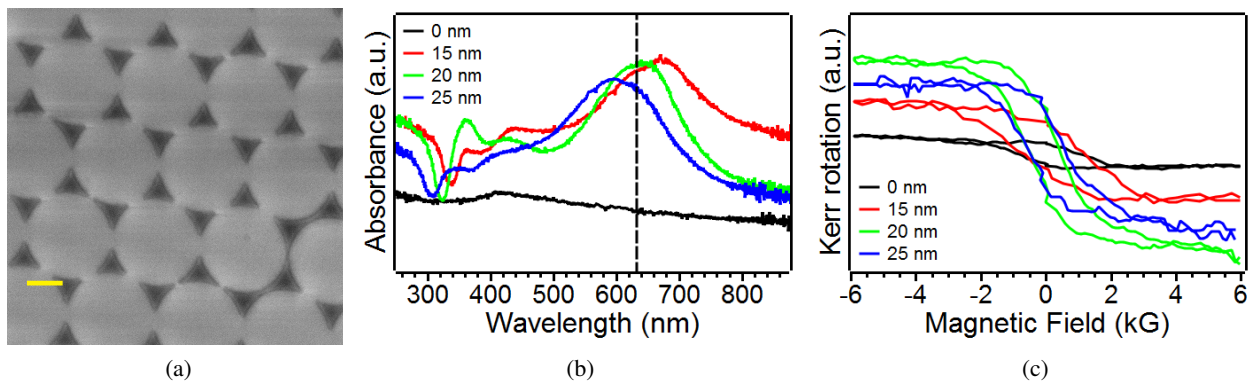


Figure 8.6: (a) Representative SEM image for Fe-Ag nanotriangles synthesized using 500 nm PS bead template. The thicknesses of Fe and Ag are 12 and 15 nm, respectively. The length of the scale bar is 200 nm. (b) Absorption spectra for three different thicknesses of Ag for fixed Fe thickness in Fe-Ag nanotriangles. (c) Kerr rotation comparison for the three different thicknesses of Ag with fixed Fe amount.

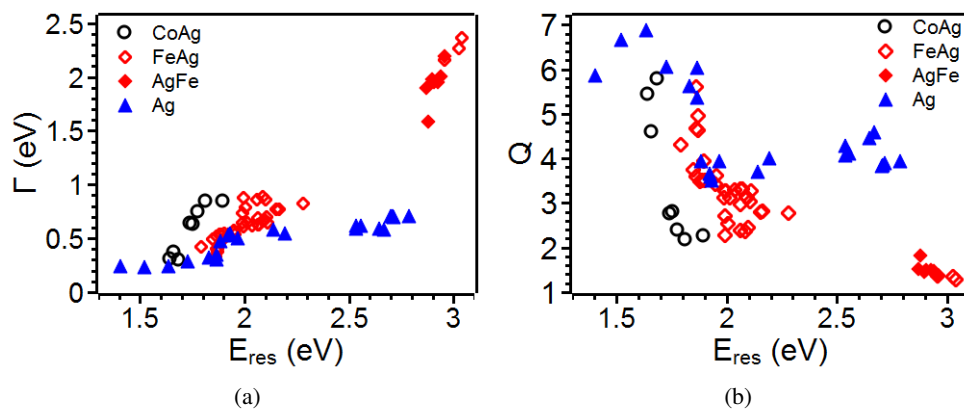


Figure 8.7: (a) Plots the bandwidth of Ag, Co-Ag and Fe-Ag nanotriangles as a function of plasmon resonance energy. (b) Plots the quality factor of Ag, Co-Ag and Fe-Ag nanotriangles as a function of plasmon resonance energy.

- *Plasmonic coupling between quantum dots and plasmonic nanoparticles:* The plasmonic interaction studies of quantum dots with Ag NPs and bimetallic Ag NPs can be performed. For the interaction of the plasmons of quantum dots and nanoparticles, the excited plasmons energies of the two systems should be close to see the maximum coupling. This can be achieved by tuning the plasmon energy of NPs, which can be achieved by synthesizing bimetals of Ag. As shown in this thesis the Ag plasmon energy range can be tuned from 1.5 to 3 eV by controlling the shape, size and the bimetal composition. The quantum dots of CdSe have plasmons in the energy range below 2.5 eV, which is well within the Ag NP range. Fig. 8.8 (a) shows the photograph of the synthesized CdSe quantum dots. The quantum dot synthesis was performed in ORNL with the help of Dr. Michael Hu. Fig. 8.8 (b) shows the absorbance spectrum and the photoluminescence of the as synthesized quantum dots after purification.

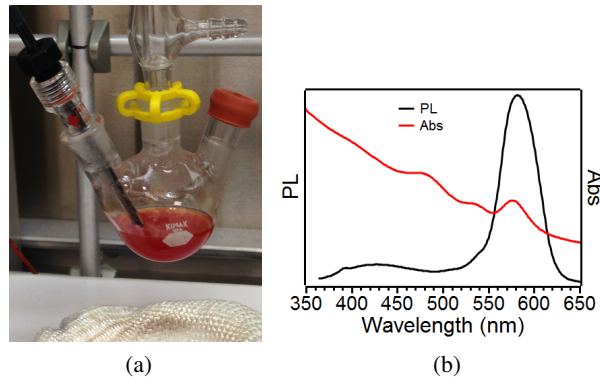


Figure 8.8: (a) Photograph of synthesized CdSe quantum dots. (b) Shows the absorbance and the photoluminescence of CdSe quantum dots.

### 8.2.2 Terfenol-D related work

The amorphous semiconductor oxides of ternary alloy of Fe-Tb-Dy is an unexplored area and lot of work is required to understand its behavior. Some of the key things that can be studied are:

- Stability of films in ambient environment and on its transport properties.
- Role of deposition techniques: e-beam vs PLD
- Magnetism in Terfenol-D
- Composition of Tb, Dy and Fe on the semiconductor properties
- Controlling the electron density for semiconductor based application
- Finding the crystallization temperature
- Role of annealing in air and nitrogen on the semiconductor properties

- Temperature dependent semiconductor properties
- Device fabrication

# **Bibliography**

- [1] O. Pena-Rodriguez and U. Pal, “Au@ag core-shell nanoparticles: efficient all-plasmonic fano-resonance generators,” *Nanoscale*, vol. 3, p. 3609, 2011.
- [2] L. Wang, Z. Clavero, C. Huba, K. J. Carroll, E. E. Carpenter, D. Gu, and R. A. Lukaszew, “Plasmonics and enhanced magneto-optics in core-shell co-ag nanoparticles,” *Nano Lett.*, vol. 11, pp. 1237–1240, 2011.
- [3] S. A. Maier, *Plasmonics: Fundamentals and Applications*. Springer, 2007.
- [4] X. Li, C. Jia, B. Ma, W. Wang, Z. Fang, G. Zhang, and X. Guo, “Substrate-induced interfacial plasmonics for photovoltaic conversion,” *Scientific Reports*, vol. 5, p. 14497, 2015.
- [5] J. C. Bantbi, D. Meneses-Rodriguez, F. Garcia, M. U. Gonzalez, A. Garcia-Martin, and G. Armelles, “High magneto-optical activity and low optical losses in metal-dielectric au/co/au-sio<sub>2</sub> magnetoplasmonic nanodisks,” *Adv. Mater.*, vol. 24, pp. OP36–OP41, 2012.
- [6] E. Prodan, C. Radloff, N. J. Halas, and P. Nordlander, “A hybridization model for the plasmon response of complex nanostructures,” *Science*, vol. 302, pp. 419–422, 2003.
- [7] A. Holewinski, J. C. Idrobo, and S. Linic, “High-performance ag-co alloy catalysts for electrochemical oxygen reduction,” *Nature Chem.*, vol. 6, pp. 828–834, 2014.
- [8] B. Lukyanchuk, N. I. Zheludev, S. A. Maier, N. J. Halas, P. Nordlander, H. Giessen, and C. T. Chong, “The fano resonance in plasmonic nanostructures and metamaterials,” *Nat. Mater.*, vol. 9, pp. 707–715, 2010.
- [9] M. Faraday, “On the magnetization of light and the illumination of magnetic lines of force,” *Phil. Trans. R. Soc. Lond.*, vol. 136, pp. 1–20, 1846.
- [10] D. Meneses-Rodriguez, E. Ferreiro-Vila, P. Prieto, J. Anguita, M. U. Gonzalez, J. M. Garcia-Martin, A. Cebollada, A. Garcia-Martin, and G. Armelles, “Probing the electromagnetic field distribution within a metallic nanodisk,” *Small*, vol. 7, pp. 3317–3323, 2011.
- [11] G. Armelles, A. Cebollada, A. Garcia-Martin, J. M. Garcia-Martin, M. U. Gonzalez, J. B. Gonzalez-Diaz, E. Ferreiro-Vila, and J. F. Torrado, “Magnetoplasmonic nanostructures: systems supporting both plasmonic and magnetic properties,” *J. Opt. A: Pure Appl. Opt.*, vol. 11, p. 114023, 2009.

- [12] Z. Zheng, T. Tachikawa, and T. Majima, "Single-particle study of pt-modified au nanorods for plasmon-enhanced hydrogen generation in visible to near-infrared region," *J. Am. Chem. Soc.*, vol. 136, pp. 6870–6873, 2014.
- [13] S. Neatu, J. A. Macia-Agullo, P. Concepcion, and H. Garcia, "Gold-copper nanoalloys supported on tio<sub>2</sub> as photocatalysts for co<sub>2</sub> reduction by water," *J. Am. Chem. Soc.*, vol. 136, pp. 15969–15976, 2014.
- [14] D. Tilman and E. C. Snell-Rood, "Diversity breeds complementarity," *Nature*, vol. 515, pp. 44–45, 2014.
- [15] R. Sachan, S. Yadavali, N. Shirato, H. Krishna, V. Ramos, G. Duscher, S. J. Pennycook, A. K. Gangopadhyay, H. Garcia, and R. Kalyanaraman, "Self-organized bimetallic ag-co nanoparticles with tunable localized surface plasmons showing high environmental stability and sensitivity," *Nanotechnology*, vol. 23, p. 275604, 2012.
- [16] R. Sachan, V. Ramos, A. Malasi, B. Bartley, G. Duscher, and R. Kalyanaraman, "Oxidation resistant ag nanoparticles for ultrastable plasmonic applications," *Adv. Mater.*, vol. 25, pp. 2045–2050, 2013.
- [17] R. Sachan, A. Malasi, J. Ge, S. Yadavali, H. Krishna, A. Gangopadhyay, H. Garcia, G. Duscher, and R. Kalyanaraman, "Ferroplasmons: Intense localized surface plasmons in metal-ferromagnetic nanoparticles," *ACS Nano*, vol. 8, pp. 9790–9798, 2014.
- [18] O. Primera-Pedrozo, J. I. Jerez-Rozo, E. Cruz-Montoya, T. Luna-Pineda, L. C. Pacheco-Londono, and S. Hernandez-Rivera, "Nanotechnology-based detection of explosives and biological agents simulants," *IEEE Sens. J.*, vol. 8, pp. 963–973, 2008.
- [19] A. V. Kabashin, P. Evans, S. Pastkovsky, W. Hendren, G. A. Wurtz, R. Atkinson, R. Pollard, V. A. Podolskiy, and A. V. Zayats, "Plasmonic nanorod metamaterials for biosensing," *Nature Mater.*, vol. 8, pp. 867–871, 2009.
- [20] H. A. Atwater and A. Polman, "Plasmonics for improved photovoltaic devices," *Nat. Mater.*, vol. 9, pp. 205–213, 2010.
- [21] D. O'Connor and A. V. Zayats, "Data storage: The third plasmonic revolution," *Nat. Nanotechnol.*, vol. 5, pp. 482–483, 2010.
- [22] S. Linic, P. Christopher, and D. Ingram, "Plasmonic-metal nanostructures for efficient conversion of solar to chemical energy," *Nat. Mater.*, vol. 10, pp. 911–921, 2011.
- [23] B. Gallinet and J. F. Martin, "Analytical description of fano resonances in plasmonic nanostructures," in *AIP Conf. Proc.*, vol. 1398, pp. 73–75, 2011.
- [24] P. A. Gonzalez, P. Albella, F. Neubrech, C. Huck, J. Chen, F. Golmar, F. Casanova, L. E. Hueso, A. Pucci, J. Aizpurua, and R. Hillenbrand, "Experimental verification of the spectral shift between



- near- and far-field peak intensities of plasmonic infrared nanoantennas,” *Phys. Rev. Lett.*, vol. 110, p. 203902, 2013.
- [25] M. D. Doherty, A. Murphy, R. J. Pollard, and P. Dawson, “Surface-enhanced raman scattering from metallic nanostructures: Bridging the gap between the near-field and far-field responses,” *Phys. Rev. X*, vol. 3, p. 011001, 2013.
- [26] J. Zuloaga and P. Nordlander, “On the energy shift between near-field and far-field peak intensities in localized plasmon systems,” *Nano Lett.*, vol. 11, pp. 1280–1283, 2011.
- [27] B. Grzeskiewicz, K. Ptaszynski, and M. Kotkowiak, “Near and far-field properties of nanoprisms with rounded edges,” *Plasmonics*, vol. 9, pp. 607–614, 2014.
- [28] C. Menzel, E. Hebestreit, S. Muhligh, C. Rockstuhl, S. Burger, F. Lederer, and T. Pertsch, “The spectral shift between near- and far-field resonances of optical nano-antennas,” *Opt. Express*, vol. 22, pp. 9971–9982, 2014.
- [29] F. Moreno, P. Albella, and M. Nieto-Vesperinas, “Analysis of the spectral behavior of localized plasmon resonances in the near- and far-field regimes,” *Langmuir*, vol. 29, pp. 6715–6721, 2013.
- [30] M. Rahmani, E. Yoxall, B. Hopkins, Y. Sonnefraud, Y. Kivshar, M. Hong, C. Phillips, S. A. Maier, and A. E. Miroshnichenko, “Plasmonic nanoclusters with rotational symmetry: Polarization-invariant far-field response vs changing near-field distribution,” *ACS Nano*, vol. 7, pp. 11138–11146, 2013.
- [31] J. M. Sanz, D. Ortiz, R. Alcaraz de la Osa, J. M. Saiz, F. Gonzalez, A. S. Brown, M. Losurdo, H. O. Everitt, and F. Moreno, “Uv plasmonic behavior of various metal nanoparticles in the near- and far-field regimes: Geometry and substrate effects,” *J. Phys. Chem. C*, vol. 117, pp. 19606–19615, 2013.
- [32] A. Yanai, M. Grajower, G. M. Lerman, M. Hentschel, H. Giessen, and U. Levy, “Near- and far-field properties of plasmonic oligomers under radially and azimuthally polarized light excitation,” *ACS Nano*, vol. 8, pp. 4969–4974, 2014.
- [33] B. M. Ross, S. Tasoglu, and L. P. Lee, “Plasmon resonance differences between the near- and far-field and implications for molecular detection,” in *Plasmonics: Metallic Nanostructures and Their Optical Properties VII*, 2009.
- [34] H. Wang, D. W. Brandl, F. Le, P. Nordlander, and N. J. Halas, “Nanorice: A hybrid plasmonic nanostructure,” *Nano Lett.*, vol. 6, pp. 827–832, 2006.
- [35] G. Bachelier, I. R. Antoine, E. Benichou, C. Jonin, N. Del Fatti, F. Vallee, and P. F. Brevet, “Fano profiles induced by near-field coupling in heterogeneous dimers of gold and silver nanoparticles,” *Phys. Rev. Lett.*, vol. 101, pp. 197401 (1–4), 2008.
- [36] Y. Sun and Y. Xia, “Increased sensitivity of surface plasmon resonance of gold nanoshells compared to that of gold solid colloids in response to environmental changes,” *Anal. Chem.*, vol. 74, pp. 5297–5305, 2002.

- [37] S. Tripathy, R. Marty, V. K. Lin, S. L. Teo, E. Ye, A. Arbouet, L. Saviot, C. Girard, M. Y. Han, and A. Mlayah, “Acousto-plasmonic and surface-enhanced raman scattering properties of coupled gold nanospheres/nanodisk trimers,” *Nano Lett.*, vol. 11, pp. 431–437, 2011.
- [38] P. K. Jain, Y. Xiao, R. Walsworth, and A. E. Cohen, “Surface plasmon resonance enhanced magneto-optics (supremo): Faraday rotation enhancement in gold-coated iron oxide nanocrystals,” *Nano Lett.*, vol. 9, pp. 1644–1650, 2009.
- [39] T. Atay, J. H. Song, and A. V. Nurmikko, “Strongly interacting plasmon nanoparticle pairs: From dipole-dipole interaction to conductively coupled regime,” *Nano Lett.*, vol. 4, pp. 1627–1631, 2004.
- [40] A. N. Grigorenko, A. K. Geim, H. F. Gleeson, Y. Zhang, A. A. Firsov, I. Y. Khrushchev, and J. Petrovic, “Nanofabricated media with negative permeability at visible frequencies,” *Nature*, vol. 438, pp. 335–338, 2005.
- [41] S. Link and M. El-Sayed, “Spectral properties and relaxation dynamics of surface plasmon electronic oscillations in gold and silver nanodots and nanorods,” *J. Phys. Chem. B*, vol. 103, pp. 8410–8426, 1999.
- [42] W. Zhou, S. J. Pennycook, and J. C. Idrobo, “Localization of inelastic electron scattering in the low-loss energy regime,” *Ultramicroscopy*, vol. 119, pp. 51–56, 2012.
- [43] P. Schattschneider, S. Rubino, C. Hebert, J. Ruzs, J. Kunes, P. Novak, E. Carlino, M. Fabrizioli, G. Panaccione, and G. Rossi, “Detection of magnetic circular dichroism using a transmission electron microscope,” *Nat. Lett.*, vol. 441, pp. 486–488, 2006.
- [44] J. Nelayah, M. Kociak, O. Stephan, F. J. G. de Abajo, M. Tence, I. Henrard, D. Taverna, I. P. Santos, L. M. Liz-Marzan, and C. Colliex, “Mapping surface plasmons on a single metallic nanoparticle,” *Nat. Phys.*, vol. 3, pp. 348–353, 2007.
- [45] R. F. Egerton, “Electron energy-loss spectroscopy in the tem,” *Rep. Prog. Phys.*, vol. 72, p. 016502, 2009.
- [46] S. Rao, K. Muraleedharan, and C. Humphreys, *Microscopy: Science, Technology, Applications and Education*. Formatex Research Center, 2010.
- [47] J. C. Hulteen and R. P. Van Duyne, “Nanosphere lithography: A materials general fabrication process for periodic particle array surfaces,” *J. Vac. Sci. Technol. A*, vol. 13, pp. 1553–1558, 1995.
- [48] C. L. Haynes, A. D. McFarland, M. T. Smith, J. C. Hulteen, and R. P. Van Duyne, “Angle-resolved nanosphere lithography: Manipulation of nanoparticle size, shape, and interparticle spacing,” *J. Phys. Chem. B*, vol. 106, pp. 1898–1902, 2002.
- [49] C. L. Haynes and R. P. Van Duyne, “Dichroic optical properties of extended nanostructures fabricated using angle-resolved nanosphere lithography,” *Nano Lett.*, vol. 3, pp. 939–943, 2003.

- [50] N. Vogel, S. Goerres, K. Landfester, and C. K. Weiss, "A convenient method to produce close-and non-close-packed monolayers using direct assembly at the air-water interface and subsequent plasma-induced size reduction," *Macromol. Chem. Phys.*, vol. 212, pp. 1719–1734, 2011.
- [51] V. Ng, Y. V. Lee, B. T. Chen, and A. O. Adeyeye, "Nanostructure array fabrication with temperature-controlled self-assembly techniques," *Nanotechnology*, vol. 13, pp. 554–558, 2002.
- [52] P. Pieranski, "Two-dimensional interfacial colloidal crystals," *Phys. Rev. Lett.*, vol. 45, p. 569, 1980.
- [53] A. J. Hurd and D. W. Schaefer, "Diffusion-limited aggregation in two dimensions," *Phys. Rev. Lett.*, vol. 54, p. 1043, 1985.
- [54] F. Lenzmann, K. Li, A. H. Kitai, and H. D. H. Stover, "Thin-film micropatterning using polymer microspheres," *Chem. Mater.*, vol. 6, pp. 156–159, 1994.
- [55] K. U. Fulda and B. Tiede, "Langmuir films of monodisperse 0.5  $\mu\text{m}$  spherical polymer particles with a hydrophobic core and a hydrophilic shell," *Adv. Mater.*, vol. 6, pp. 288–290, 1994.
- [56] R. Micheletto, H. Fukuda, and M. Ohtsut, "A simple method for the production of a two-dimensional, ordered array of small latex particles," *Langmuir*, vol. 11, pp. 3333–3336, 1995.
- [57] J. Rybczynski, U. Ebels, and M. Giersig, "Large-scale, 2d arrays of magnetic nanoparticles," *Colloids and Surfaces A*, vol. 219, pp. 1–6, 2003.
- [58] N. D. Denkov, O. D. Velev, P. A. Kralchevsky, I. B. Ivanov, H. Yoshimura, and K. Nagayama, "Mechanism of formation of two-dimensional crystals from latex particles on substrates," *Langmuir*, vol. 8, pp. 3183–3190, 1992.
- [59] N. D. Denkov, O. D. Velev, P. A. Kralchevsky, I. B. Ivanov, H. Yoshimura, and K. Nagayama, "Two-dimensional crystallization," *Nature*, vol. 361, p. 26, 1993.
- [60] S. Rakers, L. F. Chi, and H. Fuchs, "Influence of the evaporation rate on the packing order of polydisperse latex monofilms," *Langmuir*, vol. 13, pp. 7121–7124, 1997.
- [61] S. L. Kuai, X. F. Hu, A. Hache, and V. V. Truong, "High-quality colloidal photonic crystals obtained by optimizing growth parameters in a vertical deposition technique," *Journal of Crystal Growth*, vol. 267, pp. 317–324, 2004.
- [62] S. H. Park, D. Qin, and Y. Xia, "Crystallization of mesoscale particles over large areas," *Adv. Mater.*, vol. 10, pp. 1028–1032, 1998.
- [63] R. M. Amos, J. G. Rarity, P. R. Tapster, T. J. Shepherd, and S. C. Kitson, "Fabrication of large-area face-centered-cubic hard-sphere colloidal crystals by shear alignment," *Phys. Rev. E*, vol. 61, p. 2929, 2000.

- [64] Y. Lu, Y. Yin, B. Gates, and Y. Xia, "Growth of large crystals of monodispersed spherical colloids in fluidic cells fabricated using non-photolithographic methods," *Langmuir*, vol. 17, pp. 6344–6350, 2001.
- [65] X. Meng and D. Qiu, "Gas-flow-induced reorientation to centimeter-sized two-dimensional colloidal single crystal of polystyrene particle," *Langmuir*, vol. 30, pp. 3019–3023, 2014.
- [66] T. R. Jensen, G. C. Schatz, and R. P. Van Duyne, "Nanosphere lithography: Surface plasmon resonance spectrum of a periodic array of silver nanoparticles by ultraviolet-visible extinction spectroscopy and electrodynamic modeling," *J. Phys. Chem. B*, vol. 103, pp. 2394–2401, 1999.
- [67] T. R. Jensen, M. D. Malinsky, C. L. Haynes, and R. P. Van Duyne, "Nanosphere lithography: Tunable localized surface plasmon resonance spectra of silver nanoparticles," *J. Phys. Chem. B*, vol. 104, pp. 10549–10556, 2000.
- [68] S. M. Weekes, F. Y. Ogrin, W. A. Murray, and P. S. Keatley, "Macroscopic arrays of magnetic nanostructures from self-assembled nanosphere templates," *Langmuir*, vol. 23, pp. 1057–1060, 2007.
- [69] A. Nemiroski, M. Gonidec, J. M. Fox, P. Jean-Remy, E. Turnage, and G. M. Whitesides, "Engineering shadows to fabricate optical metasurfaces," *ACS Nano*, vol. 8, pp. 11061–11070, 2014.
- [70] C. M. Muller, F. C. F. Mornaghini, and R. Spolenak, "Ordered arrays of faceted gold nanoparticles obtained by dewetting and nanosphere lithography," *Nanotechnology*, vol. 19, p. 485306, 2008.
- [71] A. V. Whitney, B. D. Myers, and R. P. Van Duyne, "Sub-100 nm triangular nanopores fabricated with the reactive ion etching variant of nanosphere lithography and angle-resolved nanosphere lithography," *Nano Lett.*, vol. 4, pp. 1507–1511, 2004.
- [72] H. Fredriksson, Y. Alaverdyan, A. Dmitriev, C. Langhammer, D. S. Sutherland, M. Zach, and B. Kasemo, "Hole-mask colloidal lithography," *Adv. Mater.*, vol. 19, pp. 4297–4302, 2007.
- [73] S. V. Kostinski, E. R. Chen, and M. P. Brenner, "Characterization of patterns formed by shadows of spheres," *Phys. Rev. Lett.*, vol. 112, p. 235502, 2014.
- [74] A. Kosiorek, W. Kandulski, P. Chudzinski, K. Kempa, and M. Giersig, "Shadow nanosphere lithography: Simulation and experiment," *Nano Lett.*, vol. 4, pp. 1359–1363, 2004.
- [75] A. Kosiorek, W. Kandulski, H. Glaczynska, and M. Giersig, "Fabrication of nanoscale rings, dots, and rods by combining shadow nanosphere lithography and annealed polystyrene nanosphere masks," *Small*, vol. 1, pp. 439–444, 2005.
- [76] G. Mie, "Contributions on the optics of turbid media, particularly colloidal metal solutions," *Ann. Phys.*, vol. 25, p. 377, 1908.

- [77] K. A. Willets and R. P. Van Duyne, “Localized surface plasmon resonance spectroscopy and sensing,” *Annual Review of Physical Chemistry*, vol. 58, pp. 267–297, 2007. Willets, Katherine A. Van Duyne, Richard P.
- [78] U. Kreibig and M. Vollmer, *Optical Properties of Metal Clusters*. Germany: Springer Series in Material Science, 1995.
- [79] V. M. Shalaev, ed., *Optical Properties of Nanostructured Random Media*. Springer Berlin Heidelberg, 2002.
- [80] P. R. West, S. Ishii, G. V. Naik, N. K. Emani, V. M. Shalaev, and A. Boltasseva, “Searching for better plasmonic materials,” *Laser Photonics Rev.*, vol. 4, pp. 795–808, 2010.
- [81] E. Ozbay, “Plasmonics: Merging photonics and electronics at nanoscale dimensions,” *Science*, vol. 311, pp. 189–193, 2006.
- [82] S. Shukla and S. Seal, “Theoretical model for nanocrystallite size dependent gas sensitivity enhancement in nanocrystalline tin oxide sensor,” *Sens. Lett.*, vol. 2, no. 1, pp. 73–77, 2004.
- [83] A. M. Schrand, L. K. Braydich-Stolle, J. J. Schlager, L. Dai, and S. M. Hussain, “Can silver nanoparticles be useful as potential biological labels?,” *Nanotechnology*, vol. 19, no. 23, 2008.
- [84] M. Losurdo, I. Bergmair, M. M. Giangregorio, B. Dastmalchi, G. V. Bianco, C. Helgert, E. P. Severin, M. Falkner, T. Pertsch, E. B. Kley, U. Huebner, M. A. Verschuuren, M. Muehlberger, K. Hingerl, and G. Bruno, “Enhancing chemical and optical stability of silver nanostructures by low-temperature hydrogen atoms processing,” *J. Phy. Chem. C*, vol. 115, pp. 23004–23012, 2012.
- [85] C. Shankar, A. T. N. Dao, P. Singh, K. Higashimine, D. M. Mott, and S. Maenosono, “Chemical stabilization of gold coated by silver core-shell nanoparticles via electron transfer,” *Nanotechnology*, vol. 23, no. 24, pp. 1–10, 2012.
- [86] M. Erol, Y. Han, S. K. Stanley, C. M. Stafford, H. Du, and S. Sukhishvili, “Sers not to be taken for granted in the presence of oxygen,” *Journal of the American Chemical Society*, vol. 131, no. 22, pp. 7480–7481, 2009. PMID: 19445502.
- [87] X. Li, J. Li, X. Zhou, Y. Ma, Z. Zheng, X. Duan, and Y. Qu, “Silver nanoparticles protected by monolayer graphene as a stabilized substrate for surface enhanced raman spectroscopy,” *Carbon*, vol. 66, pp. 713–719, 2014.
- [88] S. Ogawa, S. Murakami, K. Shirai, K. Nakanishi, T. Ohta, and S. Yagi, “Nexafs study of air oxidation for mg nanoparticle thin film,” *J. Phys.: Conf. Ser.*, vol. 417, p. 012065, 2013.
- [89] J. Bischoff and A. T. Motta, “Eftem and eels analysis of the oxide layer formed on hcm12a exposed to scw,” *J. Nucl. Mater.*, vol. 430, pp. 171–180, 2012.

- [90] M. D. McMahon, R. Lopez, H. M. Meyer III, L. C. Feldman, and R. F. Haglund Jr., “Rapid tarnishing of silver nanoparticles in ambient laboratory air,” *Appl. Phys. B: Lasers Opt.*, vol. 80, pp. 915–921, 2005.
- [91] S. Peng, J. M. McMahon, G. C. Schatz, S. K. Gray, and Y. Sun, “Reversing the size-dependence of surface plasmon resonances,” *Proc. Natl. Acad. Sci. U.S.A.*, vol. 107, pp. 14530–14534, 2010.
- [92] Y. Han, R. Lupitskyy, T.-M. Chou, C. M. Stafford, H. Du, and S. Sukhishvili, “Effect of oxidation on surface-enhanced raman scattering activity of silver nanoparticles: A quantitative correlation,” *Analytical Chemistry*, vol. 83, pp. 5873–5880, Aug. 2011.
- [93] G. Jerkiewicz, G. Vatankhah, J. Lessard, M. P. Soriaga, and Y. S. Park, “Surface-oxide growth at platinum electrodes in aqueous h<sub>2</sub>so<sub>4</sub> reexamination of its mechanism through combined cyclic-voltammetry, electrochemical quartz-crystal nanobalance, and auger electron spectroscopy measurements,” *Electrochim. Acta*, vol. 49, pp. 1451–1459, 2004.
- [94] U. Kreibig and C. Vonfrags, “Limitation of electron mean free path in smaill silver particles,” *Zeitschrift fur Physik*, vol. 224, no. 4, p. 307, 1969.
- [95] C. Sonnichsen, T. Franzl, T. Wilk, G. von Plessen, J. Feldmann, O. Wilson, and P. Mulvaney, “Drastic reduction of plasmon damping in gold nanorods,” *Phys. Rev. Lett.*, vol. 88, p. 077402, 2002.
- [96] E. J. Heilweil and R. M. Hochstrasser, “Nonlinear spectroscopy and picosecond transient grating study of colloidal gold,” *J. Chem. Phys.*, vol. 82, pp. 4762–4770, 1985.
- [97] M. Blaber, M. Arnold, and M. Ford, “A review of the optical properties of alloys and intermetallics for plasmonics,” *J. Phys: Cond. Matt.*, vol. 22, pp. 143201(1–15), 2010.
- [98] G. V. Naik, V. M. Shalaev, and A. Boltasseva, “Alternative plasmonic materials: Beyond gold and silver,” *Adv. Mater.*, vol. 25, pp. 3264–3294, 2013.
- [99] S. Link and M. A. El-Sayed, “Shape and size dependence of radiative, non-radiative and photothermal properties of gold nanocrystals,” *Int. Rev. Phys. Chem.*, vol. 19, pp. 409–453, 2000.
- [100] H. A. Atwater, S. Maier, A. Polman, J. A. Dionne, and L. Sweatlock, “The new "p-n junction": Plasmonics enables photonic access to the nanoworld,” *MRS Bulletin*, vol. 30, pp. 385–389, 2005.
- [101] H. A. Atwater, “The promise of plasmonics,” *Scientific American*, vol. 296, pp. 56–62, 2007.
- [102] L. Novotny and B. Hecht, *Principles of Nano-Optics*. UK: Cambridge University Press, 2006.
- [103] M. Hu, C. Novo, A. Funston, H. Wang, H. Staleva, S. Zou, P. Mulvaney, Y. Xia, and G. V. Hartland, “Dark-field microscopy studies of single metal nanoparticles: understanding the factors that influence the linewidth of the localized surface plasmon resonance,” *J. Mater. Chem.*, vol. 18, no. 17, pp. 1949–1960, 2008.

- [104] H. Hovel, S. Fritz, A. Hilger, U. Kreibig, and M. Vollmer, “Width of cluster plasmon resonances-bulk dielectric functions and chemical interface damping,” *Phys. Rev. B*, vol. 48, pp. 18178–18188, 1993.
- [105] Y. Chu, E. Schonbrun, T. Yang, and K. B. Crozier, “Experimental observation of narrow surface plasmon resonances in gold nanoparticle arrays,” *Appl. Phys. Lett.*, vol. 93, p. 181108, 2008.
- [106] R. Adato, A. A. Yanik, C. H. Wu, G. Shvets, and H. Altug, “Radiative engineering of plasmon lifetimes in embedded nanoantenna arrays,” *Optics Exp.*, vol. 18, pp. 4526–4537, 2010.
- [107] A. J. Haes and R. P. Van Duyne, “A nanoscale optical biosensor: Sensitivity and selectivity of an approach based on the localized surface plasmon resonance spectroscopy of triangular silver nanoparticles,” *J. Am. Chem. Soc.*, vol. 124, pp. 10596–10604, 2002.
- [108] K. S. Lee and M. A. El-Sayed, “Gold and silver nanoparticles in sensing and imaging: Sensitivity of plasmon response to size, shape, and metal composition,” *J. Phys. Chem. B*, vol. 10, pp. 19220–19225, 2006.
- [109] J. B. Jackson and N. J. Halas, “Surface-enhanced raman scattering on tunable plasmonic nanoparticle substrates,” *PNAS*, vol. 101, pp. 17930–17935, 2004.
- [110] K. R. Catchpole and A. Polman, “Plasmonic solar cells,” *Optic Express*, vol. 16, pp. 21793–21800, 2008.
- [111] S. Tomita, T. Kato, S. Tsunashima, S. Iwata, M. Fujii, and S. Hayashi, “Magneto-optical kerr effects of yttrium-iron garnet thin films incorporating gold nanoparticles,” *Phys. Rev. Lett.*, vol. 96, p. 167402, 2006.
- [112] K. Yang, C. Clavero, J. R. Skuza, M. Varela, and R. A. Lukaszew, “Surface plasmon resonance and magneto-optical enhancement on au-co nanocomposite thin films,” *Journal of Applied Physics*, vol. 107, p. 103924, 2010.
- [113] M. E. Mezeme, S. Lasquelles, and B. C., “Electromagnetic properties of resonant magnetoplasmonic core-shell nanostructures,” *J. Appl. Phy*, vol. 109, pp. 014302 (1–11), 2011.
- [114] B. Sepulveda, A. Calle, L. M. Lechuga, and G. Armelles, “Highly sensitive detection of biomolecules with the magneto-optic surface-plasmon-resonance sensor,” *Opt. Lett.*, vol. 31, p. 1085, 2006.
- [115] V. Myroshnychenko, J. Rodriguez-Fernandez, I. Pastoriza-Santos, A. M. Funston, C. Novo, P. Mulvaney, L. M. Liz-Marzan, and F. J. G. de Abajo, “Modelling the optical response of gold nanoparticles,” *Chem. Soc. Rev.*, vol. 37, pp. 1792–1805, 2008.
- [116] H. Garcia, R. Kalyanaraman, and R. Sureshkumar, “Nonlinear optical properties of multi-metal nanocomposites in a glass matrix,” *J. Phys. B: Atomic, Molecular and Optical Physics*, vol. 42, p. 175401, 2009.

- [117] H. Garcia, R. Sachan, and R. Kalyanaraman, “Optical plasmon properties of co-ag nano-composites within the mean-field approximation,” *Plasmonics*, vol. 7, pp. 137–141, 2012.
- [118] H. Garcia, J. Trice, R. Kalyanaraman, and R. Sureshkumar, “Self-consistent determination of plasmonic resonances in ternary nanocomposites,” *Phys. Rev. B*, vol. 75, p. 045439, 2007.
- [119] C. A. Foss Jr., C. L. Hornyak, J. A. Stockert, and C. R. Martin, “Optical properties of composite membranes containing arrays of nanoscopic gold cylinders,” *J. Phys. Chem.*, vol. 96, pp. 1491–1499, 1992.
- [120] C. A. Foss Jr., M. J. Tierney, and C. R. Martin, “Template synthesis of infrared-transparent metal microcylinders: Comparison of optical properties with the predictions of effective medium theory,” *J. Phys. Chem.*, vol. 96, pp. 9001–9007, 1992.
- [121] C. A. Foss Jr., G. L. Hornyak, J. A. Stockert, and C. R. Martin, “Template-synthesized nanoscopic gold particles: Optical spectra and the effects of particle size and shape,” *J. Phys. Chem.*, vol. 98, pp. 2963–2971, 1994.
- [122] G. L. Hornyak, C. J. Patrissi, and C. R. Martin, “Fabrication, characterization, and optical properties of gold nanoparticle/porous alumina composites: The nonscattering maxwell-garnett limit,” *J. Phys. Chem. B*, vol. 101, pp. 1548–1555, 1997.
- [123] C. L. Hornyak and C. R. Martin, “Optical properties of a family of au-nanoparticle-containing alumina membranes in which the nanoparticle shape is varied from needle-like (prolate) to spheroid, to pancake-like (oblate),” *Thin Solid Films*, vol. 303, pp. 84–88, 1997.
- [124] L. Rayleigh, “On the influence of obstacles arranged in rectangular order upon the properties of the medium,” *Phil. Mag.*, vol. 34, pp. 481–502, 1892.
- [125] B. S. LukYanchuk, M. I. Tribelsky, Z. B. Wang, Y. Zhou, M. H. Hong, L. S. Shi, and T. C. Chong, “Extraordinary scattering diagram for nanoparticles near plasmon resonance frequencies,” *Appl. Phys. A*, vol. 89, p. 259, 2007.
- [126] N. Felidj, J. A. Aubard, and G. Levi, “Discrete dipole approximation for ultraviolet-visible extinction spectra simulation of silver and gold colloids,” *J. Chem. Phys.*, vol. 111, p. 1195, 1999.
- [127] K. Yee, “Numerical solution of initial boundary value problems involving maxwell’s equations in isotropic media,” *IEEE Trans. Antennas.Propagations*, vol. 14, pp. 302–307, 1966.
- [128] L. L. Foldy, “The multiyle scattering of waves .i. general theory of isotroyic scattering by randomly distributed scatterers,” *Phy. Rev.*, vol. 67, pp. 107–119, 1945.
- [129] L. Lewin, “The electrical constants of a material loaded with spherical particles,” *J. Inst. Elect. Eng. Pt. III: Radio Commun. Eng.*, vol. 94, pp. 65–68, 1947.



- [130] M. Lax, "Multiple scattering of waves. ii. the effective field in dense systems," *Phy. Rev.*, vol. 85, pp. 621–629, 1952.
- [131] W. T. Doyle, "Optical properties of a suspension of metal spheres," *Phy. Rev. B*, vol. 39, pp. 9852–9858, 1989.
- [132] C. E. Dungey and C. F. Bohren, "Light scattering by nonspherical particles: a refinement to the coupled-dipole method," *J. Opt. Soc. Am. A*, vol. 8, pp. 81–87, 1991.
- [133] A. Malasi, R. Kalyanaraman, and H. Garcia, "From mie to fresnel through effective medium approximation with multipole contributions," *J. Optics*, vol. 16, p. 065001, 2014.
- [134] P. P. Edwards, A. Porch, M. O. Jones, D. V. Morgan, and R. M. Perks, "Basic materials physics of transparent conducting oxides," *Dalton Transactions*, pp. 2995–3002, 2004.
- [135] T. Kamiya and H. Hosono, "Material characteristics and applications of transparent amorphous oxide semiconductors," *NPG Asia Mater.*, vol. 2, pp. 15–22, 2010.
- [136] K. Ellmer, "Past achievements and future challenges in the development of optically transparent electrodes," *Nat. Photonics*, vol. 6, pp. 808–816, 2012.
- [137] K. Nomura, H. Ohta, A. Takagi, T. Kamiya, M. Hirano, and H. Hosono, "Room-temperature fabrication of transparent flexible thin-film transistors using amorphous oxide semiconductors," *Nature*, vol. 432, pp. 488–492, 2004.
- [138] J. F. Wager, B. Yeh, R. L. Hoffman, and D. A. Keszler, "An amorphous oxide semiconductor thin-film transistor route to oxide electronics," *Current Opinion in Solid State & Materials Science*, vol. 18, pp. 53–61, 2014.
- [139] H. Hosono, N. Kikuchi, N. Ueda, and H. Kawazoe, "Working hypothesis to explore novel wide band gap electrically conducting amorphous oxides and examples," *J. Non-Crys. Solids*, vol. 198-200, pp. 165–169, 1996.
- [140] K. Nomura, T. Kamiya, H. Ohta, T. Uruga, M. Hirano, and H. Hosono, "Local coordination structure and electronic structure of the large electron mobility amorphous oxide semiconductor in-ga-zn-o: Experiment and ab initio calculations," *Phys. Rev. B*, vol. 75, no. 3, p. 035212, 2007.
- [141] R. Martins, P. Barquinha, L. Pereira, I. Ferreira, and E. Fortunato, "Role of order and disorder in covalent semiconductors and ionic oxides used to produce thin film transistors," *Appl. Phys. A*, vol. 89, pp. 37–42, 2007.
- [142] J. Robertson, R. Gillen, and S. J. Clark, "Advances in understanding of transparent conducting oxides," *Thin Solid Films*, vol. 520, pp. 3714–3720, 2012.

- [143] R. Khanal, D. B. Buchholz, R. P. H. Chang, and J. E. Medvedeva, "Composition-dependent structural and transport properties of amorphous transparent conducting oxides," *Phys. Rev. B*, vol. 91, p. 205203, 2015.
- [144] C.-N. Lok, C.-M. Ho, R. Chen, Q.-Y. He, W.-Y. Yu, H. Sun, P. K.-H. Tam, J.-F. Chiu, and C.-M. Che, "Silver nanoparticles: partial oxidation and antibacterial activities," *JOURNAL OF BIOLOGICAL INORGANIC CHEMISTRY*, vol. 12, pp. 527–534, MAY 2007.
- [145] T. Rindzevicius, Y. Alaverdyan, M. Kall, W. A. Murray, and W. L. Barnes, "Long-range refractive index sensing using plasmonic nanostructures," *JOURNAL OF PHYSICAL CHEMISTRY C*, vol. 111, pp. 11806–11810, AUG 16 2007.
- [146] Y. Yin, Z. Li, Z. Zhong, B. Gates, Y. Xia, and S. Venkateswaran, "Synthesis and characterization of stable aqueous dispersions of silver nanoparticles through the Tollens process," *JOURNAL OF MATERIALS CHEMISTRY*, vol. 12, no. 3, pp. 522–527, 2002.
- [147] R. M. Bozorth, *Ferromagnetism*. Wiley-VCH, 1993.
- [148] M. Singleton and P. Nash, "The ag-ni (silver-nickel) system," *Bulletin of Alloy Phase Diagrams*, vol. 8, pp. 119–121, 1987.
- [149] L. J. Swartzendruber, "The ag-fe (silver-iron) system," *Bulletin of Alloy Phase Diagrams*, vol. 5, pp. 560–564, 1984.
- [150] I. Karakaya and W. T. Thompson, "The ag-co (silver-cobalt) system," *Bulletin of Alloy Phase Diagrams*, vol. 1986, pp. 259–263, 7.
- [151] D. Linde, ed., *The CRC Handbook of Chemistry and Physics*. Boca Raton: CRC Press, 1992.
- [152] C. L. Cheung, R. J. Nikoli, C. E. Reinhardt, and T. F. Wang, "Fabrication of nanopillars by nanosphere lithography," *Nanotechnology*, vol. 17, pp. 1339–1343, 2006.
- [153] R. Sachan, A. Malasi, S. Yadavali, B. Griffey, J. Dunlap, G. Duscher, and R. Kalyanaraman, "Laser induced self-assembled nanostructures on electron transparent substrates," *Part. Part. Syst. Charact.*, vol. 32, pp. 476–482, 2015.
- [154] H. Krishna, N. Shirato, S. Yadavali, R. Sachan, J. Strader, and R. Kalyanaraman, "Self-organization of nanoscale multilayer liquid metal films: Experiment and theory," *ACS Nano*, vol. 5, no. 1, pp. 470–476, 2011.
- [155] A. Malasi, J. Ge, C. Carr, H. Garcia, G. Duscher, and R. Kalyanaraman, "Two-dimensionally ordered plasmonic and magnetic nanostructures on transferable electron transparent substrates," *Part. Part. Syst. Charact.*, vol. 32, pp. 970–978, 2015.
- [156] N. Shirato, *Morphology-properties studies in laser synthesized nanostructured materials*. PhD thesis, University of Tennessee Knoxville, 2012.

- [157] D. J. Bergman, “Rigorous bounds for the complex dielectric constant of a two-component composite,” *Annals of Physics*, vol. 138, pp. 78–114, 1982.
- [158] G. W. Milton, “Bounds on the complex permittivity of a two-component composite material,” *Journal of Applied Physics*, vol. 52, pp. 5286–5293, 1981.
- [159] H. Garcia, J. Trice, R. Kalyanaraman, and R. Sureshkumar, “Self-consistent determination of plasmonic resonances in ternary nanocomposites,” *Phys. Rev. B*, vol. 75, p. 045439, 2007.
- [160] R. Sachan, C. Gonzalez, O. Dyck, Y. Wu, H. Garcia, S. J. Pennycook, P. D. Rack, G. Duscher, and R. Kalyanaraman, “Enhanced absorption in ultrathin Si by Ni<sub>2</sub> nanoparticles,” *Nanomater. Energy*, vol. 2, pp. 11–19, 2012.
- [161] A. H. Sihvola, “How strict are theoretical bounds for dielectric properties of mixtures?,” *IEEE Trans Geosci Remote Sens*, vol. 40, pp. 880–886, 2002.
- [162] A. H. Sihvola, *Electromagnetic mixing formulas and applications*. The Institute of Electrical Engineers, 1999.
- [163] N. Shirato, H. Krishna, A. K. Gangopadhyay, and R. Kalyanaraman, “Magnetic measurement of pulsed laser-induced nanomagnetic arrays using surface magneto-optic Kerr effect,” in *Instrumentation, Metrology, and Standards for Nanomanufacturing IV*, 2010.
- [164] G. H. Chan, J. Zhao, E. M. Hicks, G. C. Schatz, and R. P. Van Duyne, “Plasmonic properties of copper nanoparticles fabricated by nanosphere lithography,” *Nano Lett.*, vol. 7, pp. 1947–1952, 2007.
- [165] V. V. Temnov, G. Armelles, U. Woggon, D. Guzatov, A. Cebollada, A. Garcia-Martin, J. M. Garcia-Martin, T. Thomay, A. Leitenstorfer, and R. Bratschitsch, “Active magneto-plasmonics in hybrid metal-ferromagnet structures,” *Nature Photon.*, vol. 4, pp. 107–111, 2010.
- [166] T. Shegai, S. Chen, V. D. Miljkovic, G. Zengin, P. Johansson, and M. Kall, “A bimetallic nanoantenna for directional colour routing,” *Nature Commun.*, vol. 2, p. 481, 2011.
- [167] N. Liu, M. L. Tang, M. Hentschel, H. Giessen, and A. P. Alivisatos, “Nanoantenna-enhanced gas sensing in a single tailored nanofocus,” *Nature Mater.*, vol. 10, pp. 631–636, 2011.
- [168] D. Rudolf, C. La-O-Vorakiat, M. Battiato, R. Adam, J. M. Shaw, E. Turgut, P. Maldonado, S. Mathias, P. Grychtol, H. T. Nembach, T. J. Silva, M. Aeschlimann, H. C. Kapteyn, M. M. Murnane, C. M. Schneider, and P. M. Oppeneer, “Ultrafast magnetization enhancement in metallic multilayers driven by superdiffusive spin current,” *Nature Commun.*, vol. 3, p. 1037, 2012.
- [169] V. I. Belotelov, L. E. Kreilkamp, I. A. Akimov, A. N. Kalish, D. A. Bykov, S. Kasture, V. J. Yallapragada, A. V. Gopal, S. I. Grishin, A. M. and Khartsev, M. Nur-E-Alam, M. Vasiliev, L. L. Doskolovich, D. R. Yakovlev, K. Alameh, A. K. Zvezdin, and M. Bayer, “Plasmon-mediated magneto-optical transparency,” *Nature Commun.*, vol. 4, p. 2128, 2013.

- [170] J. B. Gonzalez-Diaz, A. Garcia-Martin, J. M. Garcia-Martin, A. Cebollada, G. Armelles, B. Sepulveda, Y. Alaverdyan, and M. Kall, "Plasmonic Au/Co/Au Nanosandwiches with Enhanced Magneto-optical Activity," *Small*, vol. 4, pp. 202–205, 2008.
- [171] J. M. Hollas, *Modern Spectroscopy*. Wiley, 2004.
- [172] H. G. Tompkins and J. A. Augis, "The oxidation of cobalt in air from room temperature to 467 c," *Oxid. Met.*, vol. 16, p. 355, 1981.
- [173] K. V. Rao and A. Smakula, "Dielectric properties of cobalt oxide, nickel oxide, and their mixed crystals," *J. Appl. Phys.*, vol. 36, pp. 2031–2038, 1965.
- [174] P. R. Athey, F. K. Urban, M. F. Tabet, and W. A. McGahan, "Optical properties of cobalt oxide films deposited by spray pyrolysis," *J. Vac. Sci. Technol., A*, vol. 14, pp. 685–692, 1996.
- [175] D. Gallant, M. Pezolet, and S. Simard, "Optical and physical properties of cobalt oxide films electro-generated in bicarbonate aqueous media," *J. Phys. Chem. B*, vol. 110, pp. 6871–6880, 2006.
- [176] H. Krishna, J. Strader, A. K. Gangopadhyay, and R. Kalyanaraman, "Nanosecond laser-induced synthesis of nanoparticles with tailorable magnetic anisotropy," *J. Magn. Magn. Mater.*, vol. 323, pp. 356–362, 2011.
- [177] A. Malasi, H. Taz, A. Farah, M. Patel, B. Lawrie, R. Pooser, A. Baddorf, G. Duscher, and R. Kalyanaraman, "Novel iron-based ternary amorphous oxide semiconductor with very high transparency, electronic conductivity, and mobility," *Scientific Reports*, vol. 5, p. 18157, 2015.
- [178] H. Taz, R. Ruther, A. Malasi, S. Yadavali, C. Carr, J. Nanda, and R. Kalyanaraman, "In situ localized surface plasmon resonance (lspr) spectroscopy to investigate kinetics of chemical bath deposition of cds thin films," *J. Phys. Chem. C*, vol. 119, pp. 5033–5039, 2015.
- [179] M. Khenner, S. Yadavali, and R. Kalyanaraman, "Formation of organized nanostructures from unstable bilayers of thin metallic liquids," *Phys. Fluids*, vol. 23, p. 122105, 2011.
- [180] M. Khenner, S. Yadavali, and R. Kalyanaraman, "Controlling nanoparticles formation in molten metallic bilayers by pulsed-laser interference heating," *Math. Model. Nat. Phenom.*, 2012. In Press.
- [181] P. Offermans, S. R. K. Schaafsma, M. C. and Rodriguez, Y. Zhang, M. Crego-Calama, S. H. Brongersma, and J. G. Rivas, "Universal scaling of the figure of merit of plasmonic sensors," *ACS Nano*, vol. 5, pp. 5151–5157, 2011.
- [182] F. Wang and Y. R. Shen, "General properties of local plasmons in metal nanostructures," *Phys. Rev. Lett.*, vol. 97, p. 206806, 2006.
- [183] J. R. Lakowicz, "Radiative decay engineering: biophysical and biomedical applications," *Anal. Biochem.*, vol. 298, pp. 1–24, 2001.

- [184] Q. Hao, D. Du, C. Wang, W. Li, H. Huang, J. Li, T. Qiu, and P. K. Chu, “Plasmon-induced broadband fluorescence enhancement on al-ag bimetallic substrates,” *Sci. Rep.*, vol. 4, p. 6014, 2014.
- [185] J. C. Garnett, “Color in metal glasses and in metal films,” *Trans. Royal. Soc. London*, vol. CCIII, pp. 385–420, 1904.
- [186] W. L. Mochan and R. Barrera, eds., *ETOPIM3, Proceedings of the Third International Conference on Electrical Transport and Optical Properties of Inhomogeneous Media*, (North Holland, Amsterdam), 1994.
- [187] J. R. Kalnin and E. Kotomin, “Modified maxwell-garnett equation for the effective transport coefficients in inhomogeneous media,” *J. Phys. A: Math. Gen.*, vol. 31, p. 7227, 1998.
- [188] K. K. Karkkainen, A. H. Sihvola, and K. I. Nikoskinen, “Effective permittivity of mixtures: Numerical validation by the fdtd method,” *Trans. Geo. Sci. Rem. Sens*, vol. 38, p. 1303, 2000.
- [189] R. G. Barrera, G. Monsivais, and W. L. Mochan, “Renormalized polarizability in the maxwell garnett theory,” *Phy. Rev. B*, vol. 38, pp. 5371–5379, 1988.
- [190] R. Z. Bachrach and F. C. Brown, “Exciton-optical properties of tlbr and tlcl,” *Phys. Rev. B*, vol. 1, pp. 818–831, 1970.
- [191] E. A. Coronado and G. C. Schatz, “Surface plasmon broadening for arbitrary shape nanoparticles: A geometrical probability approach,” *J. Chem. Phys.*, vol. 119, pp. 3926–3934, 2003.
- [192] “www.sopra sa.com, sopra database.”
- [193] M. G. Blaber, M. D. Arnold, and M. J. Ford, “Search for the ideal plasmonic nanoshell: The effects of surface scattering and alternatives to gold and silver,” *J. Phys. Chem. C*, vol. 113, pp. 3041–3045, 2009.
- [194] R. Gans and H. Happel, “Zur optik kolloidaler metallosungen,” *Ann. Physik*, vol. 29, p. 277, 1909.
- [195] D. A. G. Bruggeman, “Calculation of various physics constants in heterogenous substances i dielectric constants and conductivity of mixed bodies from isotropic substances,” *Ann. Phys.*, vol. 24, pp. 636–664, 1935.
- [196] A. Lakhtakia, “Size-dependent maxwell-garnett formula from an integral equation formalism,” *Optik*, vol. 91, p. 134, 1992.
- [197] M. T. Prinkey, A. Lakhtakia, and B. Shanker, “On the extended maxwell-garnett and the extended bruggeman approaches for dielectric-in-dielectric composites,” *Optik*, vol. 96, pp. 25–30, 1994.
- [198] T. G. Mackay and A. Lakhtakia, “A limitation of the bruggeman formalism for homogenization,” *Opt. Comm.*, vol. 234, pp. 35–42, 2004.
- [199] A. Yariv, *Quantum Electronics*. John Wiley & Sons, 1989.

- [200] T. Yamashita and P. Hayes, "Analysis of XPS spectra of  $Fe^{2+}$  and  $Fe^{3+}$  ions in oxide materials," *Appl. Surf. Sci.*, vol. 254, pp. 2441–2449, 2008.
- [201] J. F. Moulder, W. F. Stickle, P. E. Sobol, and K. D. Bomben, *Handbook of X-Ray Photoelectron Spectroscopy*. Physical Electronics, Inc, Eden Prairie, MN, USA, 1995.
- [202] E. Quandt, B. Gerlach, and K. Seemann, "Preparation and applications of magnetostrictive thin-films," *J. Appl. Phys.*, vol. 76, pp. 7000–7002, 1994.
- [203] R. B. Vandover, E. M. Gyorgy, R. P. Frankenthal, M. Hong, and D. J. Siconolfi, "Effect of oxidation on the magnetic-properties of unprotected tbfe thin-films," *J. Appl. Phys.*, vol. 59, pp. 1291–1296, 1986.
- [204] B. Zhao, T. C. Kaspar, T. C. Droubay, J. McCloy, M. E. Bowden, V. Shutthanandan, S. M. Heald, and S. A. Chambers, "Electrical transport properties of Ti-doped  $Fe_2O_3(0001)$  epitaxial films," *Phys. Rev. B*, vol. 84, p. 245325, 2011.
- [205] H. B. Lal and K. Gaur, "Electrical-conduction in non-metallic rare-earth solids," *J. Mater. Sci.*, vol. 23, pp. 919–923, 1988.
- [206] R.-S. Chen, C.-C. Tang, W.-C. Shen, and Y.-S. Huang, "Thickness-dependent electrical conductivities and ohmic contacts in transition metal dichalcogenides multilayers," *Nanotechnology*, vol. 25, no. 41, p. 415706, 2014.
- [207] P. Cox, *Transition Metal Oxides: An Introduction to Their Electronic Structure and Properties*. The International series of monographs on chemistry, OUP Oxford, 2010.
- [208] F. J. Morin, "Electrical properties of ( $\alpha$ - $Fe_2O_3$ )," *Phys. Rev.*, vol. 93, pp. 1195–1199, 1954.
- [209] K. M. Rosso, D. M. A. Smith, and M. Dupuis, "An ab initio model of electron transport in hematite ( $\alpha$ - $Fe_2O_3$ ) basal planes," *J. Chem. Phys.*, vol. 118, pp. 6455–6466, 2003.
- [210] N. W. Gray, M. C. Prestgard, and A. Tiwari, "Tb<sub>2</sub>O<sub>3</sub> thin films: An alternative candidate for high-k dielectric applications," *Appl. Phys. Lett.*, vol. 105, pp. 1077–3118, 2014.
- [211] R. Gillen, S. J. Clark, and J. Robertson, "Nature of the electronic band gap in lanthanide oxides," *Phys. Rev. B*, vol. 87, p. 125116, 2013.
- [212] "Icsd database."
- [213] G. Ausanio, A. C. Barone, V. Iannotti, P. Scardi, M. Dincau, S. Amoruso, M. Vitiello, and L. Lantotte, "Morphology, structure and magnetic properties of (tb<sub>0.3</sub>dy<sub>0.7</sub>fe<sub>2</sub>)<sub>100</sub>-xfex nanogranular films produced by ultrashort pulsed laser deposition," *Nanotechnology*, vol. 17, pp. 536–542, 2006.

# Vita

Abhinav Malasi was born in Dehradun, India, on August 27th, 1984, the son of Mrs. Shashi Malasi and Mr. Netra Mani Malasi. He received dual degree for Bachelor of Technology and Master of Technology in Chemical Engineering from Indian Institute of Technology (IIT), Kanpur in the year 2008. After completing his Masters, he worked in IIT Kanpur for two years as a research associate. In the Fall of 2010, he joined the doctoral program in Department of Chemical and Biomolecular Engineering at University of Tennessee Knoxville. He pursued his PhD under the supervision of Dr. Ramki Kalyanaraman.